Optical properties of nanostructured dielectric materials: from photonic crystals to metamaterials

Kevin Vynck

UNIVERSITE MONTPELLIER II
SCIENCES ET TECHNIQUES DU LANGUEDOC

T H E S E

pour obtenir le grade de

DOCTEUR DE L'UNIVERSITE MONTPELLIER II

***Discipline** : Physique de la Matière Condensée*

***Ecole Doctorale :** Information, Structures, Systèmes*

présentée et soutenue publiquement

par

Kevin VYNCK

le 12 novembre 2008

Titre :

Propriétés optiques de matériaux diélectriques nanostructurés: Des cristaux photoniques aux métamatériaux

JURY

M. Walter KOB	Président du jury
M. Christian SEASSAL	Rapporteur
M. Gérard TAYEB	Rapporteur
M. Diederik S. WIERSMA	Rapporteur
M. Jean-Michel LOURTIOZ	Examinateur
M. David CASSAGNE	Directeur de thèse
M. Emmanuel CENTENO	Co-directeur de thèse
M. Eric AKMANSOY	Invité
M. Didier FELBACQ	Invité

Remerciements

Au terme de ces trois années de thèse passées à Montpellier, c'est avec une immense joie que j'écris ces quelques lignes de remerciements.

J'aimerais tout d'abord exprimer ma gratitude à Messieurs Christian Seassal, Gérard Tayeb et Diederik Wiersma pour avoir consacré un temps précieux à la lecture détaillée de mes travaux, et à Messieurs Walter Kob, Jean-Michel Lourtioz, Eric Akmansoy et Didier Felbacq pour m'avoir fait l'honneur de participer à mon jury de soutenance.

C'était un grand privilège pour moi d'intégrer l'équipe de nano-photonique du Groupe d'Etude des Semiconducteurs. L'environnement agréable et intellectuellement stimulant que j'y ai trouvé a très largement contribué au bon déroulement de ma thèse. Je tiens particulièrement à remercier mon directeur de thèse, David Cassagne, qui a su m'initier aux joies du métier de chercheur et m'éclairer de ses connaissances à de nombreuses occasions. Sa disponibilité à mon égard et ses conseils avisés m'ont été d'une aide très précieuse. J'aimerais remercier tout aussi cordialement mon co-directeur de thèse, Emmanuel Centeno, que j'ai eu la chance de côtoyer au quotidien. Débordant d'idées novatrices et de bonne humeur, il a été une source de motivation et d'inspiration sans pareille. Un grand merci à Didier Felbacq, intarissable puits de connaissances avec lequel j'ai eu l'immense plaisir de travailler. Son implication dans ma thèse m'a ouvert à une physique riche, complexe et très attrayante. J'aimerais également remercier les autres membres de l'équipe, à savoir Jean-Paul Albert, Marine Le Vassor d'Yerville, Brahim Guizal, Alexandru Căbuz et Cristian Ciracì pour toute l'attention qu'ils ont accordée à mes travaux et pour leur sympathie qui m'est chère. Je tiens aussi à exprimer ma reconnaissance à Bernard Gil pour m'avoir accueilli au sein du laboratoire, ainsi qu'au personnel permanent et aux nombreux doctorants que j'ai eu le plaisir de fréquenter durant ces quelques années.

L'aboutissement de cette thèse eût été impossible sans la présence et le soutien de nombre de mes amis. J'aimerais dire un grand merci à Alexandru Căbuz, Mathieu Nespoulous, Catherine Nicolas, Lauréline Roger et Guillaume Toquer, amis d'exception avec lesquels j'ai eu la chance de partager d'innombrables moments plus inoubliables les uns que les autres. Je tiens à remercier chaleureusement Christelle Marcou et Maud Alcayde, qui m'ont régulièrement permis d'oublier mes recherches, le temps d'une *milonga*, et pour qui j'éprouve la plus profonde amitié. Merci également à Vanessa Amann-Steuer, Guillaume Lelong, Agnès Duri, et Guillaume Lecamp pour les bonnes ondes qu'ils m'ont envoyées à maintes reprises d'ici ou d'ailleurs.

Mes pensées les plus émues vont naturellement à l'ensemble de ma famille qui m'a soutenu des quatre coins de France. J'aimerais plus particulièrement remercier ma mère, Esther Diemunsch, qui m'a nourri de la volonté de réaliser mes rêves et n'a jamais manqué de m'aider dans les moments les plus difficiles, mon père, Bernard Vynck, pour son enthousiasme et ses encouragements permanents, qui m'ont apporté confiance et assurance, et ma grand-mère, Anne Hellstern, pour sa présence et son soutien de tous les instants.

Foreword

Light has fascinated mankind throughout the ages, by virtue of being a source of Life and the means by which we actually see the world. Our current understanding of its nature may be attributed to James Clark Maxwell, who unified electricity and magnetism into a consistent theory, in which light is described as an electromagnetic radiation [1], and Albert Einstein, who explained the photoelectric effect by the fact that light should be quantized in particles called *photons* [2], a finding that yielded the concept of wave-particle duality and set up the basis of Quantum Theory. The 20th century has been characterized by a wealth of major scientific and technological advances, especially on the apprehension of matter and its interaction with light. The development of the first lasers in the 1960s [3] marked the beginning of a new era full of hopes and challenges on the control of photons. Concurrently, the study of semiconductors to control the propagation of electrons and the development of reliable techniques to miniaturize electronic circuits were in full swing. In the early 1980s, the world was experiencing a profound transformation under the lead of semiconductors and opto-electronic devices.

In 1987, Yablonovitch and John set forth the idea that in theory, 3D artificial dielectric structures could be designed to exhibit an electromagnetic, or photonic band gap, by analogy with the electronic band gap of semiconductors [4, 5]. While the absence of electromagnetic modes could suppress spontaneous emission of light, structural defects could enhance it and lead to light localization effects. The advent of these structures, dubbed *photonic crystals*, generated a real burst of excitement in the scientific community, for they could allow a control over both the emission and propagation of light on the wavelength scale, the design of "nanocircuits for light". The existence of a photonic band gap has been verified experimentally shortly later and the number of studies on photonic crystals grew dramatically in the following years. Since that time, photonic crystals have demonstrated a myriad of novel optical effects and applications, such as low-loss photonic crystal fibers [6], low-threshold lasers [7], structures with enhanced non-linearities [8] and even some slowing down light [9]. Their unique dispersion properties have been shown to yield extremely anomalous behaviors [10], taking the examples of ultra-refraction, supercollimation and negative refraction effects, and as many additional ways to mold the flow of light.

While theorists and experimentalists paved the route toward sophisticated all-optical microchips, another original idea pushed Photonics to a higher level. It is well-known that natural materials are deprived of any magnetic activity at optical frequencies [11]. In 1999, Pendry showed that periodic arrays of metallic resonators could imitate a homogeneous medium with a dispersive effective permeability [12], demonstrating here again that artificial structures could exhibit optical properties unattainable in nature. This achievement brought out of the dark a previous study of Veselago [13] on abstract materials with negative permittivity and negative permeability that would reverse the normal behavior of electromagnetic waves. The actual fabrication of such a "double-negative" material one year later [14] set out intense investigations of these new artificial structures, called *metamaterials*. Within a few years, metamaterials have been shown to manipulate electromagnetic fields in a quite remarkable and

unprecedented way. They have, for example, the ability to reproduce the image of any light distribution with a subwavelength resolution [15, 16] or alternatively to guide light in a way to by-pass any obstacle, acting as an invisibility cloak [17]. Such realizations would have been absolutely unthinkable only a few years ago and they are now at reach.

All in all, the past twenty years have been exceptionally rich on the study and fabrication of nanostructured materials to control light. Photonic crystals and metamaterials have been shown to exceed *by far* the classical limits of conventional optical structures. Many researchers predict that the 21st century will to be to photons what the 20th century has been to electrons. And indeed, it seems a right time for it. The 21st century started on a worldwide telecommunication revolution but electronics is now approaching its limits in terms of speed and compactness. Biology (by extension, BioPhotonics) is also an expanding field, more and more using of the interaction between biological species and light for various applications in Medecine and Life Sciences. Solar power is finally at the heart of current efforts on renewable energy. In these areas and many others, photonic crystals and metamaterials could play a significant role.

This thesis is in line with this constant flow of new solutions for Photonics, covering a wide panel of different concepts *from photonic crystals to metamaterials*. We will focus exclusively on dielectric nanostructures, which, by contrast to metallic ones, are lossless at optical frequencies, while taking the most of the progress made on the fabrication level in the past decades (e.g. silicon technology). Our work is also theoretical. The increasing power of computers and the uninterrupted development of reliable modelling tools make it possible to study a large number of complex problems.

The thesis is articulated around the four following chapters:

- **Chapter 1** presents a brief overview of the basic concepts and principles of photonic crystals and metamaterials, necessary to approach each of the following ones with sufficient knowledge on the subject. We will highlight the main scientific concepts and technological achievements in the field, from the origin of the optical properties of photonic crystals to the latest challenges of metamaterials and will present the various modelling tools that have been used in this thesis.

- **Chapter 2** deals with the confinement of light in 3D opal-based photonic crystals, which, by reference to natural opals, consist of periodic arrangements of dielectric spheres. Such structures are particularly interesting on a technological point of view because they can be made by simple self-assembly techniques and thus, be fabricated with a high quality on large scales and at low cost. Handling the confinement of light in opals by the insertion of proper defects could yield many opportunities in Photonics. However, for a number of reasons that will be developed in the body of the thesis, this has been proved to be difficult. In this chapter, we will present various possible designs of waveguides and cavities in monolayers of spheres, two- and three-dimensional opal-based heterostructures and purely three-dimensional inverse opals (the latter consisting of air spheres in dielectric), thereby allowing a full control of light emission and propagation in 3D space.

- **Chapter 3** is devoted to the study of dispersion-based waveguiding in extended, i.e. defectless, photonic crystals. This much more recent concept of using the dispersion properties of photonic crystals to manipulate light has stimulated a great interest in the photonics community and has led within a few years to the development of a multitude of new technologies. The question of manipulating *light beams* has however been rarely addressed, although it is of a crucial importance. In this chapter, we will propose some possible ways to enhance the functionality and reliability of extended photonic crystals. We will show that graded photonic crystals, i.e. structures with a gradient in their lattice parameter, have the great ability to bend light on the wavelength scale,

and will closely investigate the effects related to the spatial dispersion and gradient strength of the structure on the propagating beam. We will then propose a practical and efficient solution to one of the main issues in the integration of extended photonic crystals on all-optical platforms, namely their poor coupling to external waveguides.

- **Chapter 4** finally provides some theoretical insight onto the optical properties of all-dielectric rod-type structures. Most of the major achievements in the field of metamaterials have been realized in the microwave regime using metallic resonators. Recent studies now try to scale these structures to the optical frequencies but progress is being slowed down by the losses and saturation effects inherent to the metal in this frequency range. In this chapter, we will show that dielectric rods can replace metallic resonators in their role of electric and magnetic atoms. We will propose a theory on this new type of metamaterials, show that they can exhibit overlapping negative permittivity and negative permeability and further that they can be scaled to the optical frequencies in a very simple manner. We will also discuss the effect of structural disorder on light propagation, which will finally lead us to the first-time observation of 2D microscopic necklace states.

Contents

Remerciements **1**

Foreword **3**

1 Introduction to photonic crystals and metamaterials **9**
1.1 Basics of photonic crystals . . . 9
1.1.1 Light propagation in periodic dielectric structures . . . 10
1.1.2 Properties and fabrication . . . 11
1.2 Band gap effects in photonic crystals . . . 13
1.2.1 Cavities . . . 15
1.2.2 Waveguides . . . 15
1.2.3 1D/2D versus 3D photonic crystals . . . 16
1.3 Dispersion effects in photonic crystals . . . 16
1.3.1 Principles . . . 16
1.3.2 Anomalous refraction . . . 17
1.4 Metamaterials . . . 19
1.4.1 Principles and applications . . . 20
1.4.2 Toward the optical frequencies . . . 21
1.5 Modelling tools . . . 22
1.5.1 Planewave expansion method . . . 22
1.5.2 Finite-difference time-domain method . . . 24
1.5.3 Finite-element method . . . 25
1.5.4 Scattering matrix method . . . 27

2 Confining light in opal-based photonic crystals **31**
2.1 Fabrication and optical properties of opals . . . 31
2.1.1 Direct opals . . . 32
2.1.2 Inverse opals . . . 32
2.1.3 Defects in opals . . . 34
2.2 Patterned monolayers of spheres . . . 35
2.2.1 Opening of photonic band gaps . . . 36
2.2.2 Waveguides and cavities . . . 37
2.3 Two- and three-dimensional heterostructures based on inverse opals . . . 40
2.3.1 Principles and design . . . 40
2.3.2 Broadband single-mode waveguide . . . 42
2.4 Purely three-dimensional inverse opals . . . 44

2.4.1 Waveguides . . . 45
2.4.2 Cavities . . . 46

3 Enhanced dispersion-based waveguiding in photonic crystals 51
3.1 Beam propagation in graded photonic crystals . . . 51
3.1.1 Principles of graded photonic crystals . . . 52
3.1.2 Propagation of light beams . . . 53
3.1.3 The mirage effect: comparison with experiments . . . 56
3.2 Light coupling to supercollimating photonic crystals . . . 60
3.2.1 Mode matching . . . 60
3.2.2 Impedance matching . . . 65

4 An all-dielectric route to metamaterials 69
4.1 Electric and magnetic dipole activities of dielectric rods . . . 70
4.1.1 Scattering of light by circular dielectric rods . . . 70
4.1.2 Far-field matching to radiating dipoles . . . 72
4.1.3 Resonances of high refractive index rods . . . 75
4.2 All-dielectric rod-type metamaterials operating at optical properties . . . 76
4.2.1 Optical properties of square arrays of rods . . . 77
4.2.2 Scaling to the optical frequencies . . . 80
4.2.3 From periodicity to randomness . . . 84

Conclusion 89

Bibliography 91

Chapter 1

Introduction to photonic crystals and metamaterials

Manipulating light is one of the greatest and most exciting challenges of the 21st century. The emergence of photonic crystals (PhCs) and metamaterials (MMs) has largely contributed to this quest. Both of them have already led to remarkable achievements and still allow us to envision further scientific and technological advances. This introductory chapter is intended to review the basics, applications and challenges of PhCs and MMs. In Sec. 1.1, we will introduce the principles underlying the optical properties of PhCs and the main fabrication techniques developed to date. In Sec. 1.2, we will show how the photonic band gaps (PBGs) of PhCs can be used to control the emission and propagation of light on the wavelength scale and in Sec. 1.3, how their dispersion properties can provide additional ways to enhance this control. MMs will be introduced in Sec. 1.4. We will see which are the motivations and objectives of current researches on the subject. In Sec. 1.5, we will finally give a brief overview of the different modelling techniques that have been used in this thesis.

In each of these sections, we will pay particular attention to the works the most related to our purposes and will voluntarily omit certain aspects of PhCs and MMs. These expanding fields have however the advantage of being presented by a consequent number of reviews and textbooks, which the reader can refer to if necessary (on PhCs, see e.g. [18–22]; on MMs, see e.g. [23–27]).

1.1 Basics of photonic crystals

Once again, Nature has demonstrated its ingeniousness much before scientists realized it. Iridescences of different colors can be observed in natural opals [28], on the wings of certain butterflies [29], on the cuticles of certain beetles [30] and in a variety of many other animal species. These optical effects are due to their microstructuring, which create multiple Bragg scattering effects. When the wavelength of light becomes comparable to the periodicity of the structure, the waves scattered by the various diffraction planes interfere constructively and destructively in a way to produce a diffraction pattern specific to the structure, notably prohibiting light propagation along certain directions. PhCs are artificial structures with a periodic modulation of the refractive index on the scale of the wavelength. Their purpose is precisely to mold the flow of light in a similar yet well-controlled manner. The existence of a complete PBG in particular can provide a full control over light emission and propagation in all 3D space. Reaching this objective however requires, at the lowest level, to have some understanding of how light behaves in

such media and to develop fabrication techniques capable of building wavelength scale nanostructures with a high quality.

1.1.1 Light propagation in periodic dielectric structures

Broadly speaking, electromagnetic fields in the optical range have a wavelength of the order of the micrometer. On this scale, the atomic structure of matter averages out to give a homogeneous, continuous medium with an electric permittivity ε and a magnetic permeability μ. PhCs rely on a spatial variation of these parameters on the micrometer scale. Light propagation in continuous media is described by the macroscopic Maxwell's equations, which, in the absence of free charges and currents and considering harmonic fields, reduce to a vector wave equation for the magnetic field $\mathbf{H}$ of the form:

$$\hat{\Theta}\mathbf{H}(\mathbf{r}) = \frac{\omega^2}{c^2}\mathbf{H}(\mathbf{r}) \tag{1.1}$$

with $\hat{\Theta} = \nabla \times \frac{1}{\varepsilon(\mathbf{r})}\nabla\times$. It has been assumed here that the medium is isotropic, linear and nonmagnetic.[1] Equation (1.1) is the master equation of harmonic propagation of light in mixed dielectric media, written in the form of an eigenvalue problem for the magnetic field $\mathbf{H}(\mathbf{r})$. Noting that the operator $\hat{\Theta}$ acting on the field is self-adjoint, the eigenvalue problem turns out to be ordinary, involving that its eigenvalues are necessarily real and that the associated eigenvectors are orthogonal to each other. A similar equation can be derived for the electric field $\mathbf{E}(\mathbf{r})$ but the operator in this case in not self-adjoint and consequently leads to a generalized eigenvalue problem. One usually prefers to solve the problem for the magnetic field and retrieve the electric field at a subsequent stage from Maxwell's equations.

Two remarks may be given at this point. First, it can be shown from Eq. (1.1) that the optical properties of dielectric media, assuming that they are nondispersive and macroscopic, do not rely on a fundamental length scale. They can be scaled to different frequencies only by expanding or contracting all distances. For this reason, the frequencies ω can be normalized by the lattice parameter a of the structure and given in units of $\frac{\omega a}{2\pi c} = \frac{a}{\lambda}$, where c is the velocity of light in free space and λ the wavelength of light. This fact has also been proved to be quite useful, for it makes it possible for experiments to be realized in the microwave range. Second, it is interesting to note that Eq. (1.1) can be well assimilated to Shrödinger's equation of Quantum Mechanics [31], which describes the behavior of non-interacting electrons in a potential function. In this sense, the permittivity $\varepsilon(\mathbf{r})$ of the dielectric composite plays the role of the potential $V(\mathbf{r})$ of a crystal. The steps to follow to solve the eigenvalue problem in a periodic structure are consequently very similar.

The permittivity of a periodic photonic crystal with lattice vectors $\mathbf{R}$ obeys the relation $\varepsilon(\mathbf{r}+\mathbf{R}) = \varepsilon(\mathbf{r})$. The Floquet-Bloch theorem states that the solution of the eigenvalue problem has to have the form of a planewave times a vectorial function with the periodicity of the structure lattice as:

$$\mathbf{H}(\mathbf{r}) = \mathbf{h}_\mathbf{k}(\mathbf{r})e^{i\mathbf{k}\cdot\mathbf{r}} \tag{1.2}$$

where $\mathbf{h}_\mathbf{k}(\mathbf{r}+\mathbf{R}) = \mathbf{h}_\mathbf{k}(\mathbf{r})$ and $\mathbf{k}$ is the wavevector defined in reciprocal space. By inserting Eq. (1.2) into Eq. (1.1), a new ordinary eigenvalue equation is obtained for the field $\mathbf{h}_\mathbf{k}$. The problem is now reduced to a single unit cell, where the periodicity is taken into account via the extra parameter $\mathbf{k}$. Similarly as for electrons in a potential well, to each value of $\mathbf{k}$ is attributed an infinite set of eigenvalues defined at discrete frequencies $\omega_n(\mathbf{k})$, where n is the order of the mode. When $\mathbf{k}$ is continuously varied, the

[1] The relative permeability $\mu(\mathbf{r})$ can be taken equal to unity everywhere because the magnetic response of natural materials fades out in the optical frequencies [11].

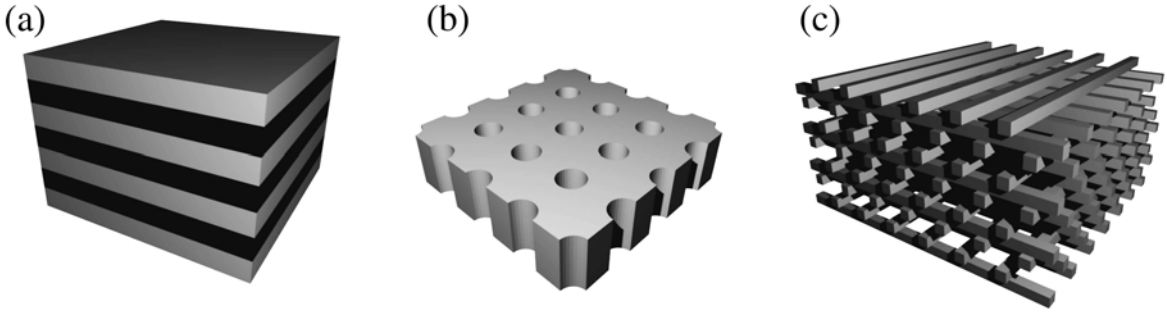

Figure 1.1: Sketch views of 1D (a), 2D (b) and 3D (c) PhCs.

continuous dispersion relation of $\omega_n(\mathbf{k})$ defines the photonic band structure of the PhC, which describes exactly the behavior of light in infinite, periodic structures. Due to the discrete translational symmetry of the lattice, the wavevectors $\mathbf{k}$ labeling the solutions can be restricted to the first Brillouin zone of the lattice. Moreover, $\omega_n(\mathbf{k})$ can be shown to possess the point group symmetry of the lattice, comprising inversion, rotation and reflection symmetries. It is therefore sufficient to describe the photonic band structure on the irreducible Brillouin zone. The actual computation of the photonic band structure can be made using the planewave expansion method, which we will briefly describe in Sec. 1.5.

1.1.2 Properties and fabrication

At the time when PhCs were introduced, the primary goal of the majority of researchers was to design and fabricate structures that would exhibit a preferably large and complete PBG to prohibit light propagation along all directions of space. These studies have quite naturally tried to scale PhCs to the near-infrared range ($\lambda = 1.55$ μm) to anticipate their use in telecommunications technologies. Of course, they have been confronted to many technological problems, eventually discovered new optical effects, which resulted in new designs and routes to follow. At the present time, a broad range of PhCs are available, as well as a variety of fabrication techniques. PhCs are generally organized in different categories, according to their dimensionality.

One-dimensional photonic crystals

One-dimensional (1D) PhCs have been known for a long time as Bragg mirrors. They consist of a periodic stack of dielectric layers of different refractive indices (Fig. 1.1(a)) and present the interesting capability to filter out (or in) certain wavelengths of a light signal. They have been used, for example, in distributed feedback lasers, anti-reflection coatings and high-reflectivity mirrors. Purely 1D PhCs extend to infinity in the two directions normal to the periodic direction and thus, do not exhibit a complete PBG. Light is therefore allowed to escape along the non-periodic directions. Still, they can make use of the refractive index contrast between the ambient medium and the dielectric stack to reflect incident light at all angles [32]. On a similar basis, micropillars have a finite size in the plane normal to the periodic direction and make use of the refractive index contrast between the stack and the ambient medium to reduce the amount of light escaping in the lateral directions.

Bragg mirrors can be fabricated by conventional thin-film depositions techniques, which have been proved to be extremely reliable throughout the years. An interesting alternative is the use of porous silicon, in which the local porosity defines an "average" refractive index that can be modulated with the depth of the penetration in the sample.

Two-dimensional photonic crystals

Strictly speaking, 2D PhCs are periodic in two dimensions of space and extend to infinity in the third one. They can consist either of a periodic set of high refractive index cylinders of arbitrary shape in a low refractive index medium (rod-type) or structures with an inverted dielectric contrast (hole-type, see Fig. 1.1(b)). Owing to the bi-dimensionality of the structure, electromagnetic modes can be treated separately according to their polarization. The E-polarization (s- or TM-polarization) and the H-polarization (p- or TE-polarization) correspond to the cases where the electric and magnetic fields are normal to the propagation plane, respectively.

In practice, 2D PhCs have to have a finite thickness. The modes may then be decoupled into their even or odd parity with respect to the mirror symmetry plane of the slab. From a technological point of view, integrating PhCs on all-optical chips encourage the use of thin layers. Here again, the refractive index contrast between the ambient medium and the PhC layer can be to our advantage. The ambient medium is described by the light cone, whose lower boundary (the light line) is given by $\omega = k\frac{c}{n_a}$, where k is the wavevector (or propagation constant) in the PhC, c the speed of light in free space and n_a the ambient refractive index. Light can therefore be confined to the PhC slab by index guiding while the PhC can offer lateral confinement if a PBG is found below the light line [33]. Early calculations and experiments have shown that 2D PBGs could be easily found in both rod-type and hole-type structures for both polarizations of light [34]. The first successful experimental demonstrations of the existence of PBGs in the near-infrared wavelengths [35, 36] have rapidly placed 2D structures at a preeminent position in PhCs research.

The fabrication of 2D PhCs has been inherited from micro and opto-electronic techniques. Typically, layers of semiconductors are grown in a stack and the pattering of the PhC is made by conventional lithography techniques, mainly photo- and electron-beam lithography. Most of the 2D PhCs studied up to now are hole-type structures, consisting of a high-refractive index slab, perforated by holes and deposited on a thick low refractive index substrate. At the present time, high quality structures can be made on a variety of different platforms, including multilayers, free-standing layers and silicon-on-insulator substrates.

Three-dimensional photonic crystals

If 2D PhCs seem to be a good compromise between ease of fabrication and radiation losses, three-dimensional (3D) PhCs remain the only structures really capable of exhibiting a complete PBG and thus, of truly controlling light in all 3D space. Unfortunately, they are also the most challenging ones to fabricate. Pushed by a constant flow of new designs, scientists have made use of their originality to develop entirely new fabrication techniques. It is fair to say that two classes of structures stood out of 3D PhCs: self-assembled and layered structures.

Self-assembled opals consist of dielectric spheres stacked in a compact face-centered cubic lattice. They have received a great deal of attention over the years because they can be reproduced artificially on large scales and at low cost. Opals with an inverted dielectric contrast, namely inverse opals, can exhibit a complete PBG provided that the index contrast is sufficiently large. This possibility has continuously motivated experimentalists to develop always more efficient self-assembly and inversion techniques [37–39]. Layered structures have been more rapidly disposed to meet the urging need of developing high-quality functional 3D PhCs. Woodpile structures, which consist of simple stacks of rods (see Fig. 1.1(c)), are probably the most popular ones in this family, for they exhibit large and complete PBGs and are relatively easy to fabricate [40, 41]. Other structures consisting of stacks of 2D PhC layers

have also been proposed [42]. They can be made using the so-called layer-by-layer technique, which consists of depositing and patterning successive dielectric layers to form the whole 3D structure. This approach is quite time and energy consuming compared to opal-based PhCs. As a matter of fact, layered structures have been perduring over the years owing to the simplicity with which suitable defects can be designed. This will be discussed in the next section.

From a broader point of view, the past twenty years have been relatively rich on the design and fabrication of 3D PhCs, taking into account other 3D structures (e.g. slanted-pore PhCs [43]) and techniques (e.g. robot-assisted micromanipulation [44]). There has been some interest recently on interference lithography [45] and direct laser writing techniques [46], which allow the patterning of large-scale 3D PhC templates of complex shapes. As a matter of fact, there seems to be a trend toward a more extensive use of 3D PhCs in Photonics. Nonetheless, it is important to bear in mind that 2D PhCs remain much easier to fabricate than 3D PhCs, while exhibiting most of the optical properties one could be interested in. The determining factor is therefore not so much about the ability of one structure or an other to exhibit PBGs, but rather to which extend we can use them to control light.

1.2 Band gap effects in photonic crystals

The advent of PhCs in the late 1980s naturally came with a great number of possible applications. The existence of PBGs offers the capability to confine light in wavelength scale areas and control its propagation in space, thereby opening the route toward all-optical technologies with enhanced functionalities [47].

To illustrate this point, we consider a 2D PhC consisting of a square array of air holes in dielectric. The choice of this structure is totally arbitrary and we do not loose any sense of generality by taking this example. Its photonic band structure is shown in Fig. 1.2. For the sake of clarity, only the three lowest frequency bands have been plotted. The dispersion curves (in blue) are represented along the high-symmetry directions of the irreducible Brillouin zone, which usually are sufficient to have a good picture of the optical properties of a PhC. The light line (dark gray) defines the limit frequency above which the PhC modes are leaky and the PBGs, highlighted in light gray areas, define the frequency ranges in which light propagation is prohibited.

Lattice imperfections in a PhC that exhibits such complete PBGs can give rise to fully localized electromagnetic modes. In fact, it is easy to conceive that light can be trapped in structural defects, surrounded by a structure in which it cannot propagate. To understand the physical origin of this phenomenon, it is very common to make the analogy with impurity modes in semiconductors [48]. The insertion of donors or acceptors in a semiconductor crystal supplies additional electrons or holes to the conduction or valence bands, respectively, which forms bound impurity levels in the electronic band gap. In the photonic case, creating a local increase (resp. decrease) of the refractive index in the PhC creates some impurity modes at lower (resp. higher) frequencies and eventually pulls them out within the PBG. The resulting modes are no longer extended in the PhC but become localized. The insertion of a point defect in a PhC (Fig. 1.3(a)) breaks the whole translational symmetry of the structure. Light cannot escape from the defect, which therefore becomes an optical cavity. When a linear defect is inserted in the PhC (Fig. 1.3(b)), a discrete translational symmetry is preserved along one direction. Light is then allowed to propagate along the defect only, which becomes an optical waveguide.

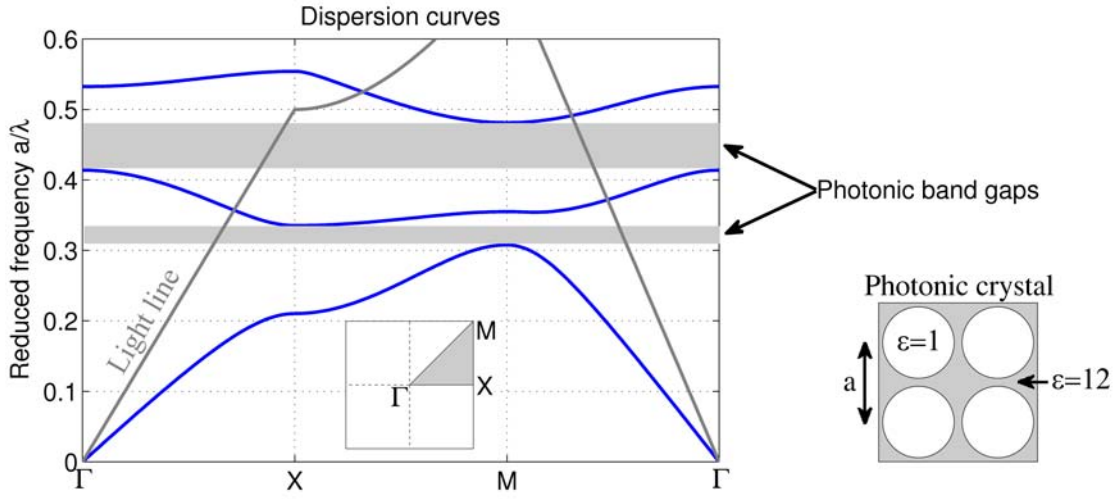

Figure 1.2: Photonic band structure of 2D PhC made of a square array of air holes of radius $0.45a$, where a is the lattice periodicity, in a dielectric medium of permittivity $\varepsilon = 12$. Representation along the high-symmetry directions of the first Brillouin zone (shown in the inset). The dispersion curves are in blue, the light line of air is in dark gray and the PBGs are enlighted in light gray shaded areas.

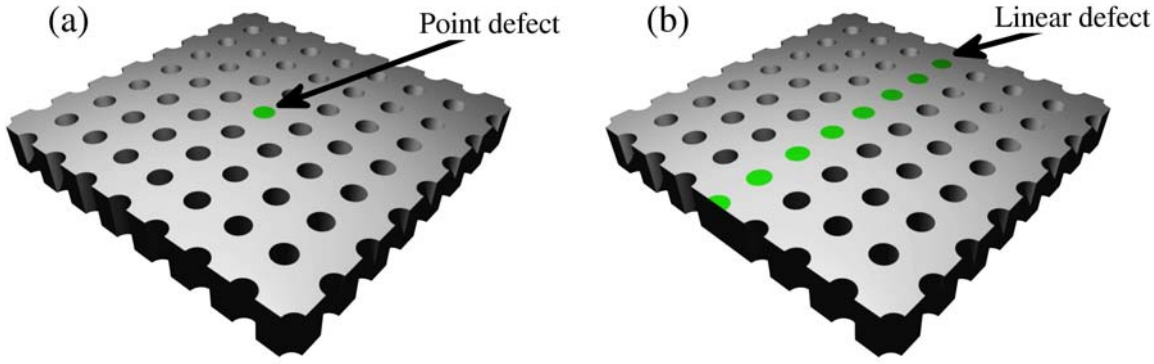

Figure 1.3: Sketch views of point (a) and linear (b) defects in a 2D PhC.

1.2.1 Cavities

The confinement of light in resonant optical cavities mainly centers on two purposes. The first one is the *enhancement of light-matter interactions*. Indeed, while spontaneous emission of light can be inhibited by creating an environment where no electromagnetic modes exist, it can also be greatly enhanced if matched in frequency with a resonant cavity. The rate of spontaneous emission is determined by the Purcell factor [49], which is proportional to the ratio Q/V, where Q is the quality factor of the cavity and V the modal volume. The quality factor of a cavity is then proportional to the lifetime of light in the cavity and is given by $Q = \omega_0/\Delta\omega$, where ω_0 is the resonant frequency of the cavity mode and $\Delta\omega$ its spectral width. Physically, the more photons spend time in the cavity, the more they interact with matter. Identically, a smaller modal volume enhances the local field intensity and increases interaction. Having large Q/V ratios find interest in lasing processes, nonlinear effects, environmental sensing and quantum information processing (e.g. quantum cryptography [50]), among others. PBGs in PhCs are expected to provide control over the losses of cavities (i.e. their quality factor) while keeping a hand on the spatial extension of the cavity mode. The compactness of PhC cavities is also suitable to their integration on all-optical platforms. Reaching high Q/V values to enhance light-matter interactions is therefore the first, and primary reason why scientists are interested in PhC cavities. The second one is the narrowness of the cavity spectral response. In this case, the cavity is not intended to interact with matter but to provide a very *high frequency-selectivity* to all-optical devices. Resonant cavities can be used for example in the telecommunications to filter out certain wavelengths of a light signal. The selectivity of the cavity corresponds to the spectral width $\Delta\omega$ of the mode, which implies that high-quality factor cavities are more selective. In sum, both purposes are demanding for high quality factors, and this has been, indeed, the main objective of studies on PhC cavities. Since the resonant modes of a cavity are inherent to the nature and the size of the defect, their quality factor is mainly a matter of design and thus, may be optimized accordingly.

1.2.2 Waveguides

Optical waveguides have played a major role in Photonics ever since the first opto-electronic devices appeared. The transport of light in conventional dielectric waveguides is ensured by total internal reflection, implying that losses appear at waveguide bends. The amount of lost light increases with the bending radius, which usually needs to be large to sustain a good transmission and consequently, seriously limits the possible degree of miniaturization of optical components. PhC waveguides rely on PBG effects so that if a bend is created, light cannot be radiated out of it precisely because no propagating mode exist in its surrounding. They are therefore expected to overcome conventional index-guided waveguides in terms of both efficiency and compactness. In view of using PhC waveguides in data transmission integrated systems, it is also desired that they be single-mode and broadband.[2] Both of these parameters rely on the nature of the defect and thus, may be tuned according to one's need. Alternatively, PhC waveguides can be considered for more evoluted purposes, for example by making them interact with neighboring cavities or waveguides [51] to create various PhC-based devices for the telecommunications, such as channel-drop filters, waveguide couplers and beam splitters.

[2] Single-mode operation is necessary to avoid losses due to inter-modal coupling, while broadband operation yields larger digital data rates.

1.2.3 1D/2D versus 3D photonic crystals

The great majority of studies on PhC cavities and waveguides have focused on 1D and 2D structures, which, in spite of being subject to radiation losses, are much more accessible experimentally than 3D ones. 1D micropillar cavities [52] and patterned strip waveguides such as air-bridge [53] and ladder-type PhC cavities [54] have demonstrated very high quality factors and small modal volumes, which, owing to the resulting strong coupling to light emitters, makes them particularly attractive for quantum information processing applications (e.g. on-demand single photon sources). 2D PhCs now benefit from an additional dimension to confine light. The literature is actually packed with an abundant number of design and fabrication studies on 2D PhC cavity/waveguide devices. 2D PhC cavities have demonstrated remarkably high quality factors [55, 56], strong coupling with single quantum dots [57, 58] and have been used to realize optically and electrically-pumped lasers [59–61]. 2D PhC waveguides have been shown to yield high transmission and bending efficiencies [62] and could be efficiently coupled to external waveguides [63, 64]. Over the years, 2D PhCs have demonstrated their ability to control light and have consequently been used primarily as testbeds for the study of newly discovered optical phenomena and as platforms for enhanced light-matter interactions and compact interconnection networks [65].

Confining light in 3D PhCs remains a live topic. In principle, 3D PhCs can provide an even greater control over light. In practice however, the challenge is twofold, being to fabricate high-quality 3D PhCs exhibiting stable and complete PBGs, and point or linear defects with suitable single-modes within the PBG frequency range. The difficulty in addressing both points depends on the complexity of the structure, which implies different amounts of computational efforts and more or less complicated fabrication processes. Theorists and experimentalists have naturally turned toward layered PhCs (e.g. woodpile), which are without doubt the most accessible ones from both points of view. Various experiments on cavity/waveguide structures indeed turned out to be quite successful [66–70]. Now, as we have seen in the previous section, there exists a reasonably broad panel of 3D structures, which, for most of them, can be fabricated with a high quality. Large attention has particularly been paid to opal structures because they present a great potential for low-cost integrated all-optical devices. Numerous experimental studies have also been carried out to embed controlled defects in inverse opals and at the present time, a variety of different techniques are available (see e.g. Ref. [71] and references therein). Progress is yet hardly made and theory seems to be the reason for this slow pace. Therefore, it seems worthwhile spending consequent efforts on the design of waveguides and cavities in opals. This will be our objective in Chapter 2.

1.3 Dispersion effects in photonic crystals

Although PBGs have drawn the attention of researchers for many years, they constitute only one particular case among the numerous complex optical effects that can occur in PhCs. As a matter of fact, light propagation in allowed frequency bands can exhibit very atypical behaviors, revealing new optical effects which can provide even mode control over electromagnetic fields [10, 72].

1.3.1 Principles

Fig. 1.4 shows the photonic band structure $\omega(\mathbf{k})$ of the 2D PhC considered above, displayed as dispersion surfaces over its entire first Brillouin zone. The iso-frequency curves (IFCs), or equi-frequency contours, of its first and second bands describe the PhC modes at given frequencies ($\omega(\mathbf{k})$ =const.). It is clear from this figure that PhCs can be strongly dispersive in both the frequency domain and the reciprocal space.

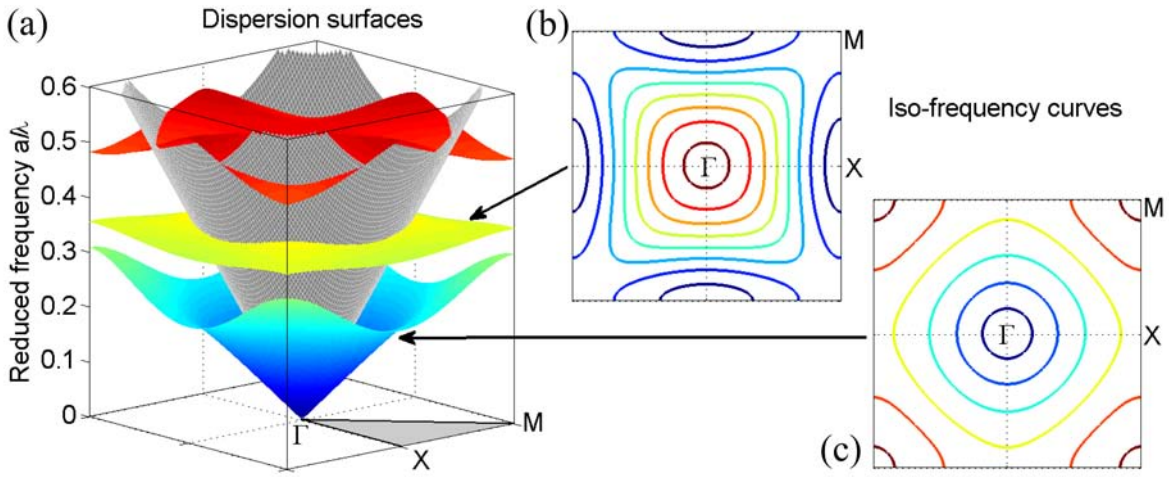

Figure 1.4: Photonic band structure of 2D PhC made of a square array of air holes of radius $0.45a$, where a is the lattice periodicity, in a dielectric medium of permittivity $\varepsilon = 12$. (a) Representation over the entire first Brillouin zone of the PhC reciprocal lattice. The dispersion surfaces are in color and the light cone in gray. Iso-frequency curves of the first (c) and second (b) bands, given in ascending order in reduced frequency a/λ following the rainbow colors from violet to red.

In a PhC, the average energy propagation velocity coincides with group velocity of light $\mathbf{v}_g$,[3] defined as:

$$\mathbf{v}_g = \nabla_{\mathbf{k}}\omega(\mathbf{k}) \tag{1.3}$$

This relation pulls out two interesting effects that can occur in PhCs: First, light can be slowed down to very low speeds. The norm of the group velocity being proportional to the slope of the dispersion surfaces, this effect occurs in regions where the dispersion curves flatten. Slow-light in PhCs has recently attracted a great deal of attention [9], providing the ability to process optical signals by using optical buffers and enhance light-matter interactions for linear and nonlinear effects (e.g. lasing [60]). Second, light can be refracted in very unusual ways. Here, the direction of the group velocity is given by the steepest ascent of the dispersion surfaces and is normal to the IFCs. As we will see now, the spatial dispersion of PhCs can be a very powerful handle on the flow of light.

Spatial dispersion evidences the fact that light does not behave in a same way along all directions of space. For example, the permittivity of a spatially dispersive dielectric medium is written as a function of the wavevector $\mathbf{k}$ as $\varepsilon(\omega, \mathbf{k})$, while the dependence in the frequency ω is the spectral dispersion. In PhCs, this dependence in $\mathbf{k}$ is included in the dispersion relation $\omega(\mathbf{k})$. Since light follows the group velocity direction, the phenomenon of spatial dispersion is particularly interesting when considering structures of finite-size, for those can exhibit anomalous refraction properties depending on the polarization of light and its angle of incidence. It is also worth noting that these effects do not require the insertion of any structural defect. This constitutes a new way to mold the flow of light, yielding many novel optical effects that we can use according to our needs.

1.3.2 Anomalous refraction

The refraction of light at the interface between two media is given by the conservation of the tangential component of the wavevector with respect to the coupling interface. This condition is due to the fact

[3] This supposes that the electromagnetic field be averaged over a unit cell and a period of time.

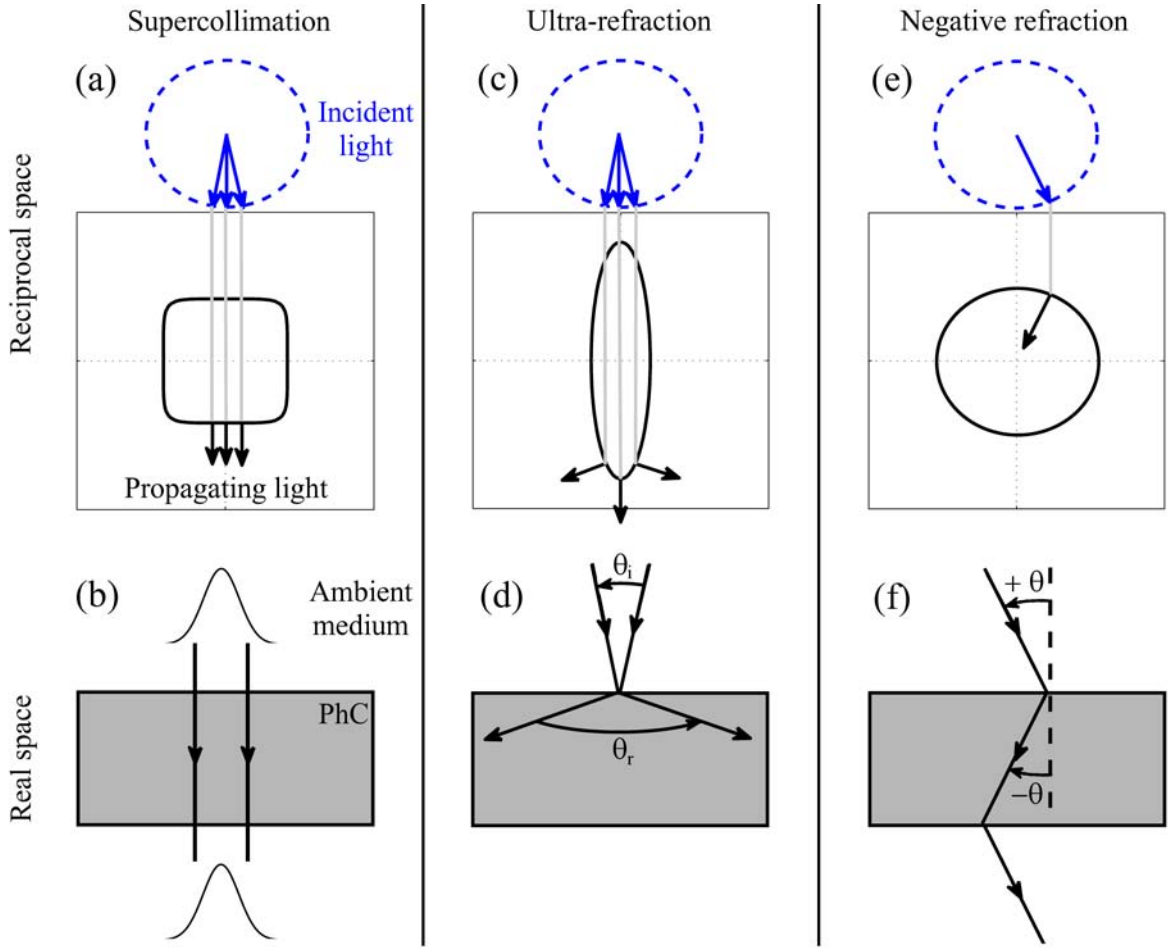

Figure 1.5: (a,b) Supercollimation (c,d) ultra-refraction and (e,f) negative refraction effects in extended PhCs. In reciprocal space (top), the wavevector components of the incident light are represented by blue arrows, defined by the IFC of the light cone (blue dashed curve). The light gray lines are the construction lines, which represent the conservation of the tangential component of the wavevectors at the coupling interface. The direction of the group velocity in the PhC is given by the black arrows normal to the IFC of the PhC (black solid curve). The flow of light in real space (bottom) is indicated by the black arrows.

that the spatial variation of the incident and refracted fields (their phase) have to be the same at the boundary. The refraction of monochromatic light in PhCs can be understood from the study of their IFCs.[4] Figure 1.5 sketches some of the typical effects of anomalous refraction in PhCs.

Supercollimation, also called self-collimation or self-guiding, occurs when the IFCs of the PhC exhibit a near-zero curvature on a certain reciprocal area [73–75]. This type of dispersion can be found, for example, at the inflection points of the IFCs on the first and second bands of 2D PhCs with square lattices (see e.g. Fig. 1.4). Straight IFCs imply that neighboring wavevector components of some incident light couple to PhC modes with parallel group velocities. Light beams, which are composed by a set of different wavevectors, therefore propagate in straight lines through the PhC without being dispersed. Propagation of near-infrared light on centimeter-scale distances has recently been demonstrated in a 2D PhC [76]. Another consequence of straight IFCs is that the different propagating modes are in phase with each other along the direction of propagation, thereby allowing us to control light in a similar way as in

[4]It is worthy of notice though, that photonic band structures calculated from the Floquet-Bloch theorem only make sense in infinite, periodic structures. They have been shown, however, to predict refraction effects with a very good accuracy in most cases.

PhC waveguides. By inserting structural defects in the PhC, it is possible to create optical routers [77], polarization beam splitters [78] and other devices [79]. Owing to this phase coherence, it is also very likely that supercollimated modes could be used for lasing.

Ultra-refraction, or superprism effect, takes place when the curvature of the IFCs is large. In this case, neighboring wavevector components couple to PhC modes with radically different directions of propagation, so that only slight variations of the angle of incidence can yield enormous variations of the angle of refraction. Typically, such large-curvature IFCs are found at the band edges of PBGs in PhCs of all dimensionalities [80–84]. Such IFCs also make the PhCs particularly sensitive to wavelength variations, finding use, for example, in wavelength division multiplexers [85]. The most important limitation of ultra-refractive structures is that light can be strongly dispersed in space. Taking the example illustrated in Fig. 1.5, the light beam that is collimated in the supercollimating PhC would spread over more than 120 degrees in the ultra-refractive PhC. Decreasing the incident beam width to make the structure more compact necessarily creates more dispersion, which is detrimental to the angular selectivity of the PhC.

Finally, *negative refraction* occurs when the group velocity of the incident beam is directed toward opposite directions with respect to the normal to the coupling interface [86,87]. It can be found on convex IFCs (e.g. in the vicinity of the M-point in Fig. 1.4(c)), or on dispersion surfaces where the direction of steepest ascent points inward, as illustrated in Fig. 1.5(e). This very counter-intuitive effect has set off a large interest in the scientific community, especially ever since Pendry proposed that negative refraction structures could be used to reconstruct a nearly perfect image of a point source [15]. The concept of negative refraction has been verified experimentally a few years ago [88–90], opening a route toward compact integrated subwavelength imaging systems.

From a general point of view, anomalous refraction in PhCs has triggered a burst of studies intended to discover new optical effects and complement the means offered by cavities and waveguides to control light. As a matter of fact, the propagation of light is not contrained by any structural defects in the PhC, in addition to which spatial dispersion allows us, in certain cases, to handle the spatial extension of light beams. Therefore it seems that extended PhCs could surpass many limitations of PhC waveguides. Each of these effects have been demonstrated experimentally and now would be the time to explore new possibilities for the manipulation of light beams in extended PhCs. In order for these structures to be truly operational, the coupling of light with external waveguides also needs to be improved. These points will be considered in Chapter 3.

1.4 Metamaterials

We have seen in the previous sections that light could be controlled on the wavelength scale by a periodic modulation of the permittivity $\varepsilon(\mathbf{r})$, resulting in complex Bragg reflections. A nice alternative to this approach could be to have direct control over the spectral dispersion of the permittivity $\varepsilon(\omega)$ and permeability $\mu(\omega)$. As briefly discussed in Sec. 1.1, these two parameters provide a homogeneous description of the collection of atoms and molecules of a material, much smaller than the wavelength of light. At optical frequencies, the permeability of natural materials tends to that of free space, which restricts their optical properties to a dielectric response. A way to overcome this limit is to reproduce this scheme on an intermediate scale by designing "artificial atoms", sufficiently small compared to the wavelength of light to be averaged out in a homogeneous medium and sufficiently large to be fabricable. It is particularly hoped in this way that by tuning the microscopic response of the atoms, one could create some artificial magnetism and thus, no longer be limited by a classical dielectric behavior but

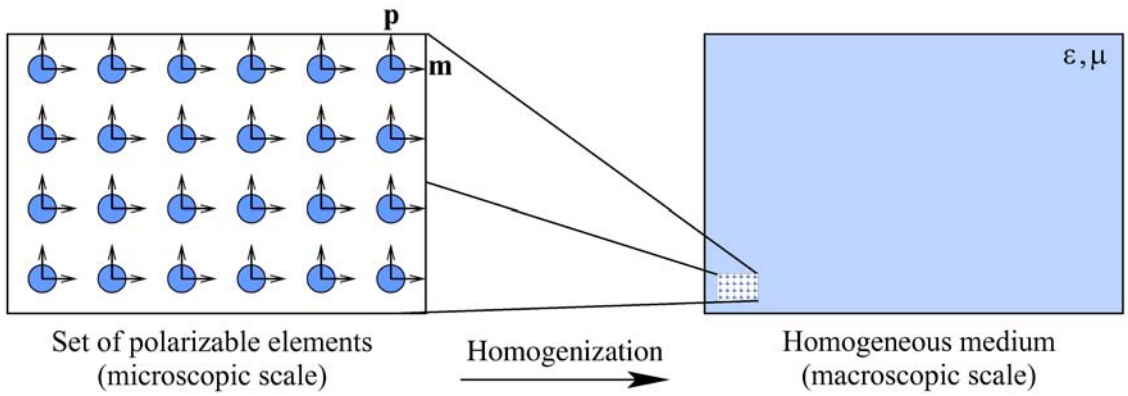

Figure 1.6: Homogenization of a set of polarizable elements with electric and magnetic dipole moments **p** and **m**, on the microscopic scale into a homogeneous medium with effective permittivity ε and permeability μ, on the macroscopic scale.

have a simultaneous control over the effective permittivity and permeability of matter. Metamaterials (MMs) are such artificial structures, composed of a set of microscopic resonators acting collectively to imitate a homogeneous medium with optical properties that exceed those found in nature.

1.4.1 Principles and applications

According to the definition of MMs above, two different scales are in play: (i) the microscopic scale, on which the artificial atoms resonate individually upon incident light and couple, in some way, to each other; and (ii) the macroscopic scale, on which the structure is considered as a whole and only characterized by an effective behavior. Since the optical properties of MMs are inherent to the *collective response* of their elements, their study necessarily starts on the microscopic scale and follows a bottom-up approach, as depicted in Fig. 1.6.

The very purpose of MMs being to exhibit anomalous optical properties, one has to look for strong spectral resonances of the permittivity ε and permeability μ. These two macroscopic quantities are respectively function of the electric and magnetic polarizabilities of the microscopic elements, which create electric and magnetic dipoles, **p** and **m** when immersed in an electromagnetic field. It is therefore desired that these elements exhibit strong microscopic resonances. Basically, reproducing an artificial dielectric behavior from any material is not so much of a problem. Already in the 1940s, Kock showed that a composite material made of metal spheres could mimic a homogeneous dielectric material [91]. Similarly, arrays of thin metallic wires are known to exhibit a cut-off frequency below which ε is negative [92]. It is however much more complicated to create artificial magnetism from nonmagnetic materials. In this regard, conducting elements have been thought as the most likely to exhibit strong magnetic dipole resonances since electromagnetic fields can generate large circulating currents that in turn, induce strong magnetic moments. This was the original idea of Pendry, who showed that arrays of so-called split-ring resonators could behave as a magnetic material [12]. These particular resonators have been intensively studied in the following years and inspired the design of a few other magnetic atoms.

Strongly dispersive $\varepsilon(\omega)$ and $\mu(\omega)$ can result in different optical effects. In 1968, Veselago studied theoretically a medium in which both ε and μ are simultaneously negative. He suggested that such a medium would be characterized by a negative index of refraction $n = -\sqrt{\varepsilon\mu}$ and support backward propagating waves [13]. In other words, the energy flow, represented by the Poynting vector **S**, would be opposite to the wavevector **k**. He called this type of medium a left-handed material, which we may

call double-negative material. Some interesting properties of such materials are reversed Doppler shifts and Čerenkov radiations as well as negative refraction of light. In 2000, Smith *et al.* fabricated the first double-negative MM in the microwave frequencies by interleaving arrays of thin metallic wires and split-ring resonators [14] and the negative refraction effect has been confirmed experimentally shortly later [93]. Concurrently, Pendry launched the concept of perfect lensing, the capability of double-negative materials to reproduce the image of a point source to the perfection [15]. Balanced between extended debates on this new concept and fervent hopes of subwavelength imaging, MMs attracted a great deal of attention in the scientific community and took an important role on the international scene.

The use of MMs is also not restricted to double-negative frequency ranges. The permittivity ε and permeability μ of MMs may be varied independently and take positive or negative values. It has been imagined then that by changing these properties in space, one could bring even more flexibility to the control over electromagnetic fields. Based on transformation optics principles, MMs can be made for light rays to follow totally arbitrary paths and, for instance, circumvent an object, thereby acting as an invisibility cloak [94]. This concept has been verified recently with the experimental demonstration of electromagnetic cloaking in the microwave frequencies [17]. Now, only looking at these impressive achievements, it seems that MMs have no bounds on the control over light. But this is not entirely true. As a matter of fact, the majority of experiments on MMs have been carried out in the microwave regime, for the sake of simplicity. Clearly, the use of MMs in the optical range would have a far-reaching impact on the technological level.

1.4.2 Toward the optical frequencies

Operating in the optical range obviously finds some interest in the telecommunications. MMs could be used to guide light in all-optical circuits or be the building block of various sophisticated optical components. But since PhCs have been proved to be extremely reliable on this level, there is naturally a trend toward more exotic effects. Subwavelength imaging in the optical frequencies could be put to good use in Medicine and Biology, while transformation optics-based devices could allow the realization of coatings capable to hide objects in visible light or, for example, light concentrators to generate high optical intensities and thus, increase the efficiency of solar energy conversion.

Scaling metamaterials to the optical frequencies is however a challenge of considerable magnitude. The first reason for this is that metals strongly deviate from being ideal conductors with increasing frequency, toward the optical range. They exhibit strong Ohmic losses, which significantly reduce the functionality of metallic resonators, taking the example of the saturation effects in split-ring resonators [95]. The second issue is that the resonators become increasingly difficult to fabricate as the operating wavelength is decreased, keeping in mind that ideally, the wavelength of light has to remain much larger than the size of the resonators and the average distance separating them. Scaling the magnetic resonances to the optical frequencies has become one of the major preoccupations of researchers in the past few years [96]. Numerous design and fabrication studies have been conducted, coming out with different designs of elements for optical magnetism (e.g. U-shaped resonators, paired metal strips) and negative indices of refraction (e.g. fishnet structures) [97]. A proof that much progress has been made is the recent demonstrations of negative refraction in the visible range [98,99]. But in spite of these promising results, the effective index of refraction of MMs are still given with an imaginary part, which unavoidably impairs their functionality.[5]

[5]The refractive index n is defined as $n = n' + in''$, where n' and n'' are its real and imaginary parts. The efficiency of a MM may be evaluated from the figure of merit $F = \frac{|n'|}{|n''|}$, which usually lies between 0 and 3 [96].

To address this problem of losses, it has been proposed that high-permittivity dielectric spheres or rods could replace the metallic resonators. As a matter of fact, it is well-known that dielectric objects can support different resonant modes, the so-called Mie resonances [100]. Various studies have shown that dielectric spheres and rods could produce electric and/or magnetic dipole resonances [101–103]. Interestingly, it has been suggested that arrays of dielectric rods in E-polarization could exhibit overlapping resonances of the permittivity and permeability, resulting in left-handed behavior [104, 105]. The first experiments realized in the microwave range have confirmed this hypothesis. Now, since this is a very new and unexplored topic, especially on the theoretical level, and because all-dielectric structures present a great potential for *lossless* optical magnetism and double-negative materials, gaining some insight onto the optical properties of all-dielectric rod-type structures will be the objective of Chapter 4.

1.5 Modelling tools

In the previous sections, we have briefly introduced the main principles of PhCs and MMs, and exposed a number of possible ways they offer to control electromagnetic fields. As for all branches of Science, experiments have often been supported by theoretical analyses, whether they be to predict or confirm the obtained results. The complexity of the problem often does not yield closed form solutions, and in this case, it requires the help of modelling techniques. The macroscopic Maxwell's equations describe exactly the behavior of electromagnetic fields in continuous media. In this sense, supposing that the structure and the materials involved are properly defined, the problem can, in principle, be solved quantitatively. Since, however, such an electromagnetic problem involves continuous quantities, a numerical treatement requires some discretization to reduce the problem to a finite number of degrees of freedom. This discretization is implemented in different ways according to the nature of the problem. It is also clear that a single method is not able to solve all kinds of problems related to electromagnetic structures and in practice, we are often inclined to use many of them.

1.5.1 Planewave expansion method

The introduction of the concept of PhCs and their PBGs came along with the need to calculate their dispersion properties. The planewave expansion (PWE) method has been developed within the first years of PhCs to answer this necessity. Its basic principles have been largely exploited for *ab-initio* calculations of electronic structures [48], explaining its early and rapid arrival in Photonics. The PWE method is a frequency-domain technique $(\mathbf{k}, \omega)$, intended to find the eigenfrequency and eigenfield of the natural modes of a structure. This requires to solve the eigenvalue problem of Eq. (1.1). The periodic part of the magnetic field in Eq. (1.2) can be written as a sum of planewaves as:

$$\mathbf{h}_{\mathbf{k}}(\mathbf{r}) = \sum_{\mathbf{G}} \mathbf{h}_{\mathbf{G}} e^{i\mathbf{G}\cdot\mathbf{r}} \tag{1.4}$$

where $\mathbf{G}$ is a vector of the reciprocal lattice. This relation is exact when the number of basis functions goes to infinity, yet to make the problem solvable numerically, the basis is truncated to N planewaves. Because of the transversality of the magnetic field ($\nabla \cdot \mathbf{H} = 0$), we can write $\mathbf{h}_{\mathbf{G}} = \sum_{\lambda=1}^{2} h_{\mathbf{G},\lambda} \hat{\mathbf{e}}_{\lambda}$, where $\hat{\mathbf{e}}_1$ and $\hat{\mathbf{e}}_2$ are unit vectors perpendicular to $\mathbf{k} + \mathbf{G}$. By using Eq. (1.4) with Eq. (1.2) and Eq. (1.1), the problem is formulated in terms of a matrix eigenvalue equation as:

$$\sum_{\mathbf{G}',\lambda'} \Theta^{\lambda,\lambda'}_{\mathbf{G},\mathbf{G}'} h_{\mathbf{G}',\lambda'} = \frac{\omega^2}{c^2} h_{\mathbf{G},\lambda} \tag{1.5}$$

where $\Theta^{\lambda,\lambda'}_{\mathbf{G},\mathbf{G}'}$ is a $2N \times 2N$ Hermitian matrix, given by:

$$\Theta^{\lambda,\lambda'}_{\mathbf{G},\mathbf{G}'} = |\mathbf{k}+\mathbf{G}||\mathbf{k}+\mathbf{G}'|\eta_{\mathbf{G},\mathbf{G}'} \begin{pmatrix} \hat{\mathbf{e}}_2 \cdot \hat{\mathbf{e}}_{2'} & -\hat{\mathbf{e}}_2 \cdot \hat{\mathbf{e}}_{1'} \\ -\hat{\mathbf{e}}_1 \cdot \hat{\mathbf{e}}_{2'} & \hat{\mathbf{e}}_1 \cdot \hat{\mathbf{e}}_{1'} \end{pmatrix}$$

$\eta_{\mathbf{G},\mathbf{G}'}$ is the inverse of the Fourier transform of the dielectric function $\varepsilon(\mathbf{r})$ and needs to be discretized in order to be solvable numerically. The calculation of $\eta_{\mathbf{G},\mathbf{G}'}$ can be made either by the direct (or "slow") method, which consists of inverting the dielectric function $\varepsilon(\mathbf{r})$, calculating its Fourier transform and finally truncating it, or by the Ho-Chan-Soukoulis method, where the dielectric function is first Fourier transformed, then truncated and finally inverted [106]. These two approaches are obviously not equivalent on a truncated basis but both give the rigorous solution to the Maxwell's equations on a complete basis. Once $\eta_{\mathbf{G},\mathbf{G}'}$ has been evaluated, $\Theta^{\lambda,\lambda'}_{\mathbf{G},\mathbf{G}'}$ can be computed explicitly and the eigenvalue problem in Eq. (1.5) can be solved by standard matrix diagonalization techniques. This way of solving the original eigenvalue problem has unfortunately demonstrated a poor planewave convergence, in addition to which the diagonalization and storage of the entire matrix are extremely expensive in time and memory.

To avoid an explicit storage of the matrix, it has been proposed to follow an iterative scheme [107]. In particular, when the number of planewaves matches that of spatial grid points, both representations take the form of a discrete Fourier transform. Since the curls $\nabla\times$ in reciprocal space are cross-products with $\mathbf{k}+\mathbf{G}$ and the multiplication by the inverse dielectric function is diagonal in direct space, applying $\hat{\Theta}$ to a vector can be computed by taking its curl in reciprocal space, computing the fast-Fourier transform, dividing by the dielectric function in direct space, computing the inverse fast-Fourier transform, and taking the curl again in reciprocal space. The first cycle of operation is made on a trial eigenvector and iterative eigensolvers then minimize the energy functional of the eigenmode, progressively converging to a solution. The convergence rate in this case is mainly limited by the discontinuities at the interfaces between different dielectric structures. This problem can be solved by smoothing the dielectric function with a kind of weighted average over the neighboring grid points. Although this yields a modified dielectric function, it allows rapidly converging and reliable results. This approach is implemented in the freely available software "MIT Photonic Bands" (MPB) [108], which we have used in this thesis.

Within a few years, the PWE method has become a standard for computing the dispersion properties of PhCs and the field pattern of their modes, which, as we have seen in the previous sections, are a basis for the understanding of most optical effects. Since it is based on the Floquet-Bloch theorem, the PWE method requires the structure to be strictly periodic. The calculation of defects modes is possible by using the supercell approach, which consists of reproducing the unit-cell of the structure on a number of periods sufficiently large to avoid interactions between neighboring defects. From these possibilities we may also draw out several limitations of this method. First, the time and memory required to calculate, for instance, defects modes in large 3D structures can be enormous. Supercells can involve a very large number of grid points and thus, a similar amount of planewaves. Second, this method cannot deal with radiation losses, as in slab-type structures for modes above the light cone, since it computes the resonant modes of the background, which are spurious. Third, owing to its periodicity requirement, it is not adapted to the study of finite-size or aperiodic structures and thus, is inadapted to any "real-world" system. More generally, it excludes all spatial and temporal specificities of the problems, which therefore require the use of different approaches.

1.5.2 Finite-difference time-domain method

The finite-difference time-domain (FDTD) method has been introduced by Yee in 1966 [109] originally to solve complex engineering problems of functional systems interacting with matter (e.g. lasers, quantum-optical systems). Since then, it has spread among many different areas [110], and is currently used intensively in the field of PhCs and MMs. The FDTD method is a space-grid time-domain technique $(\mathbf{r}, t)$, which discretizes the electromagnetic fields in both time and space and thus, does not involve any Fourier transform. The keystone of this method is precisely the way electromagnetic fields are related to each other in time and space. The Maxwell's curl equations relate the time variation of one field as a function of the spatial variation of the other. To illustrate this point, let us consider a linear, isotropic, non-dispersive and source-free medium.[6] Maxwell's curl equations read:

$$\frac{\partial \mathbf{H}}{\partial t} = -\frac{1}{\mu_0 \mu} \nabla \times \mathbf{E} \qquad \frac{\partial \mathbf{E}}{\partial t} = \frac{1}{\varepsilon_0 \varepsilon} \nabla \times \mathbf{H}$$

The electric and magnetic fields can be written in Cartesian coordinates of the system (x, y, z), which yields a set of six coupled scalar equations, from which the E_x-field component is:

$$\frac{\partial E_x}{\partial t} = \frac{1}{\varepsilon_0 \varepsilon} \left(\frac{\partial H_z}{\partial y} - \frac{\partial H_y}{\partial z} \right) \tag{1.6}$$

The original idea of Yee was to solve this set of equations, which includes both the electric and magnetic fields, instead of a vector wave equation such as Eq. (1.1), for only one of the two. The procedure to follow is pictured by the so-called Yee lattice, shown in Fig. 1.7, which consists of interleaved arrays of electric and magnetic components, disposed in such a way that every component of the electric field is surrounded by four components of the magnetic field and inversely. Every node of the spatial grid is defined by the coordinates $(i, j, k) = (i\Delta x, j\Delta y, k\Delta z)$, where Δx, Δy and Δz are the space increments along the x, y and z directions, respectively. Similarly, the time-stepping is defined by the index $n = n\Delta t$, where Δt is the time increment. Equation (1.6) can then be written in terms of central differences as:

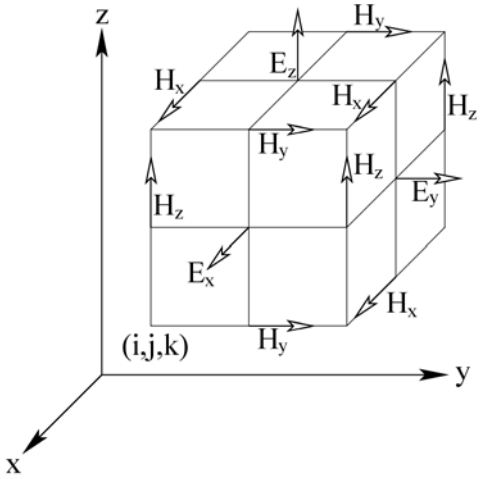

Figure 1.7: Yee lattice.

$$\frac{E_x\big|_{i,j+1/2,k+1/2}^{n+1/2} - E_x\big|_{i,j+1/2,k+1/2}^{n-1/2}}{\Delta t} =$$
$$\frac{1}{\varepsilon_0 \varepsilon_{i,j+1/2,k+1/2}} \left(\frac{H_z\big|_{i,j+1,k+1/2}^{n} - H_z\big|_{i,j,k+1/2}^{n}}{\Delta y} - \frac{H_y\big|_{i,j+1/2,k+1}^{n} - H_y\big|_{i,j+1/2,k}^{n}}{\Delta z} \right)$$

and similarly for the five other field components.

Yee's algorithm can be formulated in words as follows: given a certain distribution of electromagnetic fields, the electric field at a time $n+1/2$ is computed from the stored value of the electric field at $n-1/2$ and the curl of the local magnetic fields at n. The magnetic field at $n+1$ is then evaluated from the stored value of the magnetic field at n and the curl of the local electric field at $n+1/2$, and so on,

[6] The insertion of a source term absolutely causes no trouble. It has only been avoided for the sake of simplicity.

following a so-called "leapfrog" scheme.

The FDTD method presents many advantages that explain its success. It is flexible, in the sense that it can handle structures of arbitrary shapes, arrangement and made of any type of material (e.g. dispersive, nonlinear, metallic) as long as its parameters are properly defined. The excitation source can also be made as wanted (e.g. point source, Gaussian beam). Moreover, it provides a way to actually observe the propagation of light in *real space* and *real time*, which may have some interest, for instance, to study the propagation of light pulses in a PhC waveguide, the temporal decay of light in PhC cavities, or the coupling processes between neighboring resonators in MMs. The transmission and reflections spectra of a structure can be computed by integrating the energy flux passing through a defined area. Periodic boundary conditions can be imposed such that an harmonic inversion of the time signal can retrieve the natural modes of a periodic structure [111]. This presents a clear interest especially for the study of modes lying above the light line. In this sense, the FDTD method complements the PWE method on many points. In this thesis, we have used the freely available software "MIT Electromagnetic Equation Propagation" (MEEP) [112].

It is also important to point out the limitations of the FDTD method. First, the space-domain needs to be discretized on a finite computational area to be solvable numerically and special care has to be taken on its boundaries. It is common to use the so-called perfectly matched layers, which simulate an absorbing material to reduce (but not suppress) undesirable reflections [113]. Second, structures where the fields rapidly vary in space require a fine mesh to be accurately described. This implies that the calculation can be extremely memory consuming. Another consequence of this is due to the fact that the time increment Δt needs to be bounded to ensure the numerical stability of the computations. Δt is related to the space increments Δx, Δy and Δz by the so-called Courant stability bound, given by

$$c\Delta t \leq \frac{1}{\sqrt{\frac{1}{(\Delta x)^2} + \frac{1}{(\Delta y)^2} + \frac{1}{(\Delta z)^2}}}$$

Fine spatial meshes therefore impose small time increments, which increases the computational time required to reach a desired state. This is obviously even more problematic for the study of slow-light structures. In this case, space-grid frequency-domain techniques $(\mathbf{r}, t)$ are prefered.

1.5.3 Finite-element method

The finite-element (FE) method is a numerical technique developed many decades ago to solve complex mathematical problems, originally in structural analysis. The principle of this method is basically to find an approximate solution to a complex equation by fractioning it into a system of simpler equations. This is particularly well adapted to our case as describing the behavior of light in electromagnetic structures is made by solving the Maxwell's equations in a system with more or less complex boundary conditions [114]. To illustrate this method, let us consider a spatial domain Ω enclosing a harmonic current distribution $\mathbf{J}$ oscillating at a frequency ω in a continuous medium of relative permittivity ε and permeability μ. This system is voluntarily made more general to emphasize the importance of the excitation source on the problem. From the Maxwell's equations, we can write the *inhomogeneous* vector wave equation for the magnetic field:

$$\nabla \times \left(\frac{1}{\varepsilon}\nabla \times \mathbf{H}\right) - \frac{\omega^2}{c^2}\mu\mathbf{H} = \nabla \times \left(\frac{1}{\varepsilon}\mathbf{J}\right)$$

which can be written as a differential equation:

$$\mathscr{L}\phi = f \tag{1.7}$$

where $\mathscr{L} = \nabla\times\frac{1}{\varepsilon}\nabla\times - \frac{\omega^2}{c^2}\mu$ is the differential operator, $\phi = \mathbf{H}$ the unknown quantity and $f = \nabla\times\left(\frac{1}{\varepsilon}\mathbf{J}\right)$ the excitation function. Considering the boundary conditions in Ω, Eq. (1.7) takes the form of a boundary-value problem, which may not be solvable analytically.

To deal with this problem, we introduce a trial function $\tilde{\phi}$ (i.e. $\tilde{\mathbf{H}}$ in our case), which we expand as $\tilde{\phi} = \sum_{i=1}^{N} c_i v_i$, where v_i are the expansion functions and c_i are unknown coefficients. The problem is now a system of N equations, from which we seek to find the coefficients that make $\tilde{\phi}$ fit the best to ϕ. There exists two popular ways to solve the problem.

First, the *Rayleigh-Ritz* method, which relies on the well-known variational principle, formulating the problem in terms of a functional. In the case of a self-adjoint and positive-definite operator $\mathscr{L}$,[7] the functional F can be written in the form:

$$F(\tilde{\phi}) = \frac{1}{2}\int_{\Omega} \tilde{\phi}\mathscr{L}\tilde{\phi}d\Omega - \int_{\Omega} f\tilde{\phi}d\Omega$$

The functional is then written explicitely as a function of the boundary conditions in the domain Ω. The following step is then to find the coefficients c_i that minimize the functional (i.e. $\frac{\partial F}{\partial c_i} = 0$), from which the trial function $\tilde{\phi}$ is the closest to the solution.

The second way to find these coefficients is to use the *Galerkin* method, which is defined as a weighted residual method. The weighted residual integrals R_i are defined as :

$$R_i = \int_{\Omega} \omega_i(\mathscr{L}\tilde{\phi} - f)d\Omega \qquad i = 1, 2, 3, \cdots, N$$

The term $\mathscr{L}\tilde{\phi} - f$ is nonzero if $\tilde{\phi}$ does not equal ϕ. The procedure of this method is then to find the correct weighting functions ω_i that set the integrals R_i to zero and thus, optimize $\tilde{\phi}$.

At this point, it is important to remark that the determination of the trial function $\tilde{\phi}$ is the fundamental step that determines the quality of the approximation, in the sense that a totally wrong guess yields a poor approximation. In complex systems, such as PhCs and MMs, it is obviously difficult to have a good guess for the trial function. To simplify the problem, the domain Ω is divided into small subdomains, called "elements". Supposing that these subdomains are small compared to the variation of ϕ implies that the trial functions *over each element* can be relatively simple. This is the basic principle of the FE method. The procedure to solve a complete problem is therefore the following: (i) the domain Ω is discretized into smaller subdomains (generally tetrahedra in 3D problems), whose size depend on the expected local variation of ϕ; (ii) the interpolation functions over each subdomains are defined (first or second order polynomials are generally good enough); (iii) the system of equations is formulated by the Rayleigh-Ritz or the Galerkin method and (iv) it is finally solved.

According to this brief description, it is not surprising that the FE method has met such a perdurable success over the years and in such a large number of different disciplines. One of the strengths of the FE method is without doubt its adaptative meshes, which concentrate on the regions of interest, thereby avoiding useless computational efforts, and match quasi-perfectly the different interfaces in the structure. The latter notably prevents numerical discrepencies to occur. Moreover, the materials involved in the computational domain can be arbitrary, as long as they are properly defined. By comparison with the

[7] These properties mainly depend on the boundary conditions of the system.

FDTD method, harmonic propagation does not require time to reach a steady-state, which is a clear advantage in many cases. The calculation of transmission and reflection efficiency of a structure is one of the many possible post-processing operations. Modal analysis can also be conducted by imposing periodic boundary conditions on the border of the computational area and by setting the excitation function f in Eq. (1.7) to zero. Finally, since the FE method is also applicable to many different fields of Physics, it allows the study of electro-, thermo- or piezo-optical effects, which is quite unique in computational electromagnetics.

All these advantages naturally come with a price to pay. Depending on the number of elements and the complexity of the boundaries, FE computations can be extremely expensive in memory. This is particularly true in 3D structures, where several millions of degrees of freedom can rapidly be involved. Although iterative solvers can generally handle large 3D electromagnetic problems, the FE method may then not be advantageous compared to other techniques in terms of computational time. Another weakness of the FE method is its complexity of implementation, which makes it quite inaccessible to newcomers. Hopefully recent years have seen the development of many reliable softwares with user-friendly interfaces, which greatly simplifies the setting of the problem. The commercial software "COMSOL Multiphysics", which we have used in this thesis, is one of them [115].

1.5.4 Scattering matrix method

The scattering of light by obstacles has been a long-standing topic, taking the example of Rayleigh scattering which explains the blue color of the sky by the scattering of sunlight by the molecules in the atmosphere [116]. The scattering matrix (SM) method has received increasing attention in years following the advent of PhCs, for it is a very reliable and intuitive approach to describe the scattering of light by large finite sets of objects. Broadly speaking, scattering matrices relate the initial and final states of interacting particles. In our context, the objective of the SM method is to make the connection between an arbitrary incident field on an assembly of objects and the field scattered by it. This method has been developed for 2D arrangements of cylinders [117] and 3D arrangements of spheres [118]. For the sake of simplicity, we will focus on the 2D case, keeping in mind that the underlying principles in the 3D case are similar, though not the formalism. Light is also assumed to be E-polarized, noting that similar steps could be carried out the H-polarization, and a time dependence in $e^{-i\omega t}$ is implicitely used.

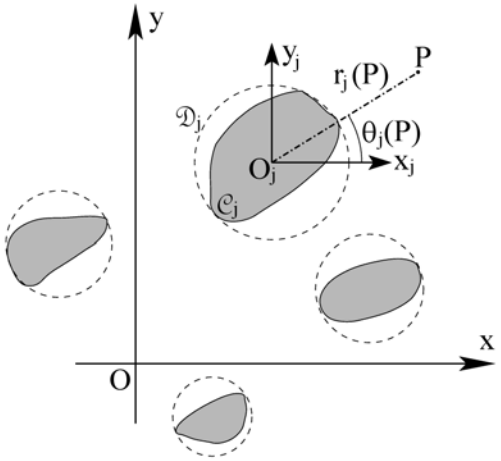

Figure 1.8: Collection of cylinders $\mathscr{C}_j$ of arbitrary shape, index and position.

We consider a 2D arrangement of N parallel cylinders denoted $\mathscr{C}_j$ $(j = 1, 2, \cdots N)$ of arbitrary shape, index and position, included in circles $\mathscr{D}_j$ of center O_j, embedded in air (see Fig. 1.8). Supposing that some light is incident on such a collection of cylinders, the total field (outside the cylinders) can then be decomposed into three different contributions with respect to the cylinder $\mathscr{C}_j$: (i) the actual incident field, (ii) the field scattered by all cylinders but $\mathscr{C}_j$, and (iii) the field scattered by $\mathscr{C}_j$. The local incident field on the cylinder $\mathscr{C}_j$ is therefore composed of (i) and (ii). After some mathematical development (see the details in Ref. [117]), the total field can be expanded in a Fourier-Bessel series and written in

the local coordinate system $(O_j,\, x_j,\, y_j)$ at any point P between $\mathscr{D}_j$ and the circle of center O_j passing through the closest point of the surrounding cylinders as:

$$E(P) = \sum_{m=-\infty}^{+\infty} a_{j,m} J_m[kr_j(P)] e^{im\theta_j(P)} + \sum_{m=-\infty}^{+\infty} b_{j,m} H_m^{(1)}[kr_j(P)] e^{im\theta_j(P)}$$

where $a_{j,m}$ and $b_{j,m}$ respectively represent the total incident (i+ii) and scattered (iii) fields with respect to $\mathscr{C}_j$, $r_j(P)$ and $\theta_j(P)$ are the polar coordinates of point P in the local coordinate system, and J_m and $H_m^{(1)}$ the mth-order Bessel and Hankel functions of the first kind.

The field scattered by all cylinders but $\mathscr{C}_j$ should then be the sum of the scattered field of individual cylinders, translated to their respective local coordinate system. This is transcribed mathematically using Graf's addition formula for Bessel functions [119], which yields the matrix equation:

$$\hat{\mathbf{a}}_j = \mathbf{Q}_j + \sum_{k \neq j} \mathbf{T}_{j,k} \hat{\mathbf{b}}_k$$

where $\hat{\mathbf{a}}_j$ and $\hat{\mathbf{b}}_k$ are the infinite column matrices of $a_{j,m}$ and $b_{k,m}$, respectively, $\mathbf{Q}_j$ is the column matrix corresponding to the actual incident field and $\mathbf{T}_{j,k}$ a square matrix relating the cylinders $\mathscr{C}_j$ and $\mathscr{C}_k$. In addition, it is well-known that the coefficients of the scattered field and locally incident field on a single cylinder are linked by the scattering matrix $\mathbf{S}_j$, which depend on the parameters of $\mathscr{C}_j$ only. This relation reads $\hat{\mathbf{b}}_j = \mathbf{S}_j \hat{\mathbf{a}}_j$, which yields the final equation:

$$\hat{\mathbf{b}}_j - \sum_{k \neq j} \mathbf{S}_j \mathbf{T}_{j,k} \hat{\mathbf{b}}_k = \mathbf{S}_j \mathbf{Q}_j$$

This matrix equation is a linear system of equations relating the fields diffracted by all cylinders (on the left-hand side) to the actual incident field (on the right-hand side). The matrices are made finite by truncating the Fourier-Bessel expansions involved. The resolution of this equation starts with the determination of the scattering matrix $\mathbf{S}_j$ of each cylinders. A closed form expression of the scattering matrix can be found for circular cylinders from Mie scattering theory [100], and supposing that all cylinders are alike implies that their scattering matrix are the same, which further simplifies the problem. In all cases, the matrix equation is solved to find the $\hat{\mathbf{b}}_j$ column matrix, which allows us to compute the total field outside the cylinders and gives access to other quantities such as its Poynting vector.

The SM method has been proved to be a very reliable and rapid technique to study the scattering of light by a large collection of objects. The required computational effort is actually a function of the number of objects and the truncation of the expansion but not of the spatial extension of the structure. There is no predefined computational area, the fields can be computed *at all points of space*, which also avoids any trouble related to undesirable reflections from free-space boundaries. In this regard, the SM method is particularly well adapted to harmonic propagation problems and can deal with arbitrary light sources, including planewaves, light beams or point sources. In the context of PhCs, it finds great use in the study of anomalous refraction effects, light localization by structural defects or disordered structures [120]. The computation of the far field is also possible.

The main weakness of the SM method is without doubt that assemblies of arbitrarily shaped objects cannot be easily treated, for they require the use of an external numerical technique such as the FDTD or FE methods. In addition, the problem is also not solvable in the case where neighboring circles $\mathscr{D}_j$ intersect each other, which impairs its range of applicability. In the case where the cylinders are circular, the latter condition is reduced to non-intersecting cylinders, which in the field of 2D PhCs is often met.

The code that we have used in this thesis has been developed by Centeno and Felbacq [121] and applied specifically to circular cylinders.

Summary

In this chapter, we have presented an overview of the main principles and applications of PhCs and MMs in the broad and expanding field of Photonics. We have seen different possible ways to manipulate electromagnetic fields and have identified some challenges to be addressed, more precisely on the confinement of light to structural defects in opal-based PhCs, on the use of spatial dispersion to control the propagation of light beams, and on the scaling of MMs to the optical range. These will be the objectives in this work. The modelling tools that we have just presented will help us solve this large panel of different problems.

Chapter 2

Confining light in opal-based photonic crystals

Confining light to structural defects has been the primary goal of photonic crystals (PhCs), on account of the potential they represent for all-optical telecommunication technologies, sensing devices and so on. In this context, opals have met quite a great success, for they can be reproduced artificially on large scales, at low cost and with a high-quality, thereby overcoming some of the technical limitations experienced by other 3D PhCs. Numerous studies have been carried out to apprehend their ability to control light at optical wavelengths, yet it has been rapidly found that structural defects with modes suitable to subsequent use are not trivial to design. This apparent difficulty has not discouraged experimentalists to develop sophisticated techniques to embed defects in them and at the present time, they strongly incite theorists to guide them toward reliable and realizable solutions.

This chapter is intended to provide different ways to confine light in opal-based PhCs. In Sec. 2.1, we will present the optical properties of 3D direct and inverse opals and review some of the current technologies used to fabricate and embed defects in them. In Sec. 2.2, we will show that patterned monolayers of spheres can exhibit PBGs below the light cone, making them reliable platforms for the design of single-mode waveguides and resonant cavities. In Sec. 2.3, we will study the confinement of light in two- and three-dimensional (2D-3D) heterostructures based on inverse opals and will present the design of a broadband single-mode waveguide. Finally, in Sec. 2.4, we will provide some novel insight onto the processes of light confinement in 3D inverse opals. This will make it possible to come out with simple designs of single-mode cavities and broadband single-mode waveguides, fabricable with current means and operating in the near-infrared range. This work has been part of a collaboration between different partners under the european PHAT project [122].

2.1 Fabrication and optical properties of opals

Modelling studies intended to find realizable designs for a given problem always start with the determination of the optical properties of the host structures and the technical limitations inherent to the fabrication processes. In this section, we review some of the main experimental aspects and basic optical properties of 3D opals, noting that more extensive descriptions of the subject can be found in recent review papers by López [123, 124].

2.1.1 Direct opals

Natural opals are composed of silica (SiO_2) spheres, stacked in a close-packed face-centered cubic (FCC) lattice along the $< 111 >$ direction, as shown on Fig. 2.1(a). This configuration is naturally favored over hexagonal-close-packed structures because it maximizes the total entropy of the stacking [125]. Artificial opals are usually made of silica, polystyrene (PS) or polymethylmetacrylate (PMMA) spheres. They can be used directly as PhCs or can serve as templates for subsequent processes, such as the fabrication of inverse opals.

Various techniques of fabrication are known. Probably the most common one is the vertical deposition technique [126]. A flat substrate is submerged in a colloidal suspension of monodispersed spherical particles and then drawn out at a slow and constant velocity. As the solvent evaporates, the spheres located at the meniscus are deposited on the substrate in a periodic arrangement. This technique has been shown to make up high-quality opals. A recent work has shown that this quality could be further improved by applying acoustic noise vibrations to the sample during the deposition process [127]. Another popular approach to fabricate opals is the spin-coating technique [128], which is usually applied to thin film deposition on flat substrates. Here, the solution of particles is dropped on the rotating substrate and spreads uniformly over the whole surface. Again, the solvent evaporates, leaving the spheres stacked in periodic arrangement. In this process, the number of layers can be accurately controlled with the spinning velocity. This technique allows the fabrication of opals on large scales in a short amount of time but with a reduced quality. Both of the above techniques are complemented by a sintering or heating process, which has the effect of creating small necks between the spheres, providing a certain mechanical stability to the structure.

The photonic band structure of a direct opal made of spheres of refractive index 1.45 is shown on Fig. 2.1(b). The photonic bands have been calculated along the high-symmetry directions of the first Brillouin zone of the FCC lattice, with the planewave expansion (PWE) method. We define the lattice parameter a as the distance between two neighboring spheres. This definition does not follow the usual convention in the literature [48, 129], where a is the edge-length of the cubic structure. In our case, the radius R of the spheres equals $a/2$, instead of the usual $a/2\sqrt{2}$. This convention will be used in the remainder of this chapter.

The photonic band structure exhibits no complete PBG, meaning that there always exists a direction where light can propagate, regardless of the wavelength. The use of higher refractive index spheres does not help in the opening of a complete PBG. Direct opals therefore do not make it possible to confine light in point or linear defects. The partial PBGs on the contrary, which are responsible for the iridescence of natural opals, prohibit light propagation along certain directions at certain wavelengths. Light can then be confined to planar defects normal to these directions, provided that they are designed to resonate in the forbidden range of frequency. The ΓL Bragg gap, found at reduced frequencies a/λ between 0.449 and 0.473, is particularly convenient to use because the corresponding planar defect can be placed in the plane normal to the natural growth direction.

2.1.2 Inverse opals

Compact FCC arrangements of spheres have a filling ratio of about 74 %. The air voids between the spheres are connected to each other so that a fluid can possibly fill the entire structure. The porous character of opals therefore provides an extra parameter to tune their optical properties. Infiltrating direct opals with materials of different refractive indices makes it possible to change their dielectric constrast and eventually invert it, yielding the so-called inverse or inverted opals. Early photonic band

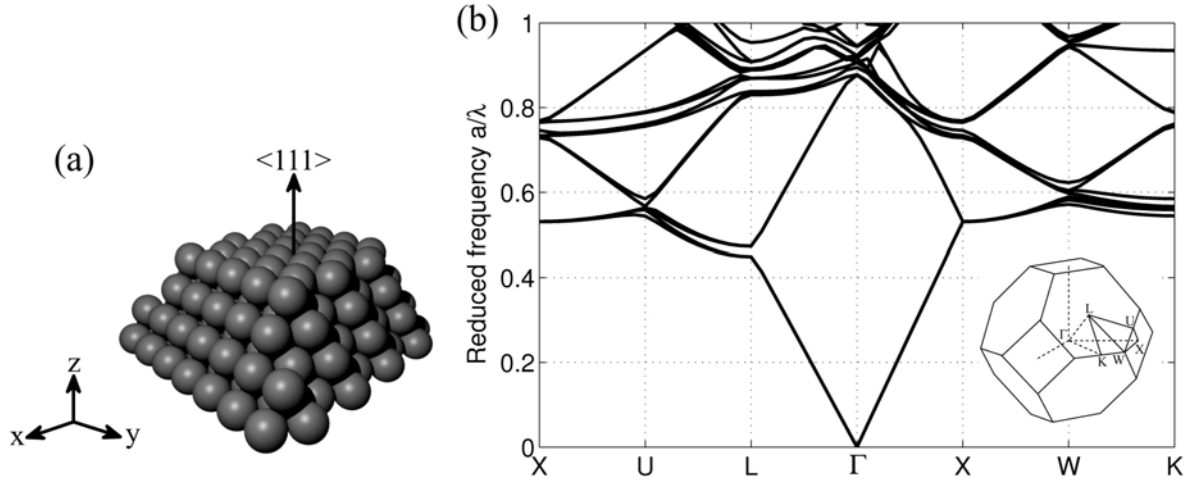

Figure 2.1: (a) 3D view of a direct opal. The layers of spheres are stacked along the $< 111 >$ direction of a FCC lattice. (b) Photonic band structure of a direct opal made of spheres of refractive index 1.45 in air. The inset shows the first Brillouin zone of the FCC lattice. The lattice parameter a is the distance between two neighboring spheres.

calculations showed that they could exhibit a complete PBG, provided that the refractive index contrast between the spheres and the surrounding medium would exceed 2.8 [130]. This finding encouraged experimentalists to develop techniques capable of fabricating high dielectric contrast structures and theorists to envision their use as potential 3D PBG materials.

Many techniques are known to infiltrate direct opals with some other material. Atomic layer deposition, sol-gel and electrochemical methods are some of them. The most common process is the Chemical Vapor Deposition technique [131]. The bare opal is exposed to a specific vapor phase reactant, which undergoes chemical reactions with the opal material to form thin films of the desired material on the surface of the spheres. Layers of different thicknesses can be obtained by varying the gas flow rate, the temperature and the time of exposure in the reaction chamber. This technique preserves the quality of the opal and it can be used for a multitude of different materials, including silicon (Si), germanium (Ge), titania (TiO_2) and zinc-oxide (ZnO). Among those, silicon is probably the most interesting, for it exhibits a large refractive index (close to 3.5) and a low absorption at near-infrared wavelengths, while being the most fundamental constituent of current photonic and electronic technologies. To increase the dielectric contrast of the structure after infiltration, the spheres are removed either by chemical reaction with diluted hydrofluoric acid (HF) for silica opals or by calcination for polymer opals. The proper removal of the spheres over the entire structure is ensured by the necks formed during the sintering process of the direct opal. In this way, silicon inverse opals can reach a dielectric contrast of about 3.5, which is sufficient for them to exhibit a complete PBG [38].

Figure 2.2(c) shows the photonic band structure of a partially-infiltrated inverse opal, as calculated with the PWE method. The structure (see Figs. 2.2(a,b)) consists of a FCC lattice of air spheres, connected to each other by air cylinders of radius $0.2a$ (standing for the small necks between the spheres), surrounded by a silicon shell of thickness $0.125a$ and refractive index 3.45. Theoretical studies have shown that partially-infiltrated inverse opals could exhibit larger PBGs than fully-infiltrated structures, while reproducing a closer picture of experimental templates [132]. This configuration, which has been used by Chutinan *et al.* in their modelling studies [133], is the one that will be considered here.

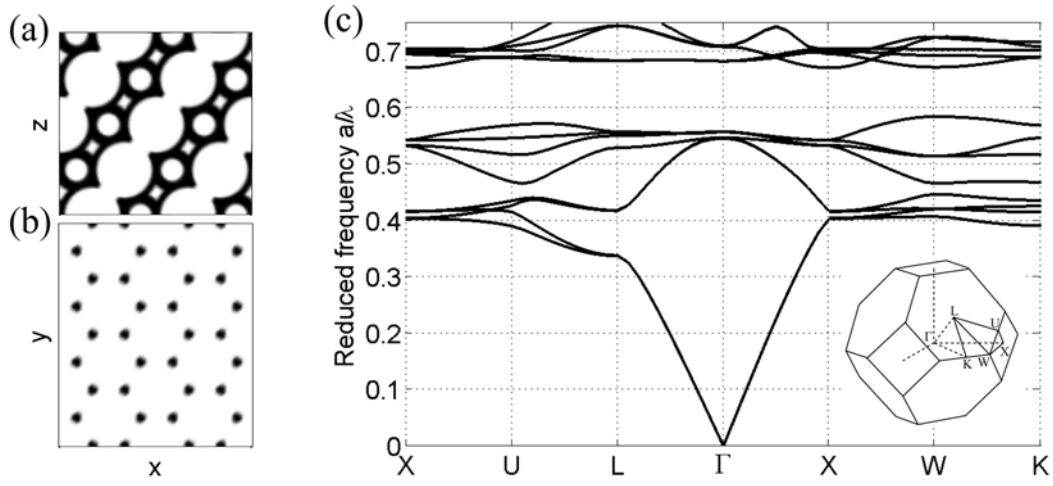

Figure 2.2: Vertical (a) and lateral (b) cross-sectional views of the partially-infiltrated inverse opal described in the text. (c) Photonic band structure of an inverse opal with a backbone material (black shaded area) of refractive index 3.45. The inset shows the first Brillouin zone of the FCC lattice.

The photonic band structure exhibits a complete PBG between the eighth and ninth bands at reduced frequencies a/λ between about 0.58 and 0.66. The relative width, or gap-to-mid-gap ratio, of the PBG is then slightly higher than to 12 % (fully-infiltrated inverse opals exhibit a PBG about 5 % wide). This complete PBG implies that the insertion of defects in the structure can create defect modes lying within the PBG, inferring a full 3D light confinement. The fact that the PBG is found in the higher-order bands of the photonic band structure also suggests that it is very fragile to disorder [134]. Small defects can therefore easily fill the PBG region with modes, making its use impossible. As we will see below, this weakness partly explains the difficulties theorists have to design proper cavities and waveguides.

At the present time, two challenges in particular have to be addressed. First, opal-based PhCs need to be efficiently integrated on photonic chips. Integration is necessary to be able to use these structures in future technologies. Recent studies, which succeeded to grow opals in confined areas, made a step toward this objective [135]. Second, the design and fabrication of proper defects is required to control light emission and propagation in all 3D space. Such defects may find use in low-threshold lasers, waveguides for data transmission systems, optical filters, sensors and so on. Here, we focus on the latter challenge, which, in view of the actual interest for all-optical technologies, is an essential step to be made. It is interesting to note though that it is also possible to use the dispersion bands of opals to control light, with the examples of ultra-refraction [84], supercollimation [136] and negative refraction effects [137].

2.1.3 Defects in opals

There exists numerous different ways to embed defects in opal structures (see e.g. Refs. [71, 138] and references therein). One of them is electron-beam lithography, which has been shown to be an efficient way of structuring opal-based PhCs [139]. The opal growth and insertion of the defects are made in a step-by-step process. A certain number of layers is first grown on a substrate. The top layer of the opal is then exposed to a low-dose electron beam focused on delimited areas and the growth of the opal is resumed to add some additional layers on top of the defect. The opal is finally developed in a solvent to remove the exposed regions. The resulting structure is a direct opal with an embedded defect. Superlattices of defects have recently been realized using this technique [140]. Laser induced

breakdown, which uses femtosecond lasers to damage the material, is another way of patterning sphere monolayers [141]. Once the defects are created, one can eventually proceed to the opal inversion, i.e. the high refractive index material infiltration and sphere removal, which would result in an inverse opal with an embedded defect. It should however be noted that the defect would have the same refractive index as the inverse opal backbone material, e.g. silicon. This may be problematic, as discussed above, since such defects would push far too many modes in the PBG frequency range. Alternative techniques can overcome this issue. For example, it is possible to grow an overlayer of photoresist on top of the lower opal using a spin-coating technique and then pattern it using photolithography or nanoimprint. This approach can be used to fabricate air-core defects in inverse opals. Planar defects have also been created by embedding silica layers in silica-air inverse opals, monolayers of spheres with different diameters, and polyelectrolyte multilayers with active functionalities.

A few years ago, direct laser writing by two-photon polymerization appeared as a very flexible technique, enabling the design of high-quality templates for 3D PhCs [69]. This approach can also be used to insert high-resolution defects into bulk opal structures. A two-photon polymerizable resin is infiltrated in the direct opal and the defect is designed in all 3D space by a laser beam. The unexposed resin is removed by development and annealing of the structure, leaving the 3D embedded defect within the direct opal. The inversion process (material infiltration and removal of oxides and polymers) then results in an inverse opal with a point, linear or planar air-core defect. Rinne *et al.* have recently demonstrated the fabrication of planar cavities and bend waveguides in a silicon inverse opals [142]. This approach makes it possible to create defects that can be much smaller in size than the diameter of the spheres (typically about 1 μm), which is a great advantage regarding our concerns in inverse opals.

However, in spite of these conclusive experimental results, the design of proper defects has been weakly addressed by theorists. Planar defects in direct opals have shown to create defect states in the forbidden range of frequency. Concurrently, the design of point and linear defects in inverse opals has been slowed down by the higher-order character of the complete PBG, making small defects capable of pushing many modes into the PBG. It is known that the electric displacement of electromagnetic fields minimizes its energy by being localized in high refractive index materials, meaning that low refractive index defects can be controlled more easily. Chutinan *et al.* have introduced the concept of 2D-3D heterostructure to create broadband single-mode air-core waveguides [133] and Lousse *et al.* have conducted an optimization study of simple linear defects in inverse opals [143]. Point defects, finally, have been investigated by Chan *et al.*, who proposed to substitute an air sphere of the inverse opal by a SiO_2 sphere of reduced diameter [144]. At the present time, these results have not been confirmed experimentally, for the fabrication of the proposed designs is truly challenging. Theory is basically lacking of efficient solutions for confining light in ways suitable to all-optical technologies. The particularly small number of theoretical papers on defects in opal-based PhCs shows that many points still remain to be investigated.

2.2 Patterned monolayers of spheres

Direct opals have not the ability to confine light to point or linear defects, at least not in stricly 3D structures. As discussed in Sec. 1.1 however, PhC slabs can sustain defect modes by combining the effects of index guiding for out-of-plane confinement and of PBGs below the light line for in-plane confinement. In spite of the radiation losses which occur when the translational symmetry of the structure is broken (e.g. in cavities or waveguide bends), slab-type structures remain interesting candidates for creating ultra-compact and efficient photonic components. In our context, it would be particularly useful to transpose this concept to direct opals. Monolayers of dielectric spheres have received some attention

in recent years [145]. Such structures could be used for example as planar defects in 3D structures, as building blocks for the creation of 2D-3D hybrid architectures or simply as optical filters, waveguides, or other 2D photonic components. Confining light in monolayers of spheres requires us to consider two points:

First, out-of-plane confinement results from the index contrast between the PhC slab and the surrounding medium. Clearly in our case, the use of higher refractive index materials to constitute opals would yield a stronger confinement of light within the structure, which is of course, a benefit. Recent studies report the synthesis of titania spheres with diameters of a few hundreds nanometers with coefficients of variations in size ranging from 5 to 20 % and refractive indices as high as 2.9 [146]. The double inversion technique may also be an alternative for the fabrication of high refractive index direct opals (e.g. silicon) [147]. Second, in-plane confinement and subsequent processes such as the design of waveguides or cavities may require the insertion of defects in the structure. As we have just seen above, specific patterns of defects can be engineered in opals, for example by using electron beam lithography or laser-induced breakdown. These techniques are currently adapted to PMMA and silica spheres in particular but we may expect the development of similar ones for higher-refractive index materials in a near future.

Considering these recent technological advances in synthesizing high refractive index spheres and in creating defects in opal structures, it seems reasonable to study various configurations of monolayers of spheres, looking for a structure that exhibits a PBG below the light line. The presence of a PBG would prohibit the propagation of light in the monolayer and eventually make it possible to confine light to point and linear defects.

2.2.1 Opening of photonic band gaps

Following a natural growth process, monolayers of spheres form a compact hexagonal lattice with the high-symmetry directions being the ΓM and ΓK directions. We consider dielectric spheres of refractive index 2.9, which corresponds to rutile titania material. This choice is of course totally arbitrary. In the following, we also assume that the structure is suspended in air. In practice of course, a substrate would be necessary to hold the structure in place. This would create in a vertical asymmetry of the structure, which would destroy the even and odd parity of the modes and consequently result in mode-mixing issues. This effect can however be relatively weak depending on the strength of localization of the field in the monolayer and on the perturbative polarization [148]. Alternatively, symmetry could be re-established by adding a superstrate on top of the monolayer or by filling it entirely by a low-index material.

Compact monolayers of spheres do not exhibit a significant PBG below the light line either in the even or in the odd modes, because of symmetry and accidental degeneracies. Those cannot be lifted up by increasing the dielectric contrast of the structure but it has been demonstrated that changes in the unit cell of a 2D hexagonal lattice of cylinders can yield the opening of new PBGs [149]. Changing the lattice of a structure actually results in multiple foldings of the Brillouin zone and in the lifting of degeneracies at its edges. We propose a configuration that can be obtained by removing dielectric spheres in a hexagonal pattern, as shown on Fig. 2.3(a). Figure 2.3(b) sketches the photonic band structure of the even modes of the patterned monolayer of spheres. It exhibits a PBG between the first and second bands, centered on a reduced frequency $a/\lambda = 0.214$ and of a relative width of 12.4 %. The PBG can be tuned to the wavelength $\lambda = 1.55$ μm by using titania spheres of diameter 0.33 μm. As shown on Fig. 2.3(c,d), the creation of a superlattice of air defects in the monolayer of spheres forces the higher-order mode to enter the air region, resulting in a large energy shift and thus, in the opening of a PBG.

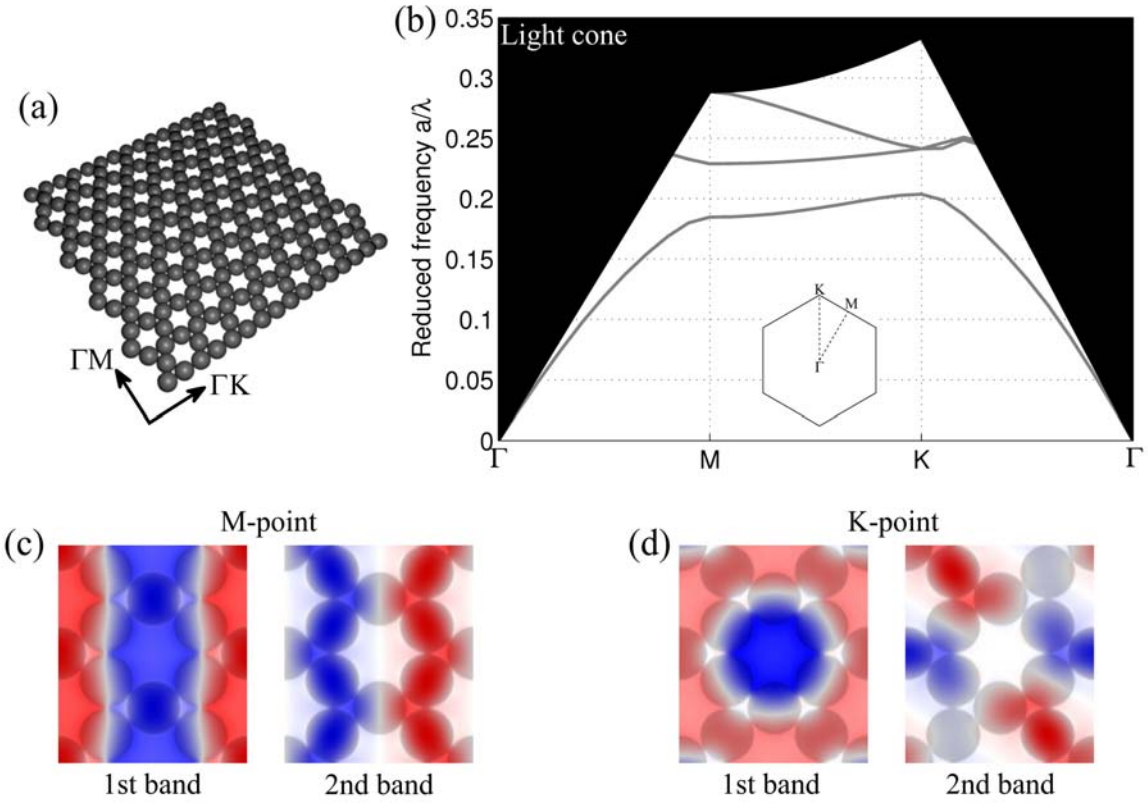

Figure 2.3: (a) 3D view of a monolayer of spheres with a hexagonal superlattice of defects (b) Photonic band structure of the patterned monolayer of spheres in the even modes. (c,d) H_z field in the lateral cross-section of the monolayer for the first and second modes at the M- and K-points of the reciprocal lattice, respectively.

To generalize this result to spheres of different materials, we map the position and width of the PBG as a function of the refractive index of the spheres. A gap map of the patterned monolayer of spheres is given in Fig. 2.4 for the even modes. The PBG that we consider here exists for spheres of refractive indices greater than about 1.9. Since the higher the refractive index of a material, the lower the frequency of its modes, the PBG becomes wider (up to about 15 % with spheres of refractive index 3.5, corresponding to silicon) and is pushed down in frequency with the increase of the refractive index. Consequently, the PBG spans a larger reciprocal area, lessening the out-of-plane radiation. Smaller PBGs that appear at higher frequencies have not been reported here because we considered them to be too small to our concerns. To demonstrate the functionality of the hexagonal superlattice monolayer, let us now investigate the possibility of creating waveguides and cavities in them.

2.2.2 Waveguides and cavities

The design of waveguides and cavities in PBG structures is usually not straightforward. Intense modelling efforts may be required to obtain the desired effects. Small variations of the size, shape and refractive index of the defects can yield large changes of the optical properties of the resulting waveguides or cavities. In our case, since the patterned structure was made by removing specific spheres in a hexagonal pattern, the simplest way of creating defects is simply to leave some of them intact.

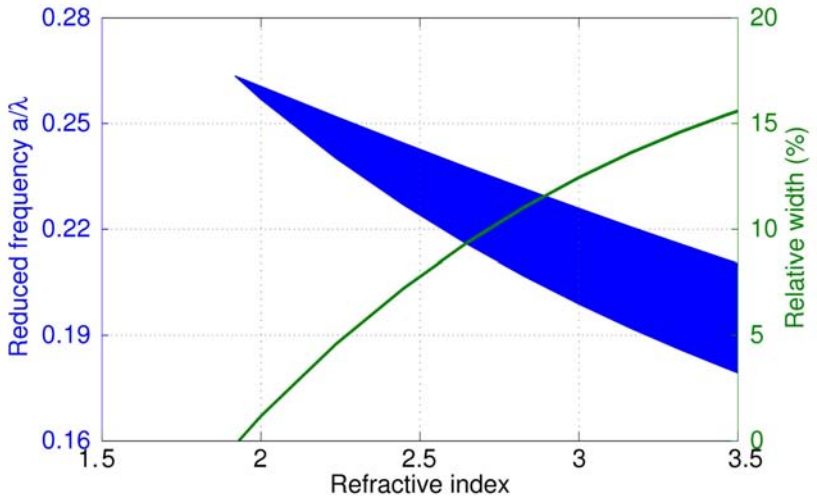

Figure 2.4: Map of the PBG appearing between the first and second even modes of the patterned monolayer of spheres. The position in reduced frequency (blue shaded area) and relative width (green solid curve) of the PBG are given as a function of the refractive index of the spheres.

W1-like waveguide

We propose to create a waveguide by leaving one row of spheres along the ΓK direction of the hexagonal superlattice structure defined above (see Fig. 2.5(a)). Since the dielectric spheres are removed from a close-packed monolayer in a triangular pattern, we may define this kind of linear defect as a W1-like waveguide. Figure 2.5(b) sketches the photonic band structure of the even modes along the ΓK' direction. The dark gray shaded areas defines the continuous region corresponding to all the possible frequencies of the sphere monolayer, i.e. where light can propagate laterally. The insertion of the linear defect gives rise to two non-degenerate modes within the PBG with reduced frequencies $a/\lambda = 0.204$ and 0.214 at the K'-point. The corresponding field patterns in Figs. 2.5(c,d) show that light is indeed well confined to the monolayer by the light cone and to the linear defect by the PBG. Following our remark above, we also note that the field patterns are very close to the ones obtained in dielectric slab W1-waveguides [150].

L3-like cavity

Resonant cavities can be created in a similar manner. We consider a closed linear defect, consisting of three spheres, aligned along the ΓK direction of the lattice (see Fig. 2.6(a)). By analogy with triangular lattices of holes in PhC slabs, this kind of defect may be defined as a L3-like cavity [55]. The resonant frequencies of the structure have been extracted by harmonic inversion of the temporal signal in the 3D FDTD method. The opal-based cavity exhibits a single resonant mode, shown on Fig. 2.6(b), with the even parity within the PBG frequency range. It resonates at the wavelength $\lambda = 1.553$ μm, for spheres of refractive index 2.9 and diameter 0.33 μm. The out-of-plane component of the quality factor is $Q = 265$, which is particularly low compared to the quality factors obtained in PhC slabs ($Q \simeq 45000$). Although resonant cavities with low quality factors are not be adapted to frequency-selective devices, they could find use in applications where coupled radiation and interaction is important, such as the enhancement of fluorescent emission from quantum dots [151]. They are also known to improve the bending efficiency of waveguides in 2D PhCs [152], so that this cavity could eventually enhance the functionality of the opal-based waveguide studied above.

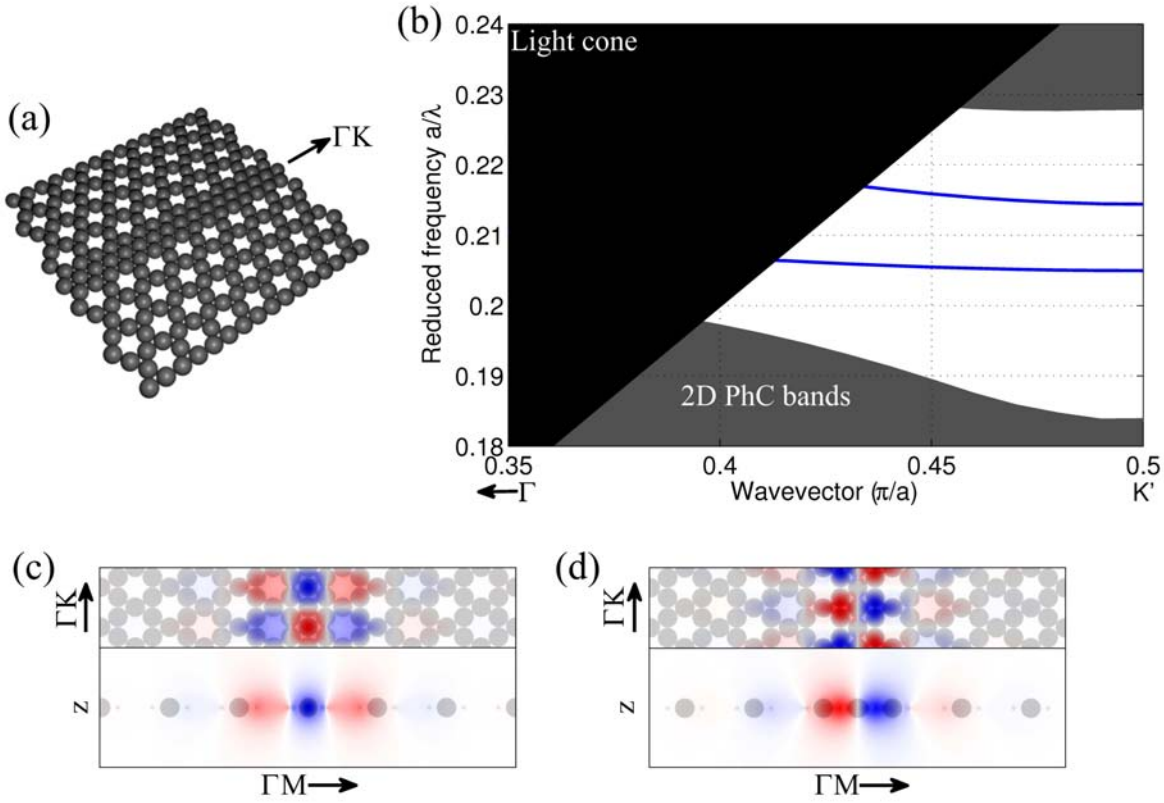

Figure 2.5: (a) 3D view of a W1-like waveguide in a patterned monolayer of spheres directed along the ΓK direction of the lattice. (b) Photonic band structure of the waveguide. The blue solid curves are the waveguide modes. The black and gray shaded areas define the light cone of air and the projected bands of the monolayer, respectively. (c,d) H_z field of the lower- and higher-order waveguide modes at the K'-point of the reciprocal lattice, respectively.

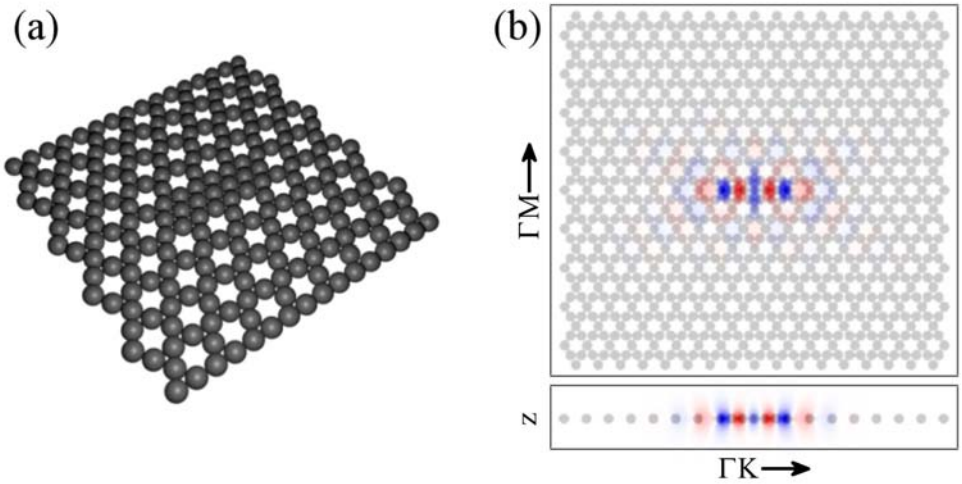

Figure 2.6: (a) 3D view of a L3-like cavity in a patterned monolayer of spheres. (b) H_z field of the cavity mode at the wavelength $\lambda = 1.553$ μm.

In summary, patterned monolayers of spheres can exhibit a PBG below the light line and support waveguides and cavities. To our knowledge, this is the first demonstration of light confinement to cavities and waveguides in direct arrangements of spheres (apart from planar cavities). Different applications may be envisaged. For example, by mixing patterned monolayers with compact defectless monolayer of spheres, it may be possible to confine light in certain specific regions of space in order to obtain the functionalities that we expect from 2D PBGs, e.g. mirrors. Alternatively, the waveguides may be used to insert or collect light from a 3D structure in a 2D-3D hybrid architecture. Such an approach is however unavoidably limited in terms of efficiency by the "imperfect" index guiding confinement of light. A full confinement requires to use a 3D PhC that exhibits a complete PBG. Inverse opals meet the necessary requirements for this task. This is the subject of the next sections.

2.3 Two- and three-dimensional heterostructures based on inverse opals

As discussed in Sec. 2.1, a large panel of different experimental techniques have been developed to design various kinds of planar, linear and point defects in opal-based PhCs, but very little has been made on the theoretical level. The design of proper defects, i.e. broadband single-mode waveguides and high quality factor cavities, remains a real challenge due to the high-order character of the PBG. To address this problem, it has been proposed to use 2D-3D heterostructures, which consist of a 2D PhC layer sandwiched between two 3D PBG structures. The extra parameters of the structure can be used to enhance the tunability of their optical properties. Obviously, the fabrication of such structures is expected to be particularly difficult, requiring a very accurate alignment of the 2D and 3D PhCs. It seems also that the description of the physics underlying the confinement processes in 2D-3D heterostructures has not been brought to an end. This should therefore be our starting point.

2.3.1 Principles and design

The concept of 2D-3D heterostructures has been introduced by Chutinan *et al.* a few years ago [153]. A 2D PhC layer of finite thickness is intercalated between two 3D PhCs that exhibit a complete PBG. In the PBG range of frequency, the 3D claddings confine the light to the planar PhC, which can then be designed in a more conventional way according to one's need. Single-mode waveguiding has been demonstrated in silicon inverse opal-based heterostructures with a maximal waveguiding bandwidth of 74 nm centered on 1.55 μm, which seems rather small as compared to the bandwidths obtained with other 3D PBG structures (up to about 180 nm) [154]. In this study, the bandwidth of the single-mode seemed to be limited by the photonic bands of the 2D PhC layer. Changing the lattice parameters and/or the position of this layer with respect to the inverse opal claddings is therefore expected to have a strong influence on the waveguiding properties of the 2D-3D heterostructure.

The 3D PhC cladding that we consider here is the inverse opal structure that has been considered by Chutinan *et al.* and by us in Sec. 2.1. It consists of a close-packed FCC lattice of air spheres of radius $0.5a$, where a is the distance between the center of two adjacent spheres, surrounded by silicon spherical shells of thickness $0.125a$ and refractive index 3.45. The spheres are connected by cylindrical windows of radius $0.2a$. The photonic band structure of this inverse opal is given in Fig. 2.2(b). The complete PBG of the inverse opal is centered on a reduced frequency $a/\lambda = 0.62$ and has a relative width of about 12 %.

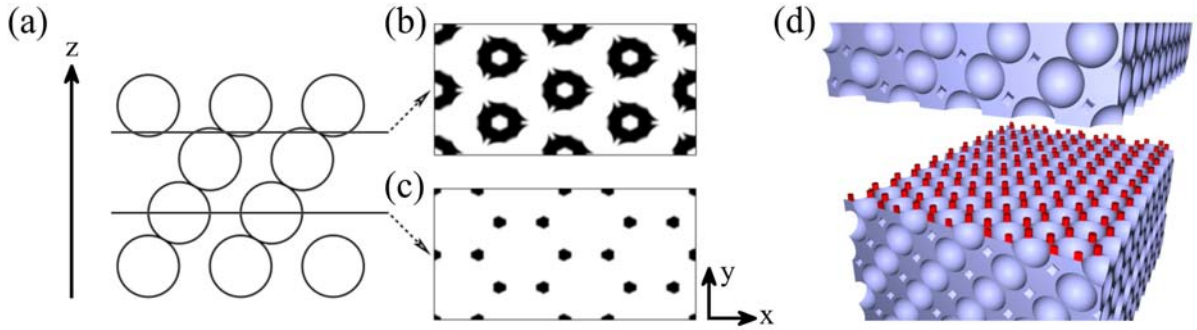

Figure 2.7: (a) Sketch view of an opal structure. Lateral cross-sectional views of the partially-infiltrated inverse opal halfway between two layers of spheres (b) and in the middle of a layer of spheres (c). The black shaded areas correspond to the high refractive index material. (d) 3D view of the 2D-3D heterostructure. The dielectric rods (in red) constituting the 2D PhC layer are sandwiched between two 3D inverse opal claddings (in blue).

The 2D layer proposed by Chutinan *et al.* consists of a triangular arrangement of silicon rods in air. For the sake of experimental feasibility, the rods of the 2D layer have to be placed on the dielectric regions of the 3D inverse opals, requiring the periodicity of both PhCs to be similar. Moreover, in order to stay close to the experiment, the 2D layer lies on the (111) plane of the FCC lattice, on which opals naturally stack. Figures 2.7(a-c) show cross-sectional views of the inverse opal structure at different heights along its growing direction. The inclusion of a 2D triangular lattice of rods has been made at the position shown on Fig. 2.7(b), which corresponds to a cut halfway between two layers of spheres. For periodic arrangements of dielectric rods in lower refractive index backgrounds, it is known that the graphite lattice can exhibit larger PBGs than the triangular one [149]. The 2D-3D heterostructure could then exhibit a larger PBG, offering a larger spectral range for the single-mode to spread on. The position on Fig. 2.7(c), which corresponds to a cut in the middle of a layer of spheres, exhibits a graphite pattern of dielectric material, making it possible to insert a graphite lattice of rods. A 3D view of the heterostructure obtained is shown on Fig. 2.7(d).

Figure 2.8 shows the photonic band structure of a 2D-3D heterostructure with rods of radius $r = 0.1a$ and a 2D layer thickness $t = 0.2a$. The insertion of the 2D PhC layer introduces some modes within the complete PBG of the 3D inverse opal. These 2D PhC bands are the dispersion curves of the graphite lattice of rods, superimposed over the projected bands of the 3D inverse opal. In the frequency range where they do not overlap, light is allowed to propagate in the 2D PhC layer only. The remaining PBG, called on-chip PBG, is the frequency range where light cannot propagate at all through the 2D-3D heterostructure, corresponding to the frequency range where a full 3D confinement of light is possible.

According to the photonic band structure on Fig. 2.8, the width of the on-chip PBG is limited by the 2D PhC bands. In view of designing broadband waveguides, one should maximize the on-chip PBG by tuning the 2D layer parameters. Since the periodicity of the 2D layer and the refractive index of the rods are fixed by the inverse opal parameters, this optimization can only be made by tuning the rod radius r and the layer thickness t as parameters of the heterostructure. Figures 2.9(a,b) sketch the on-chip PBG position in reduced frequency as a function of t (with fixed $r = 0.1a$) and r (with fixed $t = 0.2a$), respectively. As we would expect, in the limit of null thickness of the 2D layer ($t = 0$), the on-chip PBG corresponds to the PBG of the 3D inverse opal. When the layer thickness is increased, the 2D bands are pushed down to lower frequencies, entering the 3D PBG. Thicker PhC slabs can indeed support more confined modes. The variation of the on-chip PBG at fixed thickness $t = 0.2a$ with the radius is now

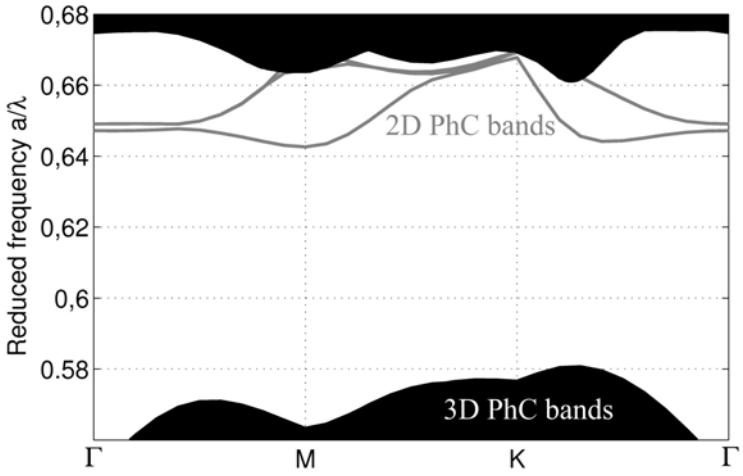

Figure 2.8: Photonic band structure of the 2D-3D inverse opal heterostructure. The on-chip PBG is the frequency range that is neither covered by the projected bands of the 3D inverse opal (black shaded area), nor by the 2D PhC bands (gray solid curves).

slightly different. In the limit where no rods are present ($r = 0$), the 3D PBG is completely filled by the 2D bands. This is normal since light propagates freely in air. The 2D PBG opens for rod radii above about $0.03a$, and is continuously pushed down to lower frequencies with the increase of r, following an increase of the high refractive index material filling ratio. The optimal overlap of the 2D and 3D PBGs is found for rod radii close to $0.10a$. This brief optimization study of the on-chip PBG of the 2D-3D heterostructure can now be used to design a broadband single-mode waveguide.

2.3.2 Broadband single-mode waveguide

An air waveguide can be realized by removing rods along the ΓK direction of the structure (see Fig. 2.10(a)). The radius of the rods is set to $r = 0.1a$ and the thickness of the layer to $t = 0.2a$. The dispersion relation of the corresponding waveguide are shown on Fig. 2.10(b). The upper single-mode ranges from 0.586 to 0.637 in units of reduced frequency (a/λ), corresponding to a bandwidth of 129 nm centered on 1.55 μm. This bandwidth is 74 % larger than the maximal bandwidth reported in the triangular case (74 nm). The single-mode extends over almost the whole on-chip PBG, which itself occupies a large part of the inverse opal 3D PBG. This significant improvement of the bandwidth is therefore truly due to the widening of the on-chip PBG by the graphite lattice.

This is further verified by studying the dependence of the single-mode waveguiding bandwidth with the 2D PhC layer parameters. As shown on Fig. 2.11, the bandwidth remains larger than the optimal one obtained in the triangular case (74 nm) on almost the whole range of study, emphasizing the significant advantage of graphite lattices of rods over triangular ones. The single-mode waveguiding bandwidth is maximized for rod radii close to $r \simeq 0.1a$ and naturally decreases for larger radii, as a consequence of the closing of the on-chip PBG by the 2D bands. The thickness dependence of the bandwidth is moderate. For a rod radius close to $r \simeq 0.1a$, it remains above 100 nm on the whole range of study. Increasing the thickness of the 2D layer increases the intrinsic bandwidth of the waveguide mode. For layer thicknesses above $t = 0.2a$, the on-chip PBG becomes smaller than the single-mode and thus, reduces its waveguiding bandwidth.

The single-mode waveguiding bandwidth therefore relies on an interplay between the intrinsic band-

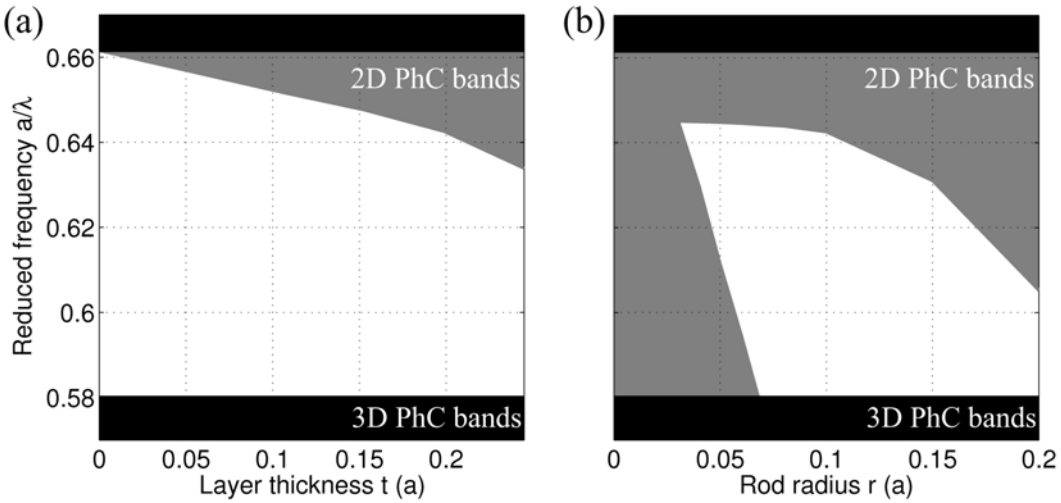

Figure 2.9: Map of the on-chip PBG of the 2D-3D heterostructure with respect to (a) the layer thickness t with $r = 0.1a$ and (b) the rod radius r with $t = 0.2a$. The black and gray shaded areas are the frequency regions filled by the 2D and 3D PhC bands, respectively.

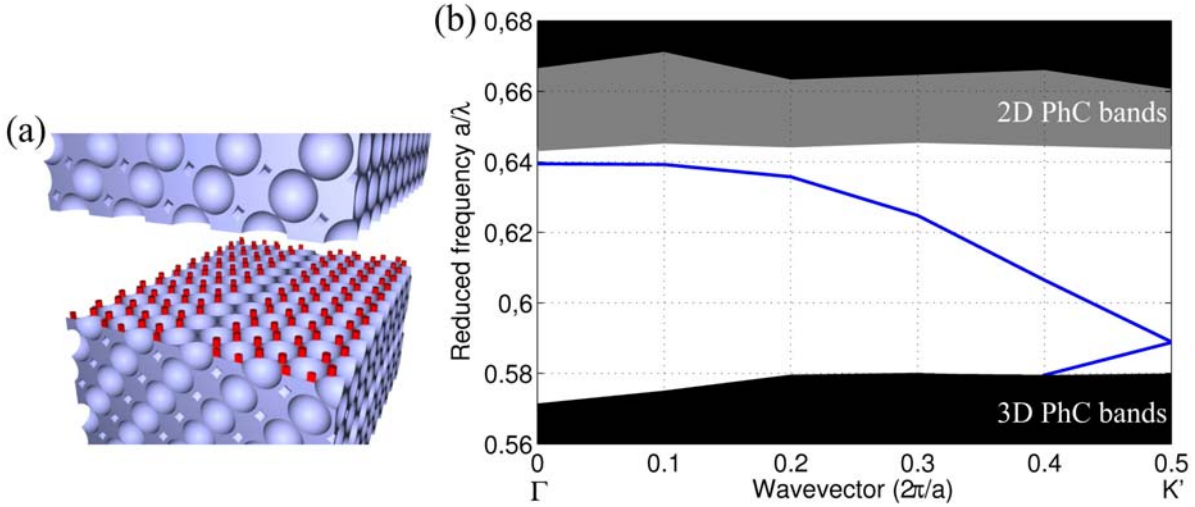

Figure 2.10: (a) 3D view of the single-mode waveguide in the 2D-3D heterostructure.(b) Photonic band structure of the waveguide. The blue solid curves are the waveguide modes. The gray and black shaded areas correspond to the projected bands of the 2D and 3D PhCs, respectively.

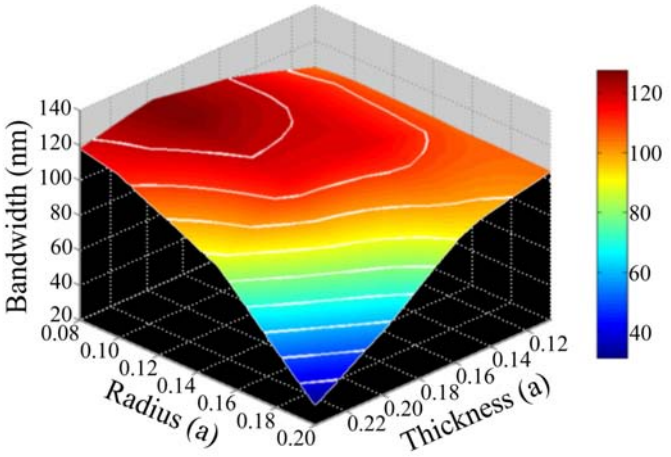

Figure 2.11: Single-mode waveguiding bandwidth of the 2D-3D heterostructure waveguide as a function of the layer thickness t and rod radius r of the 2D PhC layer. The white lines drawn on the bandwidth surface are contours delimiting bandwidths from 40 to 120 nm in steps of 10 nm.

width of the single-mode and the width of the on-chip PBG. By using a graphite lattice of rod, which is known to exhibit larger PBGs than triangular ones, we could widen the on-chip PBG of the 2D-3D heterostructure and thus, create a larger available spectral range. Some points however remain to be clarified here. In particular, it is worth noting that the rod radius that optimizes the on-chip PBG width and the single-mode waveguiding bandwidth makes the rods match perfectly to the dielectric pattern of the inverse opal. Similarly, Chutinan *et al.* remarked that the structural match between the cross-section of the 2D and 3D structures plays an important role in the design of heterostructures [155]. The optimal design for the 2D layer is actually found to be the extruded cross-section of the 3D structure. Furthermore, as we have seen above, the thinner the 2D layer, the larger the on-chip PBG. In this work, as well as in the initial study of Chutinan *et al*, the defect contituting the linear waveguide has been assumed to have the same height as the thickness of the 2D PhC layer. Such a condition ensures that the defect mode behaves in the intercalated layer in a similar way as in the 2D finite-thickness PhC. Based on our understanding of light confinement processes in 2D-3D heterostructures, it is very tempting to suggest that similar effects, i.e. similar waveguide modes, can be observed in purely 3D structures, provided that the cross-section of the structure in the propagation plane locally resemble a 2D PhC layer of finite thickness.

2.4 Purely three-dimensional inverse opals

One of the major requirements that has been pointed out at the beginning of this chapter is the necessity to design defects attainable experimentally. In this regard, creating defects in purely 3D structures should be our first option. This approach has been limited up to now by the accuracy in the size and shape of the defects suitable to the design of broadband single-mode waveguides and cavities [143,144]. Now, it is true that waveguides in 2D-3D heterostructures have been shown to exhibit stable broadband single-modes and certainly, such structures would demonstrate remarkable features for telecommunication purposes. Unfortunately, as noted above, they are expected to be quite challenging to realize, in addition to which they would require a many-step fabrication process including an accurate alignment between the different stacked structures, thereby loosing any benefit of rapid self-assembly techniques. Nonetheless, they have provided us with a non-negligeable hint on the formation of defect modes in inverse opals. As a matter

of fact, the idea briefly exposed above has some connections with previous studies.

In 2000, Johnson and Joannopoulos proposed the design of a 3D layered PhC with a large complete PBG [42]. This structure consists of alternating layers of triangular lattices of dielectric rods in air and of air holes in dielectric, stacked in a FCC lattice. The concept underlying this design is that the dispersion properties of the 3D PhC in the plane normal to the stacking direction closely look like those of the corresponding 2D PhCs, and in this sense, greatly simplify the understanding of defect modes. Waveguides and cavities could indeed be engineered in the 3D PhC according to their 2D counterpart [156]. The resulting defect modes have been shown to be mostly E- or H-polarized, depending on whether the defect was located in a rod-type or in the hole-type layer.

Now, the connection with inverse opals is quite straightforward. Considering that the cross-sections of the 3D structure are 2D PhCs with complete PBGs, waveguides and cavities may be designed in a very simple manner from their 2D counterpart. The defects are created in the (111) plane of the opal structure, in the middle of a layer of spheres to benefit from the large PBGs of graphite lattices of rods. The rods constituting the 2D PhC have a radius $r = 0.1a$, where a is the lattice parameter, which corresponds very well to the dielectric pattern of the inverse opal cross-section. Since rod-type structures are more likely to exhibit PBGs when the electric field is parallel to the axis of the rods, light in the 2D calculations is assumed to be E-polarized.

2.4.1 Waveguides

Figure 2.12(a) sketches the photonic band structure of a linear waveguide in the 2D PhC, made by removing one row of rods along the ΓK direction of the hexagonal lattice. It exhibits a defect mode ranging from $a/\lambda = 0.585$ to 0.618 within its PBG. We create the same kind of defect in the 3D inverse opal by removing some dielectric in the structure on a thickness $t = 0.3a$. The corresponding photonic band structure is shown on Fig. 2.12(b). As expected, a very similar mode appears within the 3D PBG at reduced frequencies between $a/\lambda = 0.62$ and 0.628. Comparing the field patterns of the 2D and 3D waveguide modes at the K-point in the insets of Figs. 2.12(a,b) also demonstrates the similarity of the confinement processes in the 2D and 3D structures. The overlap of the horizontal cross-section of the 3D and 2D modes shows that the 3D mode is mostly E-polarized, as expected.

This approach is obviously not limited to one particular kind of defect. We reproduce the above photonic band calculations on a linear waveguide made by removing two rows of rods along the ΓK direction of the hexagonal lattice. This defect is the same as the one defined in the 2D-3D heterostructures in the previous section, so that similar waveguide modes are expected to appear. The photonic band structures of the 2D and 3D PhCs are shown on Figs. 2.13(a,b). Here again, the dispersion of the waveguide modes match remarkably well. The PBG is entirely covered by two single-modes, degenerate at the K'-point of the hexagonal lattice Brillouin zone. The waveguide actually remains single-mode accross its entire spectral range. The defect mode can be tuned to lower (resp. higher) frequencies by decreasing (resp. increasing) the thickness of the air defect. The dispersion relations of the waveguide modes in the case where dielectric has been removed from the inverse opal on a thickness $t = 0.1a$ is shown in dashed curves. Since a larger part of the waveguide mode enters the high refractive index region, the bands are shifted to lower frequencies. The upper mode spans a relatively large spectral range, from $a/\lambda = 0.597$ to 0.641, corresponding to a bandwidth of 110 nm centered on the wavelength $\lambda = 1.55$ μm. As expected, this defect mode is almost the same as the one that was found in 2D-3D heterostructures. Although its bandwidth is slightly smaller than previously (128 nm), it remains largely sufficient for many applications in the telecommunications and far more accessible from an experimental

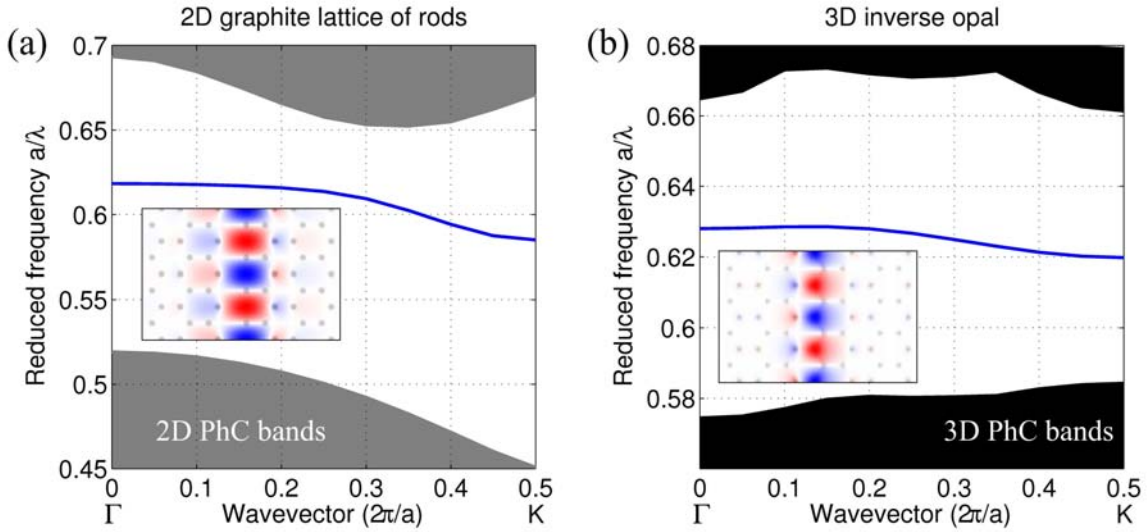

Figure 2.12: Photonic band structures of a single-mode waveguide in a 2D graphite lattice of rods (a) and a 3D inverse opal (b). The rods have a refractive index 3.45. The waveguide has been made by removing one row of rods along the ΓK direction of the structure, on a thickness $t = 0.3a$ for (b). The gray and black shaded areas are the projected bands of the 2D and 3D PhCs. The insets show the E_z field of the modes at the K-point of the reciprocal lattice.

point of view. Figure 2.13(d) shows the field pattern of the upper waveguide mode at the K-point of the lattice for $t = 0.1a$. The 3D mode is mostly localized in the air regions of the structure, which suggests that coupling from the ambient medium may be efficient.

Typically, such defects could be created by direct laser writing (see description in Sec. 2.1). For operation at a wavelength $\lambda = 1.55$ μm, the spheres need to be of the order of $a = 0.96$ μm, which can be easily obtained with current opal growth techniques. The typical size of the defects should then range from about 100 to 300 nm in thickness, which is attainable experimentally according to recent papers [142]. Figure 2.13(c) shows the linear defect that has to be inserted in the direct opal before inversion. It is also worth noting that the formation of small necks between the spheres and the degree of infiltration of the opal by silicon are both parameters that have to be carefully considered. As a matter of fact, fully-infiltrated structures exhibit much smaller PBGs. Our study provides some insight onto this phenomenon in a simple way, remarking that the dielectric pattern of the cross-section of fully-infiltrated inverse opals by itself is not favorable to the existence of large PBGs. The design of broadband single-mode waveguides is also more complicated in this case.

2.4.2 Cavities

A similar approach can now be used to create resonant cavities. To our knowledge, the only design of a cavity in a 3D inverse opal is the one proposed by Chan *et al.* [144], consisting of replacing an air sphere by a sphere of slightly higher refractive index (close to 1.5, corresponding to silica, PS or PMMA) and reduced size. In practice, supposing that spheres of different types could be mixed before the opal growth, one could fabricate opal structures with randomly-placed point defects, probably yielding some anomalous transport properties, which would surely be interesting to study. This approach is however not adapted to the fabrication of photonic technologies with well-controlled features.

We consider a simple defect consisting of one missing rod in the 2D graphite lattice of rods considered above. The corresponding photonic band structure is shown in Fig. 2.14(a). A single defect mode is

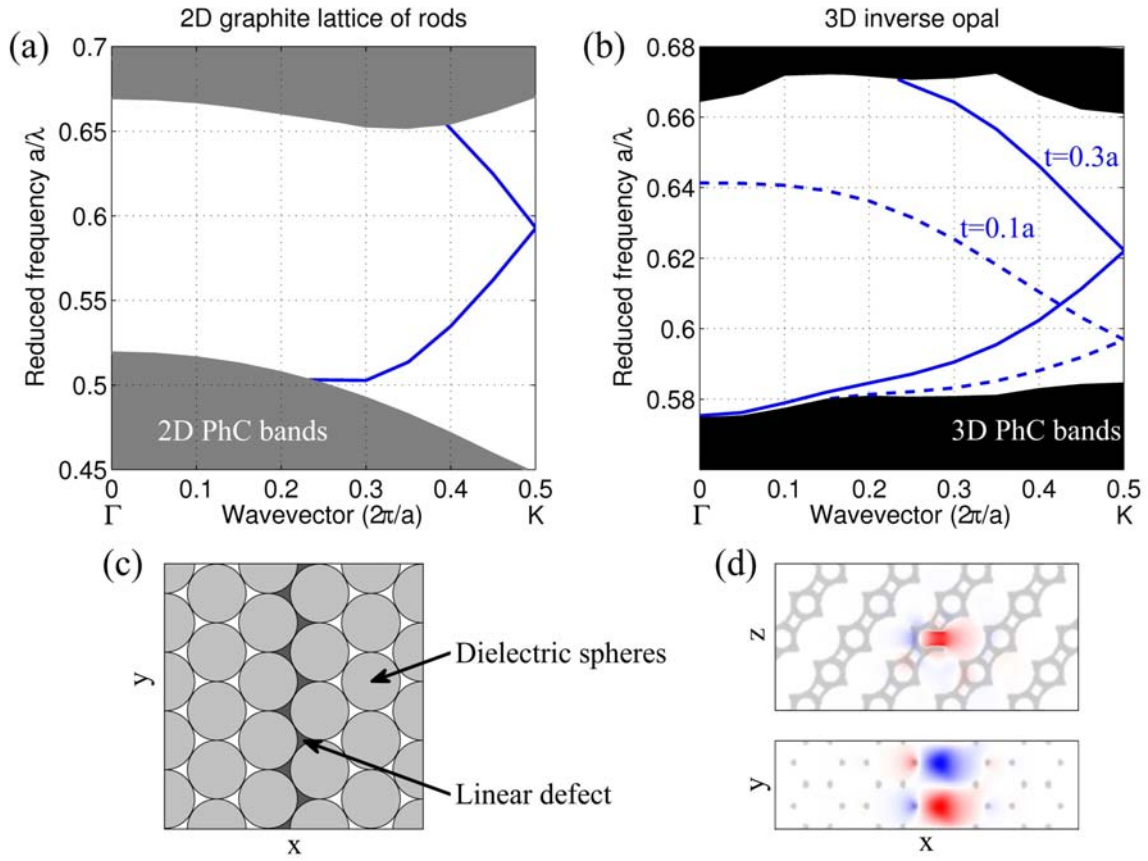

Figure 2.13: Photonic band structures of a single-mode waveguide in a 2D graphite lattice of rods (a) and a 3D inverse opal (b). The waveguide has been made by removing two rows of rods along the ΓK direction of the structure, on a thickness $t = 0.3a$ (blue solid curves) and $t = 0.1a$ (blue dashed curves) for (b). The gray and black shaded areas are the projected bands of the 2D and 3D PhCs. (c) Design of the linear defect in the direct opal before inversion. (d) E_z field of the upper waveguide mode of the 3D inverse opal with $t = 0.3a$ at the K-point of the reciprocal lattice.

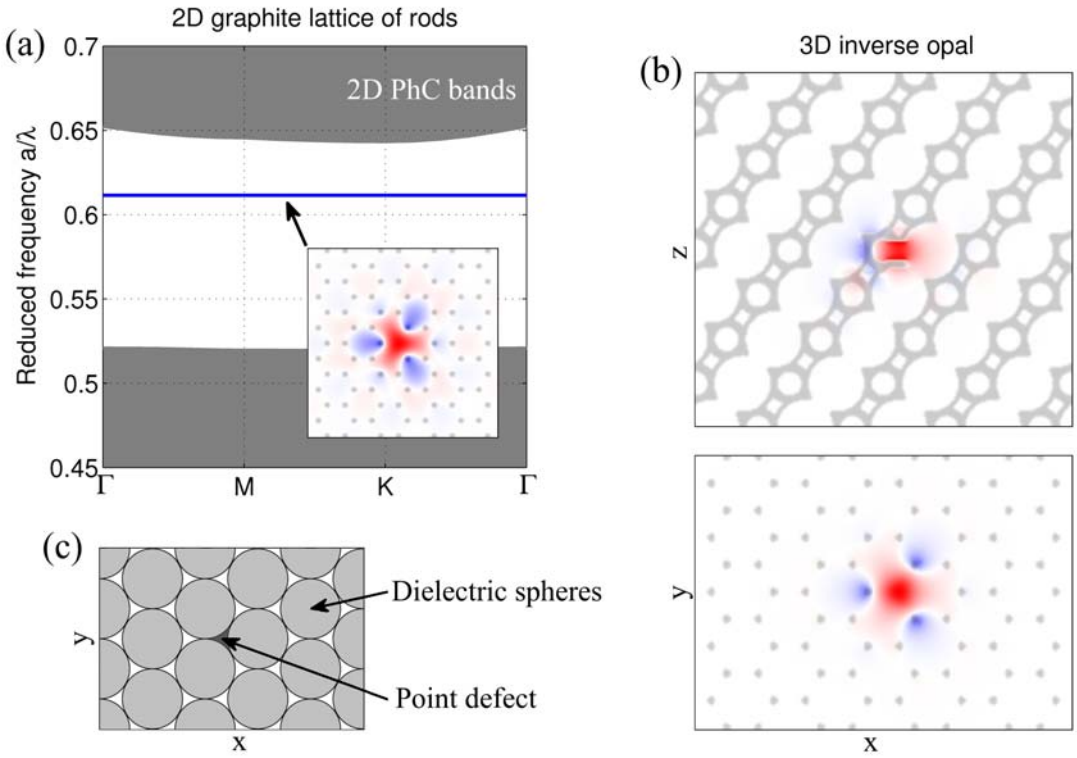

Figure 2.14: (a) Photonic band structure of a cavity in a 2D graphite lattice of rods. The inset shows the E_z field of the cavity mode. (b) E_z field of the cavity mode in the 3D inverse opal. The defect has a thickness $t = 0.3a$. (c) Design of the point defect in the direct opal before inversion.

found within the PBG at a reduced frequency $a/\lambda = 0.612$. Its field pattern is shown on the inset of the figure. The same defect is now created in the 3D bulk inverse opal on a thickness $t = 0.3a$. Since the computation of the photonic bands using the PWE method is far too memory and time-consuming, this calculation has been made using the 3D FDTD method. A single defect mode is found within the PBG, resonating at a reduced frequency $a/\lambda = 0.625$. The field pattern of the mode, shown on Fig. 2.14(b), also closely resemble that of its 2D counterpart and it remains mostly localized in the air region. As for waveguides, the resonant frequency of the cavity can be changed by varying the thickness of the defect.

This last step further validates our initial guess on the processes of light confinement in 3D inverse opals. We have proposed here a simple technique to design resonant cavities and broadband single-mode waveguides in 3D inverse opals. Both types of defects can possibly be fabricated by direct laser writing on a single 3D inverse opal, requiring no step-by-step growth process, and may be combined to create highly efficient and large-scale photonic components for the telecommunications, quantum information processing, and so on, at low cost. It is finally worth noting that this approach may be extended to a larger variety of defects, including some designed in different propagation planes to make full use of the three-dimensionality of the PhC. This is, after all, one of the many advantages of 3D PhCs.

Summary

In this chapter, we have presented various solutions to the confinement of light in opal-based PhCs. We have started by reviewing some of the main techniques known to date to fabricate opals and engineer defects in them, in order to have a broad view of the actual state-of-the-art on the experimental level.

First, we have shown that monolayers of spheres with a superlattice of defects can exhibit a PBG below the light line, so that waveguides and cavities could be designed. Then, we have optimized a 2D-3D heterostructure based on inverse opals and have demonstrated single-mode waveguiding over a bandwidth of 128 nm centered on 1.55 μm. This constitutes an increase of the bandwidth of more than 70 % compared to previous results. Finally, we have proposed a novel approach to design waveguides and cavities in 3D inverse opals based on a study of their 2D cross-section. In this way, we could design a single-mode cavity and air-core single-mode waveguides, the optimal one having a maximal bandwidth of about 110 nm centered on 1.55 μm. The designs of structural defects proposed in this chapter (in patterned monolayers of spheres and 3D inverse opals) are simple in shape and can possibly be fabricated with current techniques.

Chapter 3

Enhanced dispersion-based waveguiding in photonic crystals

Broadly speaking, photonic crystals (PhCs) owe their original optical properties from their strong dispersion, leading to a local modification of the group velocity of light or even the prohibition of its propagation. In the early years of PhCs, researchers have mainly focused on the photonic band gap (PBG) properties of PhCs and consequently on their ability to confine light to structural defects such as waveguides and cavities. A more recent approach of manipulating light is based on the spatial dispersion of PhCs. Here, the dispersion curves of an extended, i.e. defectless, PhC are used to control the direction of propagation of light. The extremely strong anisotropy of the bands can provide a multitude of very exotic effects, such as supercollimation [73], ultra-refraction [80] or negative refraction [88] and thus, bring up new functionalities to PhCs. These effects have been intensively studied in the past few years and are now well understood.

The purpose of this chapter is to enhance the features of extended PhCs, i.e. make them more flexible and reliable on the manipulation of electromagnetic fields, and in particular on the propagation of light beams. Although important efforts have been made recently on three-dimensional (3D) PhCs (see Chapter 2), we will focus on two-dimensional (2D) PhCs, for the simple reason that they can be more easily integrated on conventional platforms (e.g. silicon-on-insulator (SOI) substrates), and thus can provide a faster way of conciliating our theoretical predictions with potential future experiments. In Sec. 3.1, we will show that PhCs with a gradient in their lattice parameter, namely graded PhCs, can manipulate light beams in an original way. This concept will be verified by comparison with an experiment made by E. Akmansoy and J.-M. Lourtioz at the Institut d'Electronique Fondamentale, demonstrating a mirage effect in the microwave range. In Sec. 3.2, we will propose an efficient and practical way to improve the coupling of light from integrated SOI-based waveguides to supercollimating PhCs. This will give some insight onto the light coupling mechanisms to extended PhCs in general.

3.1 Beam propagation in graded photonic crystals

Extended PhCs exhibit spatially homogeneous optical properties. Modifying the direction of propagation of light therefore requires to insert defects in the structure. There exists, however, an alternative to such an approach. In continuous media, light rays passing between two points in space follow the well-known Fermat's principle of least time, which states that light takes the path that requires the shortest time

to go from one point to the other. The optical path length, defined in terms of the medium refractive index, is then minimized. Now, supposing that the refractive index of the medium varies in space implies that the shortest optical path is curved. This fact is nicely pictured by a few naturally occuring phenomena, such as atmospheric mirages and ionospheric refraction, where the refractive index gradient results from gradients of the temperature and of the electron density with height, respectively [157]. In fact, this concept is also the underlying principle of transformation optics-based metamaterials, which we have described in Sec. 1.4. In the context of PhCs, inhomogeneity can provide an additional handle to manipulate light, making it possible to curve the path of light, and eventually combine different anomalous refraction effects. The progressive modification of the optical properties of an extended PhC can be realized by creating a gradient of refractive index, lattice periodicity or shape of the unit cell, hence their name *graded PhCs* [158]. Such structures can be integrated on conventional platforms such as SOI substrates in the same way as classical PhCs and thus could be used to enhance the functionality of all-optical components [159, 160]. Toward this objective, it is first necessary to acquire some understanding of the propagation of light beams in graded PhCs, which requires to study the effects resulting from the finite spatial extension of the beams and the anisotropy of the dispersion curves. This section is intended to explore some of the properties of 2D graded PhCs to control the propagation of light beams in space. We start by introducing the principles of graded PhCs.

3.1.1 Principles of graded photonic crystals

The idea of modifying the parameters of a PhC to progressively change its optical properties has previously been applied in PhC waveguide tapers to make a transition between the propagating modes of two different structures [161], or to localize light [162]. In such structures, the direction of propagation of light is settled by the linear defect constituting the waveguide, which is no longer the case in extended PhCs, where light follows the dispersion curves of the defectless structures. The refraction and path of light in a continuous inhomogeneous medium is described by the generalized Snell's law, $n(y)\,sin\theta(y) = n_i\,sin\theta_i$, where n is the refractive index of the inhomogeneous medium with a gradient along the y-direction, θ the angle formed by the tangent of the light ray at the depth y, n_i the refractive index of the homogeneous medium and θ_i the angle of incidence.

Graded PhCs relies on similar principles. Light propagates according to the *local* optical properties of the PhC layers. The dispersion properties of each PhC layer can be found by calculating the photonic band structure of the corresponding infinite PhC. Photonic band structures only make sense in periodic structures and a proper determination of the properties of a finite-size aperiodic structure would require to take into account the exact multiple scattering nature of the problem. The concept of local photonic band structure yet remains a very good approximation, provided that the variation of the structural parameters remains small.

The principles of light bending in graded PhCs is illustrated in Fig. 3.1. Light is incident from a continuous homogeneous medium on an arbitrary graded PhC. The spatial dispersion properties of the homogeneous medium and of the PhC layers at specific wavelengths are given by their corresponding iso-frequency curves (IFCs), shown on Fig. 3.1(a). The incidence of light at the interface between two structures imposes the conservation of the tangential component of the wavevector with respect to the coupling interface, k_x in our case, represented by a construction line of constant wavevector k_x. We assume that the PhC layers are isotropic to make the approach to the problem simpler. For the sake of consistency with the examples to follow, the photonic band of interest is negatively curved so that the group and phase velocities are in opposite directions. Since the energy transport velocity corresponds

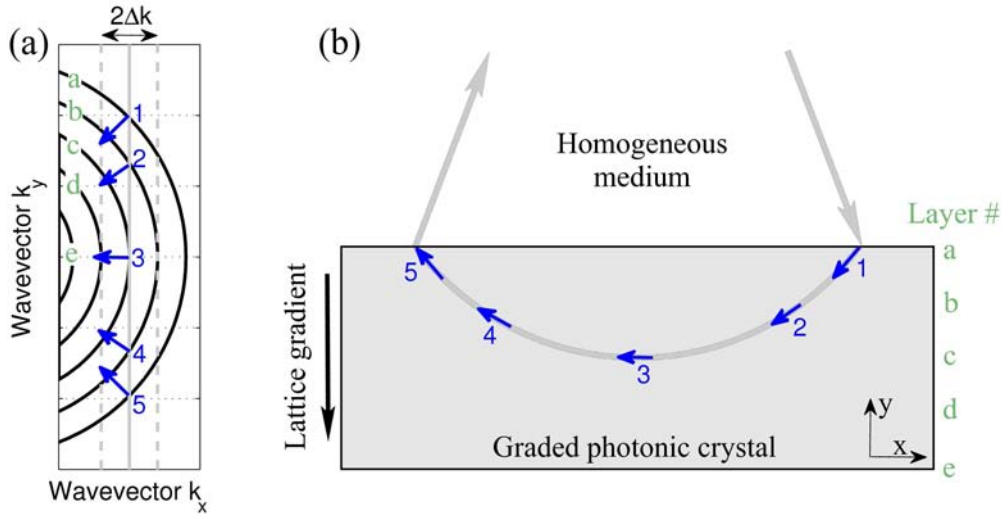

Figure 3.1: (a) IFCs (black curves) of the different PhC layers, indexed in green lower-case letters a-e, of an arbitrary graded PhC. The light gray solid line is the construction line, representing the conserved wavevector k_x, and the light gray dashed lines delimit the extension of the incident beam in reciprocal space. The various steps in the light bending process are denoted as blue numbers 1-5, and the corresponding group velocity directions as blue arrows. (b) Ray curve of the central wavevector component in the corresponding graded PhC.

to the group velocity, light is negatively refracted when it enters the graded PhC (step 1, layer a). It is smoothly bent as it penetrates the successive layers of the structure (step 2, layer b), down to the depth where its group velocity becomes parallel to the coupling interface (step 3, layer c). The PhC layers below this depth (layers d and e) have no intersection points with the construction line and thus prohibit the propagation of light. Light then naturally follows its course back to the coupling interface (steps 4 and 5, layers b and a) and finally exits in the homogeneous medium at the normal angle of reflection.

The light path described here is only valid for one specific wavelength and one specific wavevector, i.e. for a planewave incident at a specific angle. By this observation we mean that the optical effects obtained from one graded PhC would be different for other wavelengths and other angles of incidence. Considering the facts that PhCs usually exhibit a strong spectral and spatial dispersion and that the structural parameters of the graded PhCs can be molded in many different ways demonstrates the almost infinite number of possibilities that we have to manipulate light. Previous studies have used graded PhCs to realize frequency-selective tunable bends [158], or enhanced focusing and guiding devices [160]. Here, we do not look for the design of a specific device but concentrate on more elementary issues related to the propagation of light beams in strongly anisotropic structures.

3.1.2 Propagation of light beams

Light beams are composed by a finite set of wavevector components. The full-width at half-maximum (FWHM) $2\Delta x$ of a Gaussian beam in direct space is related to the FWHM $2\Delta k$ of the corresponding Gaussian beam in reciprocal space via the relation $\Delta x \Delta k = 1/2$. In the context of graded PhCs, the wavevector components of the incident beam projected on the axis parallel to the coupling interface (x-axis in our case) lie on a reciprocal area $2\Delta k$, delimited on Fig. 3.1(a) by two light gray dashed lines. This dispersion has two direct consequences. First, the exit points of the rays can be different, as it is naturally the case in atmospheric mirages. It is not necessarily detrimental to graded PhCs since this

angular sensitivity could be put to good use in frequency-selective devices. Assuming however that the wavevector dispersion Δk is small implies that the light path of the beam is relatively well preserved. Second, the group velocities of each wavevector component are parallel to the coupling interface in different PhC layers, i.e. at different depths in the graded PhC (in Fig. 3.1(a), the outer wavevector components reach the PhC layers b and d). This observation is particularly interesting, for it implies that the width of the beam in the graded PhC is not only inherent to the FWHM of the incident beam but also to the structural parameters of the graded PhC.

To give an account of these effects, we study the propagation of light in a 2D graded PhC, consisting of a rectangular array of air holes in a dielectric medium of refractive index 3.25, with lattice parameters along the x and y directions, denoted as d_x and d_y, respectively. The gradient is made by changing the lattice parameter d_y of the structure and is defined by the aspect ratio $\rho = d_y/d_x$. The radius of the holes is kept constant to $0.3d_x$. Figure 3.2(a) shows the IFCs of PhCs with aspect ratios ρ ranging from 0.90 to 1.18 in steps of 0.04 at the reduced frequency $a/\lambda = 0.27$ in the H-polarization, calculated with the planewave expansion (PWE) method. This structure can be tuned to the wavelength $\lambda = 1.55$ μm by setting the lattice periodicity $d_x = 418.5$ nm. The light beam is incident from a homogeneous medium of refractive index 3.25 on the graded PhC at an angle of 19.3 ° with respect to the y-axis, corresponding to a conserved wavevector $k_x = 0.29\,(2\pi/a)$, which lies outside the light cone of air and thus prevents out-of-plane losses to occur in finite-thickness planar structures. Due to the curvature of the first layer IFC, the beam is positively refracted and progressively turns back toward the negative x-direction. The group velocity finally becomes parallel to the coupling interface in the PhC layer of aspect ratio $\rho = 1.06$. In our simulations, the graded PhC is made of 40 columns of holes and the gradient linearly goes from $\rho = 0.90$ to 1.20, which places the region of horizontal propagation at the level of the central PhC layer.

Figures 3.2(b-d) show the modulii of the Poynting vector, computed with the 2D multiple scattering matrix method [117, 121], in different situations. In Figs. 3.2(b,c), the graded PhC is composed by 30 rows of holes with an increment in the aspect ratio $\Delta\rho = 0.01$ between successive layers, and the incident beam has a Gaussian distribution with a FWHM of 4 and 6 μm, respectively. As expected, we observe a decrease of the beam width in the graded PhC (i.e. along the y-axis) with the increase of the FWHM of the incident beam (along the x-axis). Larger incident beams indeed excite a smaller reciprocal area in the graded PhC and consequently, are localized in a fewer number of PhC layers. This effect is also obtained when the gradient strength is increased, as shown on Fig. 3.2(d). Here, the incident beam FWHM is 4 μm and the graded PhC is only made of 15 layers of holes, resulting in an increment in the aspect ratio $\Delta\rho = 0.02$ between successive layers. In this case, the incident light beam excites the same PhC modes but the horizontal propagation area now corresponds to a smaller number of layers, thereby reducing the PhC beam width. Before going any further, it is important to note that in all of the above structures, the maximal output intensity is found at the level of the central PhC layer, which thus agrees well with our IFCs study. The graded PhC have also been made shorter than required for a 180 ° bending. The output angle of the beam depends on the vertical component of the wavevector in the graded PhC. The fact that the output light beam is directed toward the positive y-direction means that the beam is still propagating downward in the graded PhC (i.e. between steps 2 and 3 in Fig. 3.1(a)).

The effect of beam shaping observed here is quite original and should absolutely be differentiated from conventional optical effects in extended PhCs. The lateral width of light beams in graded PhCs is no longer exclusively related to their characteristic localization width Δk in reciprocal space but also *to the structural parameters of the PhC in direct space*. The curvature of the beam now relies a different mechanism. In an isotropic inhomogeneous medium, the curvature of the light path increases

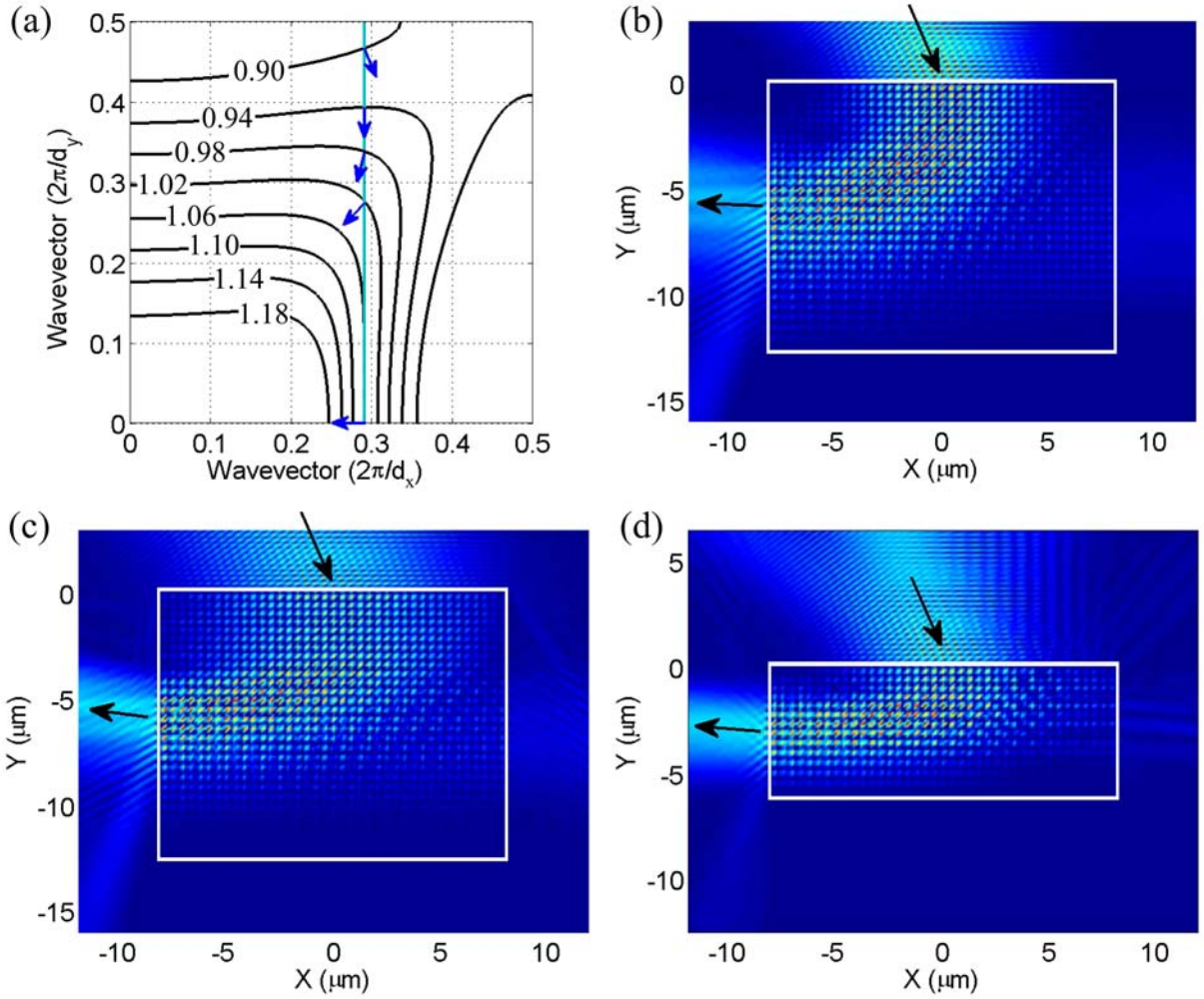

Figure 3.2: (a) IFCs of the graded PhC described in the text at the reduced frequency $a/\lambda = 0.27$. A Gaussian beam is incident on the structure at an angle of 19.3 ° with respect to the y-axis, represented by the construction line (gray solid line). The aspect ratio ρ of the PhC layers are indexed on their respective IFCs. The corresponding group velocity directions are indicated by blue arrows. (b-d) Modulus of the Poynting vector in different situations. In (b) and (c), the graded PhC is made of 40 columns by 30 rows of holes and the FWHM of the incident beam is 4 and 6 μm, respectively. In (d), the graded PhC is made of 40 columns by 15 rows of holes and the FWHM of the incident beam is 4 μm.

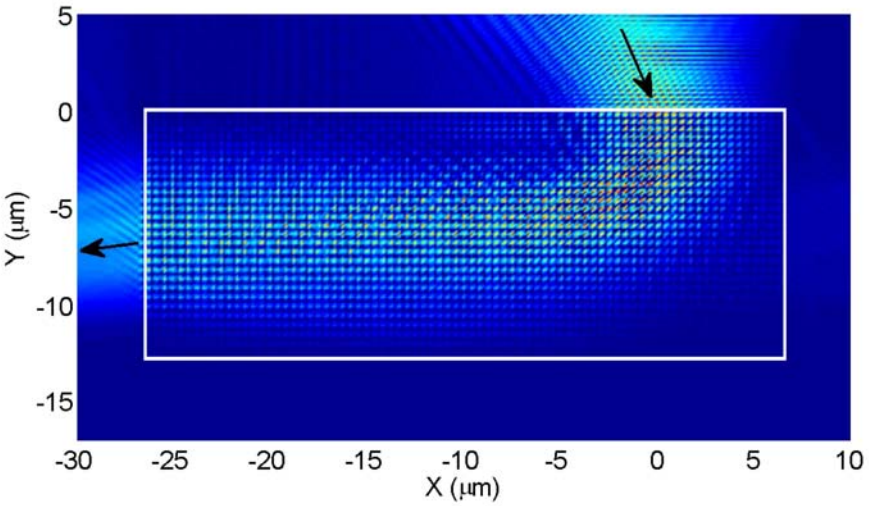

Figure 3.3: Modulus of the Poynting vector in a graded PhC, made of 80 columns by 30 rows of holes. The FWHM of the incident Gaussian beam is 4 μm.

with the rate of change of the refractive index. The strong anisotropy of graded PhCs therefore provides an additional tunable parameter to manipulate light beams. Straight IFCs, such as those used in the graded PhCs studied here, correspond to an extremely low rate of change of the group velocity. As soon as light penetrates a PhC layer with a quasi-horizontal group velocity, it starts requiring much longer distances to penetrate the lower PhC layers. Consequently, the light beam exhibits a very large radius of curvature and thus propagates almost linearly in the structure. The distance of propagation is naturally a function of the gradient strength and of the thickness of the structure. To illustrate this point, we consider the same graded PhC as previously studied, using 80 (instead of 40) columns by 30 rows of holes and an incident beam with a FWHM of 4 μm. As shown on Fig. 3.3, the beam propagates quasi-linearly in the graded PhC, as expected. The output beam is directed toward the negative y-direction, which means that the beam in the graded PhC has started its way up to the interface (between steps 3 and 4 in Fig. 3.1(a)).

At this point, we have introduced some of the effects related to the propagation of light beams in graded PhCs and have outlined their versatility, originating from their complex spatial dispersion properties. In view of the integration of graded PhCs on all-optical platforms such as SOI substrates, we have tuned the above structures to the near-infrared wavelengths. The dimensions and refractive indices used are typical of conventional silicon-based PhCs. Before designing graded PhCs for specific purposes, it is necessary to first demonstrate experimentally their capability of bending light on short distances.

3.1.3 The mirage effect: comparison with experiments

PhCs are inherently scalable to different frequencies. The concept of graded PhC in particular can be extended to structures of different materials and is expected to work also for all polarizations of light. For the sake of ease of fabrication and characterization, the graded PhC that is proposed here is tuned to the microwave range and composed of copper rods. The region of interest is the first dispersion curve of the structure in the E-polarization, which lies at relatively high frequencies, due to the existence of a cut-off [92]. Figure 3.4(a) shows the IFCs of metallic PhCs with copper rods of radius $0.075d_x$ calculated for different aspect ratios $\rho = 1.00$, 0.85 and 0.75 at the reduced frequency $a/\lambda = 0.426$, using the 2D

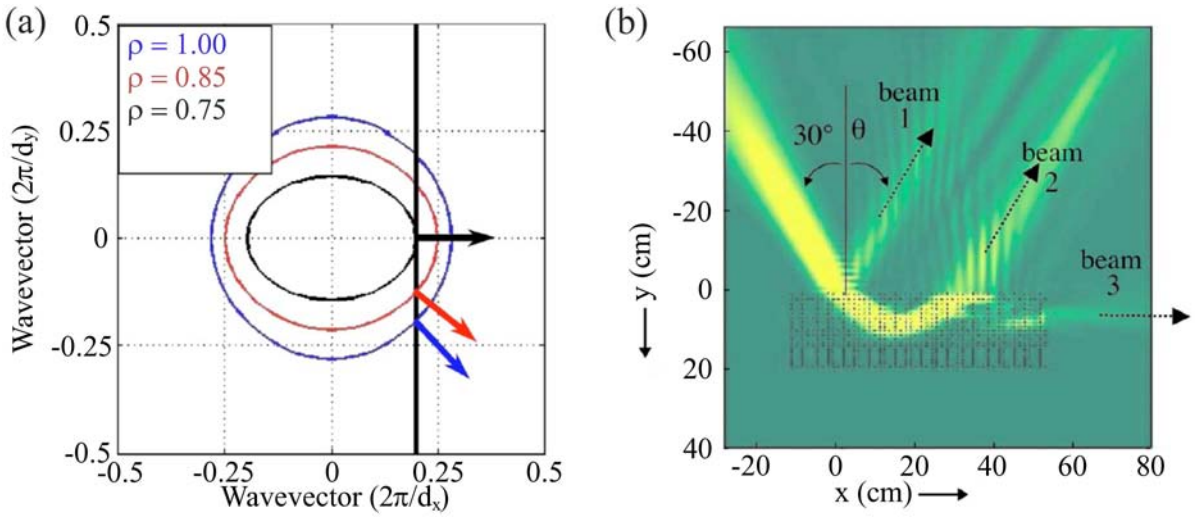

Figure 3.4: (a) IFCs calculated at 9.6 GHz for PhCs with aspect ratios ρ =1.00 (blue curve), 0.85 (red curve) and 0.75 (black curve). The construction line (black solid line) corresponding to a angle of incidence of 30 °. The group velocities directions are indicated by arrows. (b) Modulus of the Poynting vector in the metallic graded PhC at 9.6 GHz. The FWHM of the incident Gaussian beam is 10 cm. The dashed arrows indicate the reflected and transmitted beams. (Adapted from Ref. [163] with permission from E. Akmansoy).

finite-element method. The structure is scaled to a frequency of 9.6 GHz by using a lattice periodicity $d_x = 1.33$ cm. For an angle of incidence of 30 °, light is positively refracted in the structure and is bent continuously from about 45 ° ($\rho = 1.00$) to 90 ° ($\rho = 0.75$) with respect to the y-axis. This is verified in Fig. 3.4(b) by calculating the modulus of the Poynting vector in a graded PhC made of 49 columns by 20 rows of copper rods and an aspect ratio linearly going from $\rho = 1.00$ ($d_y = 1.33$ cm) to $\rho = 0.50$ ($d_y = 0.67$ cm). The incident E-polarized beam has a Gaussian distribution with a FWHM of 10 cm. As expected, the beam is bent within the structure and emerges from the upper interface (beam 2). Some part of the original beam is also reflected at the upper interface of the graded PhC (beam 1) and propagates in a secondary beam, that exits from the lateral interface (beam 3). We also note that the curvature of the beam within this graded PhC is much smaller than that observed in our previous designs (see Fig. 3.3). This effect is attributed to the quasi-isotropy of the IFCs, which makes the rate of change of the group velocity direction much larger in the vicinity of the PhC layer of horizontal group velocity.

The experimental part of this work has been made by E. Akmansoy and J.-M. Lourtioz at the Institut d'Electronique Fondamentale in Orsay, France. Figure 3.5(a) shows a picture of the fabricated graded PhC, composed of copper rods with radius 1 mm and height 20 cm. Its characterization has been carried out using a microwave goniometer, which consists of two horns connected to an 8722ES Agilent network analyzer (Fig. 3.5(b)). The emitting horn illuminates the device at a distance of 50 cm and an angle of 30 °. The receiving horn is placed at a distance of 90 cm from the device and can be rotated up to an angle of 180 °.

Figure 3.6(a) shows the scattering patterns of the metallic graded PhC obtained from the measurements and from the simulations. The two signals are in good agreement, especially considering that the finite thickness of the graded PhC has not been taken into account in the simulations. The strongly modulated signal observed at angles close to 30 ° corresponds to the interfering reflected and curved beams (beams 1 and 2 respectively), while the signal at angles close to 100 ° corresponds to the beam that exits from the lateral interface (beam 3). In order to map the trajectory of the beam within the

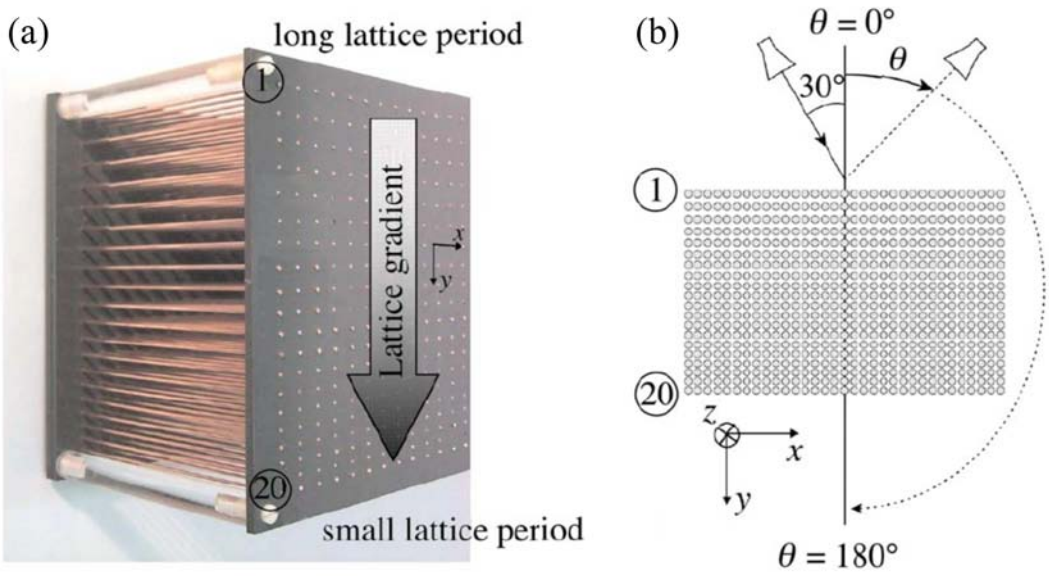

Figure 3.5: (a) Picture of the fabricated graded PhC, which consists of an array of copper rods. (b) Top view of the measurement setup. The emitting microwave horn is orientated at an oblique incidence of 30 ° and the receiving horn can be rotated around the graded PhC at angles from 0 ° to 180 °. (Adapted from Ref. [163] with permission from E. Akmansoy).

graded PhC, a microwave absorbing sheet with a 30 dB attenuation and weak residual reflection has been gradually inserted along the y-direction of the graded PhC from its lower interface up to the position where the scattering pattern was modified, denoting an interaction between the absorbing sheet and the beam. The measured positions of the lower edge of the beam within the graded PhC shown on Fig. 3.6(b) are in excellent agreement with the simulation, confirming the curved trajectory of the light beam in the structure. Additional experiments reported in Ref. [163] have led to a similar conclusion.

The experimental demonstration of this mirage effect validates the concept of graded PhC and the capability of such structures to mold the path of light. This allows us to envisage the realization of integrated graded PhCs operating in the near-infrared range that may be an integral part of future all-optical technologies. Taking some hindsight onto this concept of inhomogeneous PhC, light rays corresponding to different wavevector components follow different paths in the structure. In the cases shown above, this causes the beam to slightly spread as it propagates. Without doubt, this issue may be solved by appropriate designs. Of course, such an approach would be quite tedious, for it would rely on a try-and-see basis. In this regard, it would be interesting to make the connection between graded PhCs and geodesics, which introduce the concept of curved spaces naturally arising from the Fermat's principle of least time and with the principles of transformation optics. Although this may prove to be a difficult task due to the complexity of the dispersion properties of PhCs, it could be worth the effort, for the graded PhC would be conceptually replaced by a virtual curved electromagnetic space [164], making it possible to define all possible ray curves in the structure. In a way, graded PhCs would stand on the same level as metamaterials, which, as briefly discussed in Chapter 1, have inspired a great number of fascinating technologies, including electromagnetic cloaks [94].

Before reaching this point however, a couple of issues will need to be addressed. First, some scattering losses can occur within the graded PhC because of its discrete character (graded PhCs are not continuous media) and of the phase mismatch between consecutive PhC layers. A theoretical study on the adiabatic

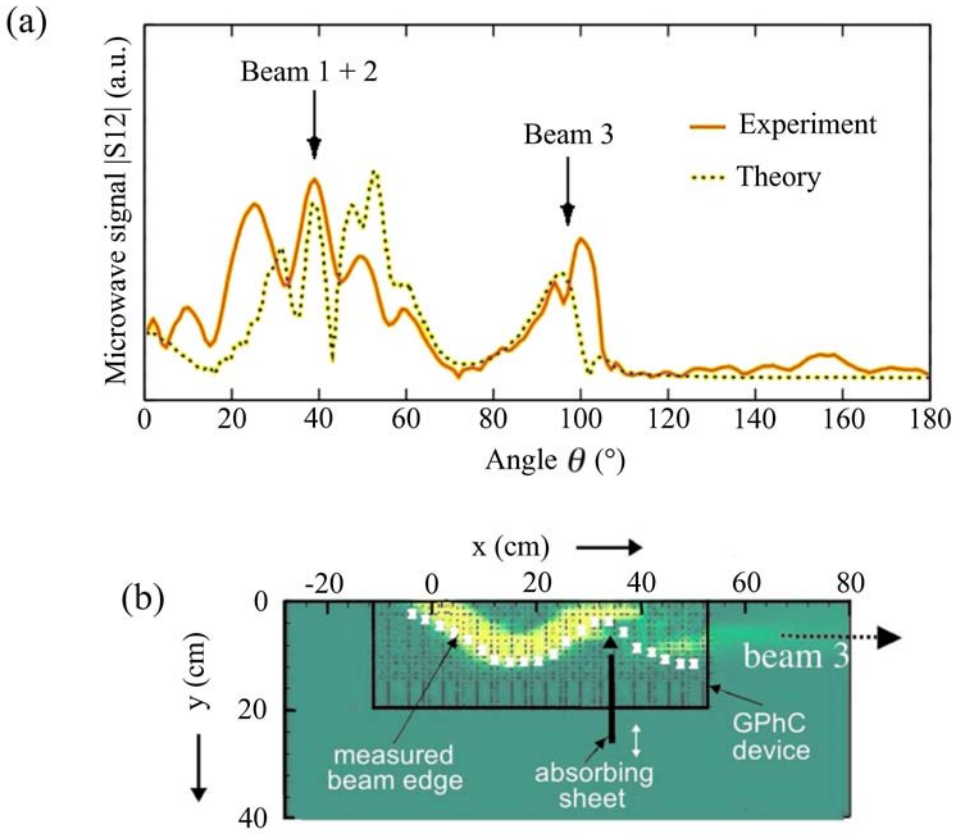

Figure 3.6: (a) Measured and calculated scattering patterns of the graded PhC at 9.6 GHz. (b) Vertical position of the lower edge of the beam in the graded PhC, measured with the absorbing sheet technique (see the text). Measurements data (white dots) are superimposed onto the numerical simulations. The size of the dots accounts for the measurement uncertainties (±3 mm). (Adapted from Ref. [163] with permission from E. Akmansoy).

process in graded PhCs, in a similar way as for slow-light tapers [165], would probably help to define certain practical conditions on the design of the gradient, particularly on a minimal rate of change. Second, the scattering losses that occur at the interfaces of the graded PhC can be relatively strong, depending on the wavelength of light and on the shape and angle of incidence of the beam. In view of integrating extended PhCs on all-optical platforms, we need to study the coupling of light from external waveguides. A first step to approach the problem is to restrict our study to one particular type of extended PhCs. The next section is intended to find an efficient and experimentally feasible solution to the coupling of light from conventional waveguides to supercollimating PhCs on SOI platforms.

3.2 Light coupling to supercollimating photonic crystals

Supercollimation, as discussed in Sec. 1.3, gives the possibility to propagate light in straight lines over large distances without using structural waveguides [76]. Recent studies report the possibility to realize devices such as optical routers, multiplexers or polarization splitters, by incorporating linear defects in periodic structures [79, 166]. In the general context of extended PhCs, supercollimating PhCs appear by themselves as a possible building block for many interesting applications and it seems very likely that they will play a key role in Photonics in the years to come. The integration of PhCs implies that they should be efficiently coupled to integrated single-mode waveguides. The integrated aspect of the external waveguides is important if all photonic components are to be fabricated on a single chip, while the single-mode condition is required to ensure proper light signal transmission between each component. The coupling of light to supercollimating PhCs however remains a real technological challenge. As we will see below, the incident beam has to excite very specific Bloch modes in the PhC [167,168], imposing some requirements on the design of the excitation waveguide, while the impedance mismatch that occurs at the interfaces between different components is responsible for back-reflections that may be inconvenient in practical applications. In this sense, the different structures and their interfaces have to be appropriately designed to overcome the mode-profile mismatch and the impedance mismatch between the propagating modes. The coupling techniques [76, 169–172] that have been employed up to now do not meet all conditions (single-mode propagation, efficient coupling and practical feasibility) simultaneously. More generally, we are not aware of any extensive work on the coupling of light from integrated waveguides to supercollimating PhCs, and although it has been shown that PhC boundaries were of crucial importance for improving the coupling of light to extended PhCs [173–175], such an approach has not been applied to supercollimating PhCs in particular. In the following, we proceed in different steps, first focusing on the matching of the profile of the waveguide mode and of supercollimated beam, and then on the improvement of the impedance matching at the interface between the two photonic components.

3.2.1 Mode matching

An efficient coupling of light to extended PhCs requires the incident beam to excite very specific Bloch modes in the PhC. This is the concept that we have used in the study of graded PhCs, where the beam is composed by a set of wavevectors which excite different modes in the structure. Here, the modal coupling efficiency between the two photonic components depends on the overlap of their mode profiles [176]. In the present case, the dispersion properties of the supercollimating PhC imposes some conditions on the incident beam that in turn yield certain requirements on the design of the excitation waveguide. The determination of the dispersion properties of the supercollimating PhC is therefore the starting point of our study.

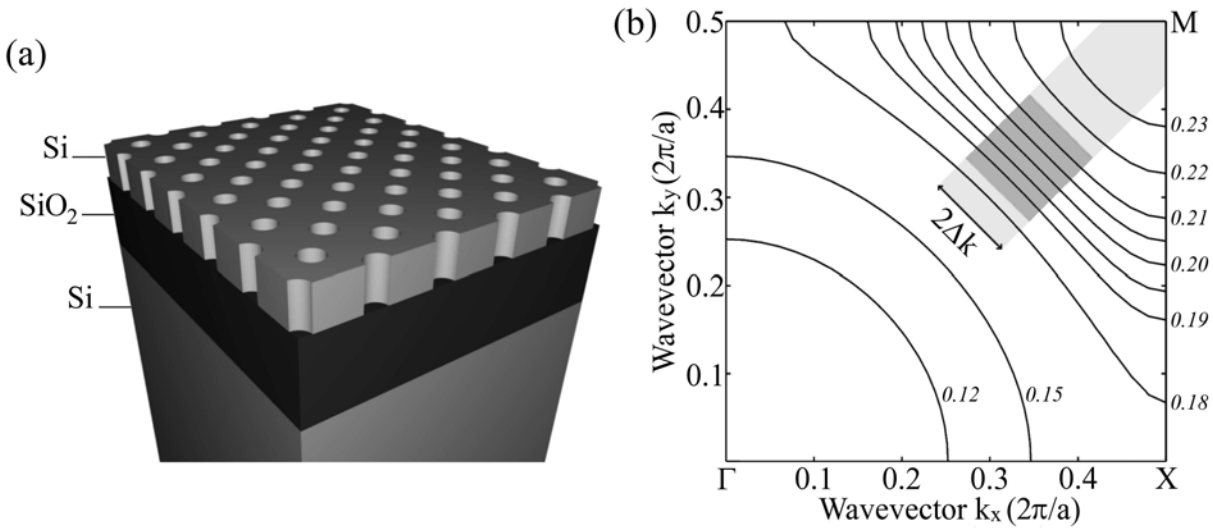

Figure 3.7: (a) 3D view of the SOI-based supercollimating PhC, consisting of a patterned Si layer, deposited on a SiO_2 layer that lies on a thick Si substrate. (b) IFCs of a PhC consisting of a square lattice of holes with radius r=94 nm and a lattice period a=310 nm, calculated in 3D with the FDTD method. The reduced frequencies are indexed on their respective IFC in units of a/λ. The dark gray-shaded area corresponds to the reciprocal full-width ($2\Delta k$) on which the IFCs exhibit a near-zero curvature.

Supercollimating photonic crystals

Due to the wide use of silicon (Si) in present electronic devices, the pre-eminent solution for integrating photonics to future technologies is to use SOI platforms. The high index contrast between Si and the substrate (typically silica (SiO_2)) makes it possible to design efficient planar PhCs and low-loss waveguides. On an experimental point of view, both components (waveguide and PhC) can be fabricated on a single SOI wafer, which therefore makes the whole device easy to integrate on current photonic platforms.

The supercollimating PhC under consideration consists of a 2D square arrangement of air holes in a Si layer of refractive index 3.5 and thickness t=340 nm, deposited on a SiO_2 layer of refractive index 1.45 and thickness 700 nm that lies on a thick Si substrate. A 3D view of this structure is given on Fig. 3.7(a). A thickness of 700 nm is sufficient for the SiO_2 layer below the guiding Si layer to prevent light from leaking down to the Si substrate [177]. The period a of the lattice is 310 nm and the radius r of the holes is 94 nm. These parameters have been chosen to collimate light at wavelengths λ close to 1.55 μm and ensure its vertical confinement to the PhC slab by index guiding. The dispersion properties of PhCs are obtained from the PhC IFCs in reciprocal space, where the group velocity of a propagating mode is defined by $\mathbf{v}_g = \nabla_k \omega(\mathbf{k})$ and its direction by the normal to the IFC. The PhC dispersion curves have been computed with the 3D finite-difference time-domain (FDTD) method.

Figure 3.7(b) sketches the IFCs corresponding to the first H-like mode of the PhC. Straight IFCs, which are composed by modes with nearly similar group velocity directions, appear along the ΓM direction for reduced frequencies a/λ between 0.19 and 0.21. The near-zero IFC curvature observed in this region lies on a reciprocal half-width $\Delta k = 0.05\ (2\pi/a)$, which corresponds to the characteristic localization width of the supercollimated beam in reciprocal space. The lateral extension Δx of the beam in direct space can then be retrieved from the well-known uncertainty relation $\Delta x \Delta k \geq 1/2$. In our case, we find $\Delta x \geq 1.6a = 0.50$ μm, which implies that the lateral width of the incident beam in the excitation waveguide should be greater than or equal to 1.0 μm to prevent some of the incident modes to

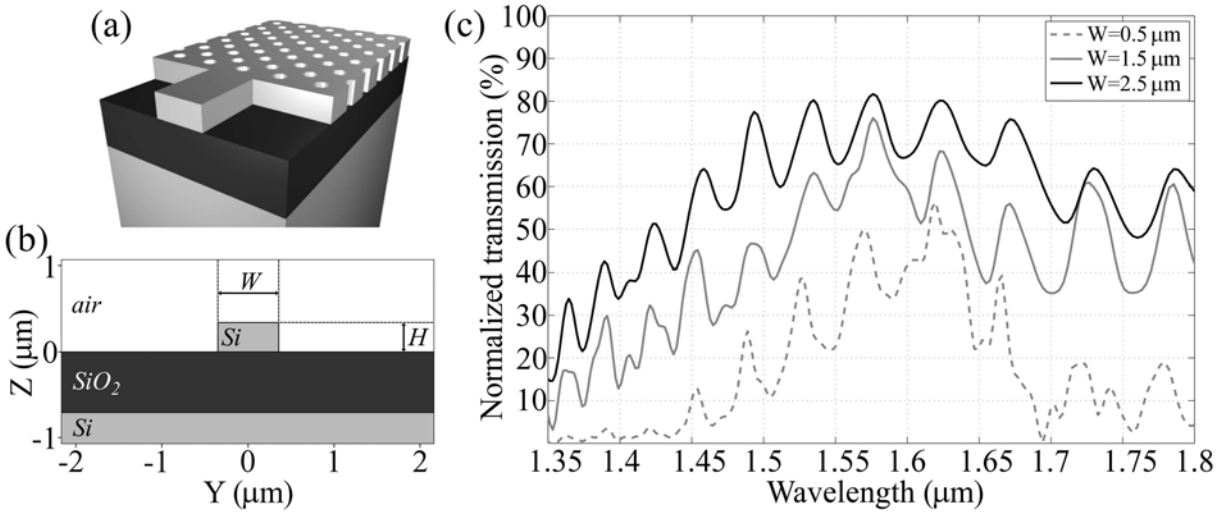

Figure 3.8: (a) 3D view of the strip waveguide-PhC interface on a SOI platform. (b) Cross-sectional view of a SOI-based strip waveguide with height H and width W. (c) Transmission spectra of the supercollimating structure using strip waveguides of height H=340 nm and respective width W=0.5 μm (gray dashed line), 1.5 μm (gray solid line) and 2.5 μm (black solid line), calculated in 3D with the FDTD method.

lie outside the IFC straight area and thus to be dispersed in the PhC. This minimal value corresponds to a Gaussian beam with a FWHM of $2\Delta x = 1/\Delta k$. In the next step of our analysis, we will therefore aim at designing a SOI-based waveguide sustaining a single-mode that fulfills the minimal width condition and deviates as less as possible from a Gaussian distribution.

Coupling to strip waveguides

Strip waveguides consist of a waveguide core surrounded by a fully etched Si layer (see Figs. 3.8(a,b)). Due to their ease of fabrication, SOI-based strip waveguides have been intensively studied and used in particular to couple light into PhC waveguides [178]. Here, we consider a strip waveguide of height H, determined by the thickness of the guiding Si layer (t=340 nm), and width W. In the present case, it is worth noting that regardless of their width, waveguides of this thickness are multimode and therefore are not adapted to data-transmission systems. Nevertheless, strip waveguides can be fabricated with existing techniques and with an excellent quality, which makes them potentially useable at least for characterization experiments. It is therefore important to study how efficient the coupling of light from strip waveguides to supercollimating PhCs could be.

The coupling efficiency of the supercollimating structure at the waveguide-PhC interface is obtained by calculating the transmission of light between two waveguides (input and output) placed on each side of an 8 μm-long supercollimating PhC directed along the ΓM direction of the PhC square lattice. The boundary of the supercollimating PhC is placed half-a-period away from the first column of holes.[1] Simulations have been performed in 3D with the FDTD method. Figure 3.8(c) sketches the transmission spectra of these structures using strip waveguides of different widths W=0.5, 1.5 and 2.5 μm. The strong Fabry-Pérot (FP) oscillations, resulting from important back-reflections at both waveguide-PhC interfaces, indicate a large impedance mismatch between the two structures. This point will be considered below. Now, according to the minimal lateral width condition, the larger waveguides sustain modes that

[1]This position will further refer to the termination $\tau = 0$.

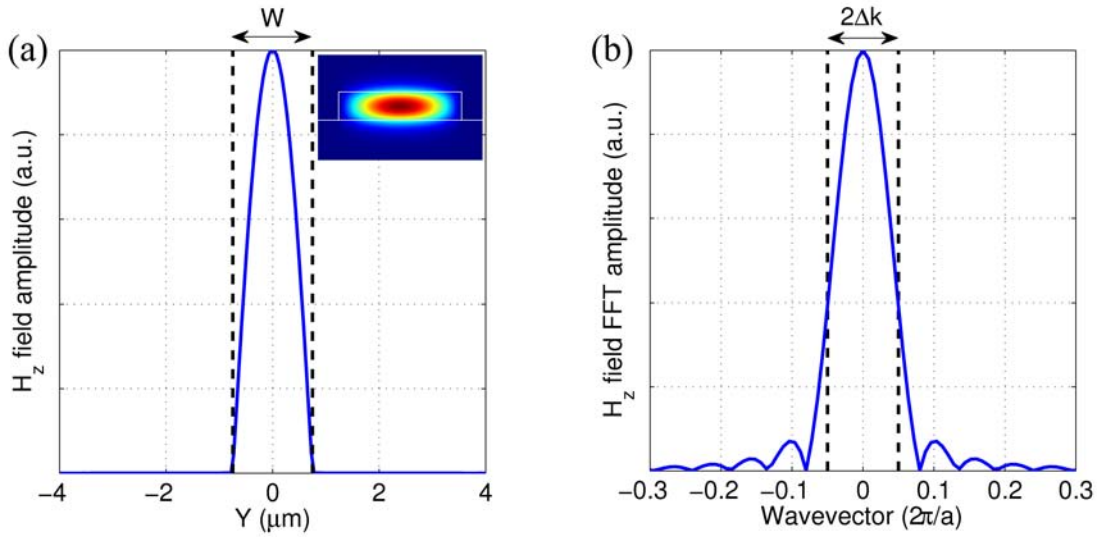

Figure 3.9: (a) Amplitude of the magnetic field H_z of the fundamental mode of a strip waveguide of width $W = 1.5$ μm. The profile is taken in the middle of the guiding Si layer. The black dashed lines delimit the lateral boundaries of the waveguide. The inset shows the mode in a vertical cross-sectional view of the strip waveguide. (b) Fourier transform of the mode profile. The black-dashed lines delimit the reciprocal area where the IFC is straight.

excite, for a larger part, the Bloch modes lying on the IFC straight area, thereby limiting the light dispersion within the PhC. As expected, we observe an improvement of the overall transmission with the widening of the excitation waveguide. The larger waveguides however still yield some serious losses and the transmission hardly reaches 80 %. There are mainly two reasons for this discrepency : first, the waveguide is multimode and therefore propagates higher-order modes with different mode profiles and symmetries that do not necessarily meet the minimal width condition. Second, the fundamental mode of the waveguide is not smooth enough in the lateral direction to avoid the excitation of Bloch modes outside the reciprocal area where the IFC is straight. This is shown in Fig. 3.9, where we sketch the lateral profile of the fundamental mode of the strip waveguide of width $W = 1.5$ μm, taken in the middle of the guiding Si layer, and the corresponding Fourier transform of the mode profile in reciprocal space. The abrupt lateral interfaces of the waveguide are indeed responsible for the excitation of higher-order terms, which contain a non-negligible part of the incident beam energy, outside the supercollimation reciprocal area. An efficient coupling of light to supercollimating PhCs requires the use of waveguides capable of sustaining large and smooth single-modes.

Coupling to rib waveguides

Rib waveguides consist of a waveguide core surrounded by a partially etched Si layer, contrary to strip waveguides, where the surrounding Si layer if etched down to the SiO_2 layer. Rib waveguides have the capability of sustaining E and H-like single-modes that exhibit a larger spatial extension than other SOI-based waveguides [179]. As explained above, these spatially extended propagating modes may be the key for a selective and efficient coupling of light to the PhC supercollimated modes. As a proof of concept, we consider a rib waveguide with a total height $H = 340$ nm (fixed by the planar PhC thickness t), an etch depth $d = 40$ nm and a width $W = 700$ nm (see Fig. 3.10(a)). Figure 3.10(b) shows the corresponding H-like single-mode propagating at a wavelength of 1.55 μm ($a/\lambda = 0.200$ in the PhC), as calculated with the finite-element method. The FWHM of the mode at the depth where it spreads

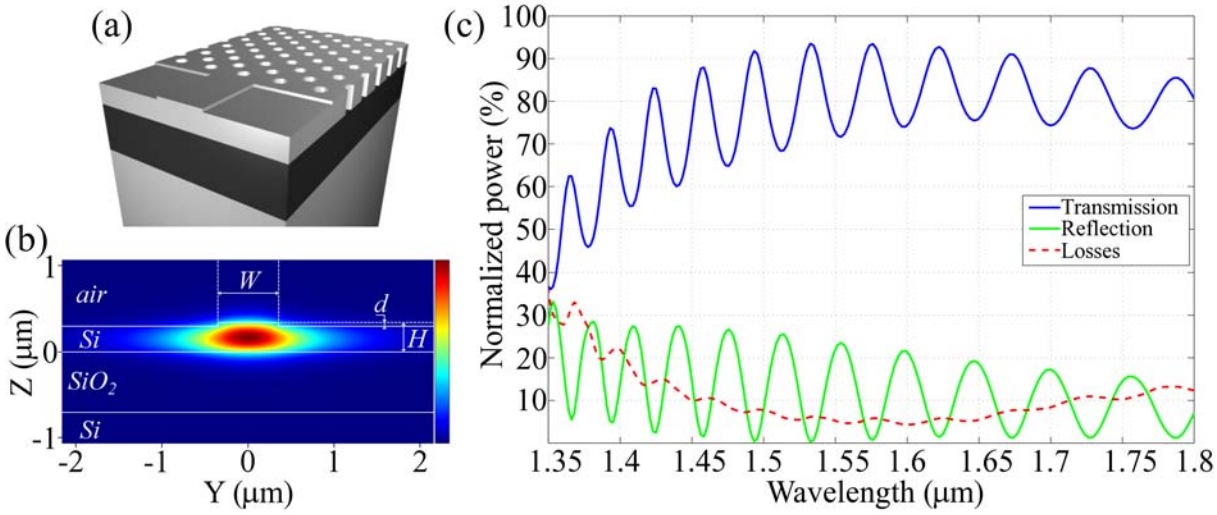

Figure 3.10: (a) 3D view of the rib waveguide-PhC interface on a SOI platform. (b) Amplitude of the magnetic field H_z at a wavelength of 1.55 μm in a cross-sectional view of the rib waveguide, calculated with the finite-element method. The Si waveguide of height H=340 nm, etch depth d=40 nm and width W=700 nm is deposited on a SiO_2 layer that lies on a thick Si substrate. (c) Transmission (blue solid line), reflection (green solid line) and losses (red dashed line) spectra of the supercollimating structure, calculated with the FDTD method in 3D.

the most is about 1.2 μm, which is slightly larger than the minimal lateral width of the supercollimated beam considered here (1.0 μm). We also note that the mode smoothly spreads within the guiding Si layer.

We calculate the transmission of light through a supercollimating device, consisting of two rib waveguides placed on each side of the supercollimating PhC. The spectra shown on Fig. 3.10(c) exhibit transmission efficiencies up to about 94 % and reflections down to almost 0 % at wavelengths close to 1.55 μm (a/λ= 0.200). The losses, which quantify the amount of light that is dispersed at the waveguide-PhC interfaces and within the PhC, go down to about 6 %, which infers an excellent mode-profile matching between the rib waveguide and the supercollimating PhC. At wavelengths where the IFC curvature is larger, light is more dispersed within the PhC, yielding an increase of the losses. Figure 3.11 sketches the lateral profile of the rib waveguide single-mode, taken in the middle of the guiding Si layer, and the corresponding Fourier transform of the mode profile in reciprocal space. Owing to the very smooth and largely extended lateral profile of the mode in direct space, the amplitude of the mode in reciprocal space rapidly decreases down to very low values, while exhibiting no higher-order bumps. A very large part of the incident energy therefore belongs to the reciprocal area where the corresponding IFC is straight, inferring a proper excitation of the supercollimated beam.

At this point, we have shown that rib waveguides ensure an excellent mode-profile matching between their fundamental mode and the supercollimated beam in the PhC. The second point to consider in the improvement of the impedance mismatch between the rib waveguide and the supercollimating PhC, causing the large FP oscillations observed in Fig. 3.10(c). They remain particularly strong with an amplitude ranging between 10 and 20 % over the whole range of study. Such oscillations yield detrimental resonances that hide the main features of the structure and could be very troublesome if supercollimating PhCs were to be used in all-optical technologies.

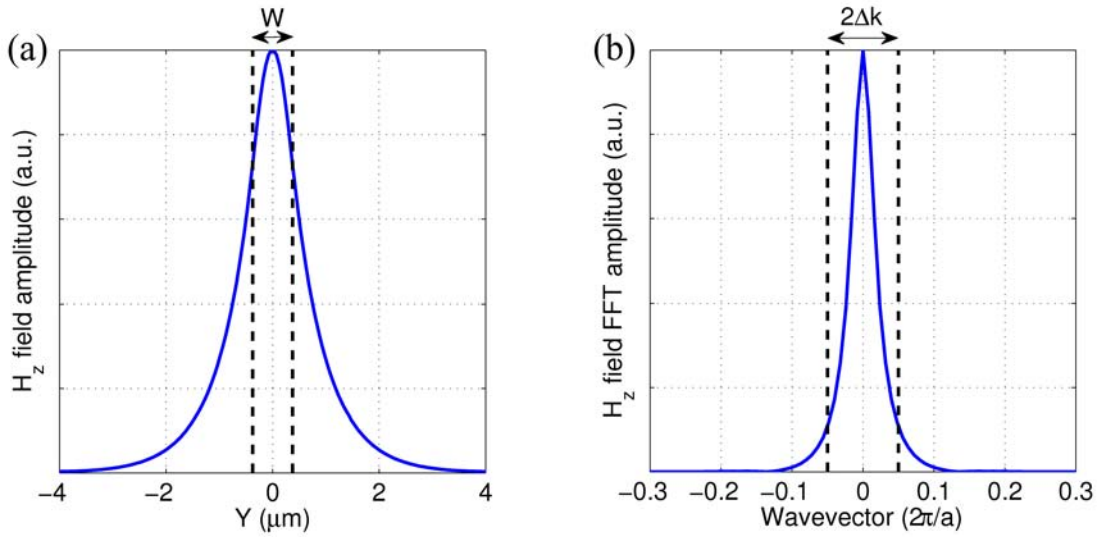

Figure 3.11: (a) Amplitude of the magnetic field H_z of the fundamental mode of the rib waveguide described in the text. The profile is taken in the middle of the guiding Si layer. The black dashed lines delimit the lateral boundaries of the waveguide of width $W = 700$ nm. (b) Fourier transform of the mode profile. The black-dashed lines delimit the reciprocal area where the IFC is straight.

3.2.2 Impedance matching

At an interface between two homogeneous media, the amplitude of reflected and refracted planewaves is given by the Fresnel formulae [180]. These relations describe the coupling efficiency of the planewave from one medium to the other. The reflection and transmission coefficients can be written as a function of the *transverse impedance*, defined as the ratio of the transverse electric field to the transverse magnetic field with respect to the direction of propagation.[2] The impedance in a PhC is spatially-dependent, since the structure is a inhomogeneous medium. It has been shown that an equivalent impedance could still be defined by averaging the fields over a period of the PhC, provided that the incident and transmitted regions would support a dominant mode [181,182]. This means that by changing the interface of the PhC, we actually can modify the impedance of the PhC and thus, improve (resp. diminish) the impedance matching between the two media in a way to increase (resp. decrease) the coupling efficiency [183].

Here, we propose to minimize the reflectivity of the interfaces between the rib waveguides and the supercollimating PhC simply by truncating the PhC at its boundary. Let τ be the termination parameter, defined as the distance between the original boundary of the PhC and the position where the PhC is effectively truncated. By commodity with the calculations above, the boundary corresponding to the termination parameter $\tau = 0$ lies half-a-period away, i.e. at a distance $a/\sqrt{2}$, from the first row of holes (see Fig. 3.12(a)). We realize a series of 3D calculations, partly shown on Fig. 3.12(b), on the transmission between two rib waveguides placed on each side of different supercollimating PhCs with termination parameters τ=$0.8a\sqrt{2}$, $0.9a\sqrt{2}$ and $1.0a\sqrt{2}$. We find that the amplitude of the FP oscillations is minimized when the supercollimating PhC is truncated in the middle of a column of holes, corresponding to the termination parameter $\tau = na/\sqrt{2}$, where n is a strictly positive integer. This dramatic change of the FP oscillations amplitude emphasizes the particular importance of the PhC termination on the coupling efficiency.

Figure 3.13(a) shows the transmission, reflection and losses spectra of the optimized supercollimating

[2] In the case of H-polarized light incident on an interface parallel to the y-axis, the transverse impedance is of the form $\eta_y = E_y/H_z$.

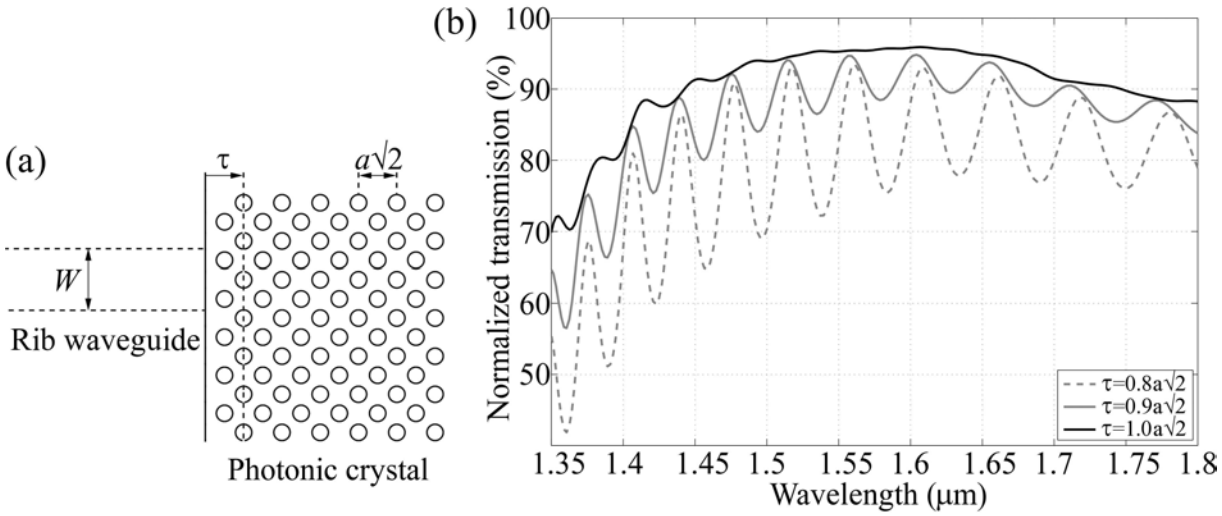

Figure 3.12: (a) Top view of the rib waveguide-PhC interface of the supercollimating structure. The rib waveguide has a width W and is coupled to the supercollimating PhC, which is truncated at a distance τ from the original PhC boundary. (b) Transmission spectra of the supercollimating structure with rib waveguides for different PhC terminations τ=$0.8a\sqrt{2}$ (gray dashed line), $0.9a\sqrt{2}$ (gray solid line) and $1.0a\sqrt{2}$ (black solid line), calculated in 3D with the FDTD method.

device with the rib waveguides considered above. It exhibits transmission efficiencies up to about 96 % and quasi-null reflections (below 0.2 %) at wavelengths close to 1.55 μm (a/λ= 0.200). The losses are very similar to those found for the non-optimized structure, which is normal since they are primarily related to the quality of the mode-profile matching between the waveguide mode and the supercollimated beam. On the other hand, the FP oscillations have been significantly reduced, which demonstrates the excellent impedance matching obtained at the waveguide-PhC interfaces from the truncation of the PhC. The reflections remain particularly low over the whole wavelength range of study, which shows that the coupling efficiency at the waveguide-PhC interface is excellent on a rather broad wavelength range. The use of longer supercollimating PhCs would reduce the operating bandwidth of the structure but not the maximal transmission efficiency. The steady-state amplitude of the magnetic field H_z at a wavelength of 1.55 μm shown on Fig. 3.13(b) confirms the low reflections and dispersion experienced at the waveguide-PhC interfaces and within the PhC. We believe that these results are truly valuable, especially considering that all calculations have been made in 3D to take into account the out-of-plane losses experienced by the whole device.

The results obtained here in the particular case of supercollimating PhCs can be generalized to extended PhCs. As a matter of fact, dispersion-based effects generally require the excitation of specific Bloch modes and here again, SOI-based rib waveguides, which support large and smooth single-modes, are suitable. This is particularly true for graded and ultra-refractive PhCs. Most of the studies on negative refraction PhCs have focused on lensing effects, in which case no excitation waveguide is needed. The impedance mismatch problem is necessarily present at all interfaces between different structures and it can be improved by structuring the interface. It is also worth noting that a single truncation may not be adapted to all incident wavevectors. Here again, the use of large incident single-modes is a benefit since they exhibit a smaller dispersion in reciprocal space.

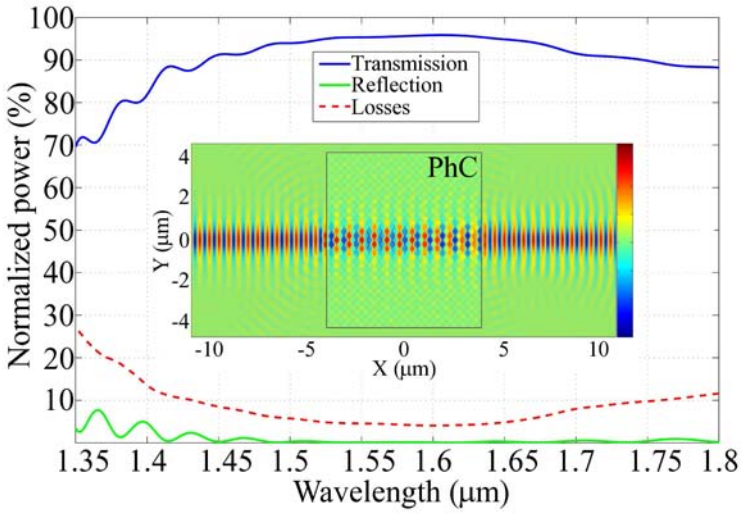

Figure 3.13: Transmission (blue solid line), reflection (green solid line) and losses (red dashed line) spectra of the supercollimating structure with rib waveguides, calculated with the FDTD method in 3D. The inset shows the steady-state amplitude of the magnetic field H_z at a wavelength of 1.55 μm in a top view of a cut in the middle of the device.

Summary

This chapter has been devoted to the enhancement of the features of extended PhCs in order to have a more flexible and efficient control over light propagation in space. We have shown that graded PhCs have the great ability to bend light beams on the wavelength scale. We have provided a deeper understanding on the curvature and shaping of the beam by relating these effects to the anisotropy of IFCs and strength of the gradient. The richness of the PhCs dispersion properties provides a wealth of possibilities to control light propagation. In a second part, we have addressed the problem of light coupling from integrated waveguides to supercollimating PhCs by successively showing that rib waveguides can provide an excellent mode-profile matching between the two structures, and that a truncation of the PhC boundary can significantly improve impedance matching. Transmission efficiencies as high as 96 % and reflections lower than 0.2 % have been obtained in this way at wavelengths close to 1.55 μm. This approach may be applied to extended PhCs in general. The structures presented here can be fabricated on conventional SOI platforms and operate in the near-infrared range.

Chapter 4

An all-dielectric route to metamaterials

Together with photonic crystals (PhCs), metamaterials (MMs) contribute to the ultimate goal of a full control of light. Perfect lensing and electromagnetic cloaking are some of the tremendous effects that have motivated their study. Great efforts are now being made to scale MMs down to the optical frequencies [96,97]. Such an accomplishment would indeed make possible the development of versatile and highly efficient technologies in various areas, including the telecommunications, medical imaging and solar energy. Recent works [101, 103–105, 184–187] made a step toward this objective using high-permittivity dielectric objects instead of metallic ones to avoid the losses and saturation effects inherent to the metal in the optical regime [188]. Interestingly, it has been suggested recently that high-permittivity rods in E-polarized light could exhibit both electric and magnetic resonances, possibly leading simultaneously to a negative permittivity and a negative permeability [104, 105]. Such an achievement could have a strong impact on the scientific community, for it would allow to design integrated lossless MMs, e.g. double-negative structures, with only one type of simple-shaped element (a dielectric rod) instead of the more complex metallic structures (e.g. a mix of split-ring resonators and thin wires). To our knowledge however, no rigorous study on the electric and magnetic activities of dielectric rods has been given in the context of MMs, preventing any deep understanding of the optical properties of rod-type structures and thus, ruling out the possibility of using them in future technologies, especially at the optical frequencies.

This chapter is intended to gain more insight onto the optical properties of all-dielectric rod-type structures. We will follow a bottom-up approach by giving a microscopic description of the behavior of the individual rods to capture the electrodynamics of arrays of rods on the macroscopic scale. In Sec. 4.1, we will show that the dielectric rods can be conceptually replaced by radiating electric and magnetic dipoles whose explicit expressions will be derived in terms of the scattering matrix. In Sec. 4.2, we will use these new microscopic expressions and a homogenization model to compute the effective dispersion curves of a macroscopic square array of rods. Based on these results, we will be able to explain the origin of photonic band gaps (PBGs) and left-handed bands in their dispersion properties. We will pay particular attention to the scaling of these effects and the spatial dispersion of these structures. In a last part, we will discuss some possible issues related to structural disorder and will report the observation of 2D microscopic optical necklace states.

4.1 Electric and magnetic dipole activities of dielectric rods

It has been known for a long time that dielectric objects under illumination can resonate in different modes [100]. Dielectric cylinder resonators have been of great interest from the 1960's, because they provide a way to create compact microwave bandpass filters, transmission antennas and many other technologies [189]. It is well-known that, for instance, the first Mie resonances of dielectric rods in E and H-polarizations give rise to electric and magnetic dipoles, respectively. Following the introduction of MMs, where the most challenging issue was to design resonators with a magnetic dipole activity in the optical frequencies, O'Brien and Pendry suggested that the dielectric rods in H-polarized light could be used to create a resonance of the effective medium permeability [101]. This artificial magnetism has been explained on a rigorous theoretical basis some years later by Felbacq and Bouchitté [102] and has been used recently to design invisibility cloaks in the microwave regime [190, 191]. The recent papers by Peng *et al.* and Schuller *et al.* have now carried this idea a little further by proposing to use the higher-order resonances of dielectric rods to create resonances of both the permittivity and permeability of the effective medium [104,105]. It is interesting to note also that it has been suggested previously that the magnetic dipole term of resonant objects provide the first dynamic correction to the static effective refractive index of arrays of them [192].

In classical electromagnetism, an arbitrary distribution of oscillating currents can be expanded in a multipole series, introducing the electric and magnetic dipoles, quadrupoles and so on. In order to use dielectric rods as a constituent of MMs, it is necessary to consider them on the microscopic scale as multipole resonators. In other words, the rods should be described in terms of their electric and magnetic polarizabilities to depict their capability of producing electric and magnetic dipole moments under external electromagnetic excitation. Although previous expressions of the electric polarizability of dielectric rods in E-polarized fields have been given [193], the existence of a magnetic polarizability is a novel concept that requires a deeper investigation. The scattering of light by circular cylinders can be rigorously described by Mie theory, thereby constituting an excellent starting point to approach the problem.

4.1.1 Scattering of light by circular dielectric rods

Let us consider a dielectric, non-magnetic rod of circular cross section C, radius R and refractive index $n = \sqrt{\varepsilon}$, where ε is the relative permittivity of the rods, surrounded by air, in a cartesian coordinate system (xyz) of origin O, where the z-axis defines the axis of the rod (see Fig. 4.1). The rod is illuminated by a homogeneous planewave with wavevector $\mathbf{k}$ ($k = |\mathbf{k}| = 2\pi/\lambda$), where λ is the wavelength of light in free space. The problem is harmonic, using an implicit time dependence in $e^{-i\omega t}$, and reduced to two dimensions by assuming that the fields are invariant in translation along the z-axis. For the sake of comparison with recent experimental results [104], the field is E-polarized, although a similar analysis could perfectly be carried out for the H-polarization.

The scattered electric field $\mathbf{E}^s$ ($E^s = |\mathbf{E}^s|$) is defined at any point of space outside the rod as the difference between the total and the incident fields $\mathbf{E}$ ($E = |\mathbf{E}|$) and $\mathbf{E}^i$ ($E^i = |\mathbf{E}^i|$), respectively. The total electric field satisfies the homogeneous Helmholtz equation, in the sense of distributions:

$$\nabla^2 E + k^2 \tilde{\varepsilon} E = 0$$

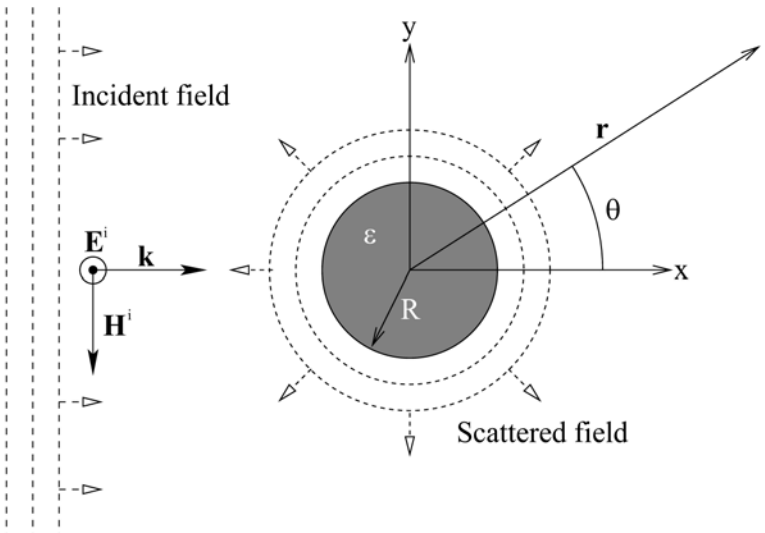

Figure 4.1: Schematic of the system under study and description of the notation used in the text.

where

$$\tilde{\varepsilon} = \begin{cases} \varepsilon, & \text{inside the rod;} \\ 1, & \text{otherwise.} \end{cases}$$

Since the incident field E^i also satisfies the homogeneous Helmholtz equation, the scattered field E^s meets the inhomogeneous Helmholtz equation

$$\nabla^2 E^s + k^2 E^s = k^2(1-\tilde{\varepsilon})E$$

Its solution is found by using Green's theorem [194], making it possible to describe the scattered field (here in a vectorial form) at any point of space $\mathbf{r}$ outside the rod as [117]:

$$\mathbf{E}^s(\mathbf{r}) = \frac{ik^2}{4}\int_C H_0^{(1)}(k|\mathbf{r}-\mathbf{r}'|)(\varepsilon-1)\,\mathbf{E}(\mathbf{r}')\,d^2r' \tag{4.1}$$

with $\mathbf{r}$ and $\mathbf{r}'$ the observation and source points, respectively, and $H_0^{(1)}$ the zeroth-order Hankel function of the first kind, to fulfill the radiation condition of outgoing waves. The integral is made on C only, since $(1-\tilde{\varepsilon}) = 0$ outside the rod.

The scattered field can be expanded into a Bessel-Fourier series as:

$$\mathbf{E}^s(\mathbf{r}) = \sum_{m=-\infty}^{\infty} b_m H_m^{(1)}(kr)e^{im\theta}\mathbf{u}_z \tag{4.2}$$

where θ is the angle formed by $\mathbf{r}$ with respect to the x-axis, b_m the mth-order coefficient describing the scattered field and $\mathbf{u}_z$ the unit vector pointing toward the positive z-direction. Supposing that the incident planewave propagates along the positive x-direction, the incident electric field $\mathbf{E}^i$ can be written in a Bessel-Fourier series as:

$$\mathbf{E}^i(\mathbf{r}) = e^{ikx}\mathbf{u}_z = e^{ikr\cos\theta}\mathbf{u}_z = \sum_{m=-\infty}^{\infty}(i)^m J_m(kr)e^{im\theta}\mathbf{u}_z$$

where J_m is the mth-order Bessel function of the first kind.

As discussed in Sec. 1.5, the scattering matrix $\mathbf{S}$ relates the incident and scattered fields of a system. In the case of circular dielectric cylinders, exact expressions of its coefficients $s_m = b_m/(i)^m$ (the Mie scattering coefficients) can be found by imposing the continuity of the tangential fields on the boundary of the rod [100]. It is found that:

$$s_m = \frac{J_m(knR)J'_m(kR) - nJ_m(kR)J'_m(knR)}{J_m(knR)H_m(kR) - nH'_m(kR)J'_m(knR)} \tag{4.3}$$

where primes denote derivatives. The superscript $^{(1)}$ of the Hankel functions has been omitted for the sake of readability. This expression describes exactly the scattering of light by a dielectric rod in terms of different scattering modes. These are precisely the different multipoles we are interested in. The next step of our approach is to relate these coefficients to classical formulae of radiating dipoles.

4.1.2 Far-field matching to radiating dipoles

The electric and magnetic dipoles can be found by expanding the scattered electric field into a series of multipoles. Since the exact charge displacements and displacement currents taking place in the rod can complicate the approach to the problem, some approximations need to be taken. Three different length scales can be considered: the wavelength of light λ, the spatial extension of the source, i.e. the spatial distribution of displacement currents, and the distance from the source to the observation point. Typical radiation problems are usually simplified by studying the radiated fields at either small or large distances compared to the wavelength of light and the spatial extension of the source. These are respectively the so-called near and far-field approximations. In our case, we would like to replace a rod of finite radius by a radiating point dipole. The correct approach is therefore to take the far-field approximation, i.e. to look at the field scattered by the rod in the far zone and find out what dipole would radiate a similar field pattern. By doing so for the first two scattering orders, we expect to retrieve analytic expressions of the electric and magnetic polarizabilities of the rods.

Scattered field in the far zone

First, we need to find an expression of the scattered electric field in the far zone in terms of scattering matrix components in Eq. (4.3). The Hankel function $H_m^{(1)}(kr)$ can be written using its asymptotic form as [119]:

$$H_m^{(1)}(kr) \approx \sqrt{\frac{2}{\pi}}\frac{e^{ikr}}{\sqrt{kr}}e^{-i\pi/4}(-i)^m$$

which yields

$$\mathbf{E}^s(\mathbf{r}) \approx \sqrt{\frac{2}{\pi}}\frac{e^{ikr}}{\sqrt{kr}}e^{-i\pi/4}\left(s_0 + 2\sum_{m=1}^{\infty} s_m \cos(m\theta)\right)\mathbf{u}_z \tag{4.4}$$

where we have used the fact that $s_{-m} = s_m$. Let us note that this expression explicitely exhibits the angular dependence of the different modes.

Second, the different scattering orders of (4.4) are found by developing the far-field expression of (4.1) into a series of multipoles. It is worth noting that this technique differs from the familiar 3D multipole expansion of the magnetic vector-potential [116] because the bidimensionality of our problem implies a strong effect of the light polarization on the scattered field. We start by writing the Hankel function

$H_0^{(1)}(k|\mathbf{r}-\mathbf{r}'|)$ in the far zone using its asymptotic form:

$$H_0^{(1)}(k|\mathbf{r}-\mathbf{r}'|) \approx \sqrt{\frac{2}{\pi}} \frac{e^{ik|\mathbf{r}-\mathbf{r}'|}}{\sqrt{k|\mathbf{r}-\mathbf{r}'|}} e^{-i\pi/4}$$

Further simplification is then obtained by keeping only the dominant terms of this expression for large values of r in comparison to the wavelength λ. $k|\mathbf{r}-\mathbf{r}'|$ is written in powers of $1/r$ and developed to the first order via the binomial theorem:

$$k|\mathbf{r}-\mathbf{r}'| = kr\sqrt{1 - 2\frac{\mathbf{r}\cdot\mathbf{r}'}{r^2} + \frac{r'^2}{r^2}} \approx k(r - \mathbf{u}_r \cdot \mathbf{r}')$$

where $\mathbf{r} = r\mathbf{u}_r$. The dependence of the scattered electric field in $k|\mathbf{r}-\mathbf{r}'|$ takes place in the phase ($e^{ik|\mathbf{r}-\mathbf{r}'|}$) and in the amplitude ($1/\sqrt{k|\mathbf{r}-\mathbf{r}'|}$) of the Hankel function. Since slight changes of $k|\mathbf{r}-\mathbf{r}'|$ are expected to have a much stronger impact on the phase than on the amplitude, it is sufficient to keep the zeroth-order term of the development for the amplitude term, such that $\sqrt{k|\mathbf{r}-\mathbf{r}'|} \approx \sqrt{kr}$. The scattered electric field in Eq. (4.1) therefore becomes:

$$\mathbf{E}^s(\mathbf{r}) = \sqrt{\frac{2}{\pi}} \frac{e^{ikr}}{\sqrt{kr}} e^{-i\frac{\pi}{4}} \frac{ik^2}{4} \int_C e^{-ik\mathbf{u}_r\cdot\mathbf{r}'} (\varepsilon - 1)\, \mathbf{E}(\mathbf{r}')\, d^2r' \tag{4.5}$$

The multipole expansion is then introduced by writing the exponential $e^{-ik\mathbf{u}_r\cdot\mathbf{r}'}$ in powers of the source extension versus the wavelength:

$$e^{-ik\mathbf{u}_r\cdot\mathbf{r}'} = \sum_{m=0}^{\infty} \frac{(-ik\mathbf{u}_r\cdot\mathbf{r}')^m}{m!}$$

By inserting this expression in (4.5), we obtain the *polarized multipole expansion* of the electric field scattered by a rod in the far zone:

$$\mathbf{E}^s(\mathbf{r}) = \sqrt{\frac{2}{\pi}} \frac{e^{ikr}}{\sqrt{kr}} e^{-i\frac{\pi}{4}} \frac{ik^2}{4} \sum_{m=0}^{\infty} \frac{(-ik)^m}{m!} \int_C (\mathbf{u}_r\cdot\mathbf{r}')^m\, (\varepsilon - 1)\mathbf{E}(\mathbf{r}')d^2r' \tag{4.6}$$

The successive terms of Eq. (4.6) can now be identified with the classical dipole radiation fields at large distances, and related to the different orders of the scattering matrix in Eq. (4.4).

Electric dipole

The electric dipole is the first term appearing in a multipole expansion of radiating fields, corresponding to the order $m = 0$ in Eqs. (4.4) and (4.6). The latter equation becomes:

$$\mathbf{E}_0^s(\mathbf{r}) = \sqrt{\frac{2}{\pi}} \frac{e^{ikr}}{\sqrt{kr}} e^{-i\frac{\pi}{4}} \frac{ik^2}{4} \int_C (\varepsilon - 1)\mathbf{E}(\mathbf{r}')d^2r' \tag{4.7}$$

By definition, the electric dipole moment (per unit length) is given by [116]:

$$\mathbf{p} = \int_C \mathbf{P}(\mathbf{r}')d^2r'$$

with $\mathbf{P} = \varepsilon_0(\varepsilon - 1)\,\mathbf{E}$, the polarization density and ε_0 the free space permittivity. Equation (4.7) can therefore be written as:

$$\mathbf{E}_0^s(\mathbf{r}) = \sqrt{\frac{2}{\pi}}\frac{e^{ikr}}{\sqrt{kr}}\,e^{-i\frac{\pi}{4}}\frac{ik^2}{4}\frac{\mathbf{p}}{\varepsilon_0}$$

which yields, by equating this expression with the zeroth-order term of Eq. (4.4):

$$\frac{\mathbf{p}}{\varepsilon_0} = \frac{4s_0}{ik^2}\mathbf{u}_z \tag{4.8}$$

The electric polarizability tensor $\bar{\bar{\alpha}}^e$ is defined by $\mathbf{p} = \varepsilon_0\bar{\bar{\alpha}}^e\mathbf{E}^i$. Since the incident electric field has been normalized to unity, the electric polarizability of the dielectric rod in the case of E-polarization is:

$$\alpha_{zz}^e = \frac{4s_0}{ik^2} \tag{4.9}$$

It can be shown that the electric polarizability obtained from this formula compares remarkably well with that using Eq. (11) of Ref. [193] (a time dependence in $e^{i\omega t}$ was used, so that the complex conjugates of the scattering coefficients have to be taken). Naturally, Eq. (4.9) can also be applied to rods with a complex permittivity $\varepsilon = \varepsilon' + i\varepsilon''$, a negative permittivity $\varepsilon < 0$ as well as to metallic rods when ε tends toward $-\infty$. The strong point of this relation is its simplicity and reliability, noting also that all resonances of the electric dipole are taken into account, not only the lowest one. As we will see in the next section, this property has a particular importance for the calculation of higher-order bands in the photonic band structure of periodic arrays of rods.

Magnetic dipole

Similar steps can now be carried out to derive the magnetic polarizability of dielectric rods. The first-order term of Eq. (4.6) can be written as:

$$\mathbf{E}_1^s(\mathbf{r}) = \sqrt{\frac{2}{\pi}}\frac{e^{ikr}}{\sqrt{kr}}\,e^{-i\frac{\pi}{4}}\frac{ik^2}{4}(-ik)\int_C(\mathbf{u_r}\cdot\mathbf{r}')\,(\varepsilon-1)\mathbf{E}(\mathbf{r}')d^2r' \tag{4.10}$$

The magnetic dipole moment per unit length is given by [116]:

$$\mathbf{m} = \frac{1}{2}\int_C \mathbf{r}'\times\mathbf{J}(\mathbf{r}')d^2r'$$

with $\mathbf{J} = \partial\mathbf{P}/\partial t$ the current density, which, considering a time dependence in $e^{-i\omega t}$, becomes $\mathbf{J} = -i\omega\varepsilon_0(\varepsilon-1)\mathbf{E} = \frac{-ik}{Z_0}(\varepsilon-1)\mathbf{E}$, where $Z_0 = \sqrt{\mu_0/\varepsilon_0}$ is the free space impedance and μ_0 the free space permeability. Equation (4.10) can therefore be written as:

$$\mathbf{E}_1^s(\mathbf{r}) = \sqrt{\frac{2}{\pi}}\frac{e^{ikr}}{\sqrt{kr}}\,e^{-i\frac{\pi}{4}}\frac{ik^2}{4}Z_0\int_C(\mathbf{u}_r\cdot\mathbf{r}')\,\mathbf{J}(\mathbf{r}')d^2r'$$

This expression can be simplified by using the triple product rule, $(\mathbf{u}_r\cdot\mathbf{r}')\,\mathbf{J}(\mathbf{r}') = \mathbf{r}'(\mathbf{u}_r\cdot\mathbf{J}(\mathbf{r}')) - \mathbf{u}_r\times(\mathbf{r}'\times\mathbf{J}(\mathbf{r}'))$. We note in particular that $\mathbf{u}_r$ and $\mathbf{J}(\mathbf{r}')$ are orthogonal to each other, so that their scalar product equals zero. Because of the translational invariance of the fields imposed along the z-axis, the electric quadrupole and magnetic dipole contributions to the scattered electric field cannot be separated

as in 3D. After this simplification, and placing $\mathbf{u}_r$ out of the integral, we obtain:

$$\begin{aligned}\mathbf{E}_1^s(\mathbf{r}) &= \sqrt{\frac{2}{\pi}}\frac{e^{ikr}}{\sqrt{kr}}\,e^{-i\frac{\pi}{4}}\frac{ik^2}{4}Z_0\left(\int_C \mathbf{r}'\times\mathbf{J}(\mathbf{r}')d^2r'\right)\times\mathbf{u}_r \\ &= \sqrt{\frac{2}{\pi}}\frac{e^{ikr}}{\sqrt{kr}}\,e^{-i\frac{\pi}{4}}\frac{ik^2}{4}2Z_0\mathbf{m}\times\mathbf{u}_r\end{aligned}$$

which, by equalization with the first-order term of Eq. (4.4), yields:

$$Z_0\mathbf{m}\times\mathbf{u}_r = \frac{4s_1}{ik^2}\cos\theta\mathbf{u}_z \tag{4.11}$$

In the case of E-polarized light propagating along the positive x-direction and for a magnetic dipole on the y-axis, Eq. (4.11) becomes:

$$Z_0\mathbf{m} = \frac{-4s_1}{ik^2}\mathbf{u}_y \tag{4.12}$$

The corresponding magnetic polarizability tensor $\bar{\bar{\alpha}}^m$, defined by $\mathbf{m} = \bar{\bar{\alpha}}^m\mathbf{H}^i$, where $H^i = E^i/Z_0$ is the amplitude of the incident magnetic field, therefore equals:

$$\alpha_{yy}^m = \frac{4s_1}{ik^2} \tag{4.13}$$

This expression shows that dielectric rods in E-polarized fields exhibit a true magnetic dipole moment, due to the field-induced response of the rods and not to their magnetization (the relative permeability μ of the rods has been set to unity). This rigorous theoretical demonstration constitutes a solid basis for the investigation of the capability of arrays of dielectric rods to produce a dispersive permeability. Before moving on to the macroscopic scale, we have to check that the electric and magnetic dipole coefficients are sufficient to describe the optical properties of arrays of rods.

4.1.3 Resonances of high refractive index rods

Describing the optical properties of a collection of rods with only their first two Mie scattering coefficients, s_0 and s_1, supposes that these are significantly more important than the higher-order coefficients. High refractive indices have the advantage of placing the working frequency range in the long wavelength limit (typically close to the lower-frequency magnetic dipole resonance), but also they increase the quality factor of the rods, sharpening their resonance peaks and thus reducing their probability to overlap. Figure 4.2 shows the complex moduli of the s_0, s_1 and s_2 coefficients of rods of permittivity $\varepsilon = 600$ as a function of the normalized frequency R/λ and the amplitude of the scattered electric field at different resonance wavelengths. Except at the resonance frequencies of the s_2 (and higher-order) coefficients, the s_0 and s_1 coefficients dominate the optical response of the individual rods. The s_0 coefficient remains particularly large between consecutive resonances, exhibiting a rather weak electric field localization. This suggests that it plays the key role in the optical properties of the structure. The s_1 coefficient on the other hand is much more spectrally localized, also strongly confining the light to the rod, and thus is expected to yield dramatic modifications of light propagation in very narrowband frequency ranges. The existence of the magnetic dipole along the y-direction can be explained by the two electric field lobes of opposite signs at the resonance of the s_1 coefficient, which create strong counter-propagative currents in the dielectric rod. The resonance of the s_2 coefficient is also very sharp and occurs at frequencies close to the second resonance of the s_0 coefficient, which will probably slightly perturb the propagation of light in a small frequency range. Based on these observations, we can confidently say that considering the

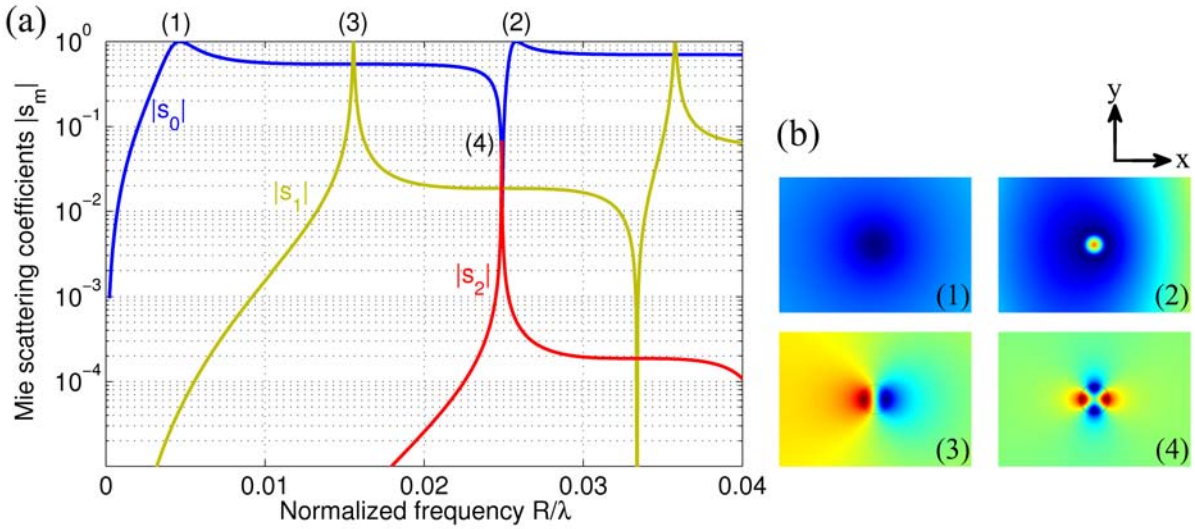

Figure 4.2: (a) Complex moduli of the s_0 (blue solid line), s_1 (green solid line) and s_2 (red solid line) Mie scattering coefficients of a circular rod of radius R and permittivity $\varepsilon = 600$, in logarithmic scale versus the normalized frequency R/λ. (b) Amplitude of the electric field scattered by the high-permittivity rod E^s at the normalized frequencies $R/\lambda = 4.65\,10^{-3}$ (1), $25.8\,10^{-3}$ (2), $15.6\,10^{-3}$ (3) and $24.9\,10^{-3}$ (4).

electric and magnetic dipole activities of rods is sufficient to describe the main features of the optical properties of arrays of such rods.

4.2 All-dielectric rod-type metamaterials operating at optical properties

Describing the macroscopic properties of arrangements of microscopic resonators involves one of the most fundamental aspect of MMs, which is their homogeneity. Although composed by a set of microscopic elements, a MM is said to be homogeneous when it can be described by some effective macroscopic parameters, a permittivity and a permeability. The homogeneous regime commonly refers to the long wavelength limit, where the wavelength of light λ is much larger than the characteristic length of the MM, e.g. the lattice periodicity in the case of periodic structures. In this way, light in the MM only "sees" a spatially averaged medium and not a discretized set of scatterers. Following this definition, it has been well accepted among the scientific community that PhCs do not belong to the class of MMs because their lattice periodicity is precisely of the order of the wavelength of light (the inhomogeneous regime) [24, 195, 196]. In Chapter 1, we made a distinction on the definitions of PhCs and MMs, being that the former rely on periodicity effects and the latter on a collective response of coupled resonators. Dielectric rods have been a building block of early (rod-type) PhCs, yet they exhibit both electric and magnetic dipole resonances, just like the most typical resonators in metallic MMs. This leads us naturally to the question: can arrays of dielectric rods be defined as MMs in the strict sense of the term?

In order to be able to treat them as homogeneous media, previous studies on all-dielectric MMs have used high refractive indices to place the Mie resonances in the long wavelength limit [103–105, 187]. Various facts can however cast doubt upon this necessity. The first one is the simple remark that even metallic MMs are more and more being used in the region $\lambda/a \approx 2$, where a is the lattice periodicity [197]. This is the actual range of operation of PhCs, which actually denotes the greater importance of coupled

resonances over homogeneity. Moreover, previous studies on spheres and rods of moderate refractive indices (e.g. silicon) have observed a correlation between the Mie resonances of their individual elements and the opening of photonic band gaps (PBGs) in arrays of them [198–200]. Some of these PBGs have also been shown to be only weakly perturbed when structural disorder was introduced [201]. These phenomena, typical of MMs, occur in the inhomogeneous regime. They are not inherent to the lattice periodicity but precisely to coupled resonances. Based on these observations and our previous conclusions, it is tempting to suggest that all-dielectric rod-type structures, even in the inhomogeneous (PhCs) range, may be defined as MMs in the strict sense of the term. We can already predict that this would be subject to the condition that the electric and magnetic dipole activities of the rods would be predominant over periodicity effects. To verify this idea, we will follow the classical bottom-up approach of MMs, which consists of homogenizing a set of microscopic resonators (the dielectric rods in our case) to retrieve the macroscopic parameters of the effective medium.

4.2.1 Optical properties of square arrays of rods

The arrival of MMs in the common scientific knowledge came along with a few intuitive methods of homogenization capable of retrieving effective material parameters quite accurately. The S-parameter retrieval technique [202] consists of matching the reflection and/or transmission coefficients of a finite-size or semi-infinite structure to a homogeneous medium of the same dimension. Although this technique has been proved to be reliable in many cases, it fully relies on the existence of a boundary between the MM and free-space. The electric permittivity and magnetic permeability of a continuous medium are, by definition, macroscopic parameters related to the *bulk* structure and in this sense, it should not involve boundary effects. It becomes very useful, however, when comparison to or prediction of experimental results on real-world structures is needed. On the same level, the field averaging technique has also met a great success [203]. The local field is spatially averaged to yield a set of macroscopic fields, which, using the constitutive relations of electromagnetic fields, make it possible to retrieve the effective parameters of the medium. This approach can be simply implemented on planewave expansion (PWE), finite-difference time-domain (FDTD) or finite-element (FE) methods. O'Brien and Pendry also adapted it to Mie scattering theory to find an approximate analytical expression of the effective permeability of arrays of dielectric rods in H-polarization [101].

The S-parameter retrieval and the field averaging techniques are both very well adapted to design and optimization studies since they do not focus on the properties of the invidual resonators but on the array of resonators as a whole, and thus make it possible to study very complex structures. In our case, however, we know about the properties of the individual resonators and we would like to study how they interact and collectively behave. The more classical homogenization techniques therefore seem to better fit these requirements. The concept of homogenization has first seen the light in the nineteenth century with the works of Lorenz, Lorentz, Clausius, Mossotti and Lord Rayleigh and later with those of Maxwell-Garnett and Bruggeman [204]. Their common objective was to describe the macroscopic properties of a medium from those of its constituents and their relative fractions. The Clausius-Mossotti (Lorenz-Lorentz) formula relates the polarizability of the individual microscopic elements to the permittivity of the medium and the Maxwell-Garnett mixing rule defines an effective permittivity directly from the permittivity of its constituents. These formulae have been adapted, for example, to retrieve the effective permittivity and permeabillity of arrays of high-permittivity spheres with and without a polaritonic dispersion [103, 185, 186]. Recently, various papers [205, 206] adopted an approach based on the Lorentz theory [207]. It basically relies on a multiple-scattering scheme similar to that described in Sec. 1.5,

describing the interactions of neighboring scatterers on an individual scatterer via the introduction of interaction fields. This approach is particularly appealing because it captures the electrodynamics of composite media in a very intuitive way. This approach has been used to study electromagnetic interaction with 2D arrays of conducting disks and 3D arrays of arbitrary resonators (e.g. split-ring resonators) among other types of structures. Here, we will use a nonlocal homogenization model recently proposed by Silveirinha [193], which applies specifically to square arrays of rods. The term "nonlocal" points out some spatial dispersion, or anisotropy effects, which can be taken into account.

Homogenization model

Let us first draw the main lines of this method. We consider a 2D square array of identical microscopic scatterers (the rods) with electric and magnetic polarizabilities $\bar{\bar{\alpha}}^e$ and $\bar{\bar{\alpha}}^m$, respectively. Since this technique relies on the use of dipole terms only, the cross-section of the scatterers should be small compared to the lattice periodicity and the wavelength should be large compared to these two dimensions. In this limit, the external electric and magnetic macroscopic fields, $\mathbf{E}$ and $\mathbf{H}$, applied on the dielectric medium can be approximated as uniformly distributed in space and thus, represented as spatially averaged fields. The homogenization process means to replace the array of scatterers by a continuous medium with relative permittivity $\bar{\bar{\varepsilon}}$ and permeability $\bar{\bar{\mu}}$. The corresponding average electric displacement $\mathbf{D}$ and magnetic induction $\mathbf{B}$ are given by:

$$\mathbf{D} = \varepsilon_0 \mathbf{E} + \mathbf{P} = \varepsilon_0 \bar{\bar{\varepsilon}} \mathbf{E} \tag{4.14a}$$

$$\mathbf{B} = \mu_0 (\mathbf{H} + \mathbf{M}) = \mu_0 \bar{\bar{\mu}} \mathbf{H} \tag{4.14b}$$

where $\mathbf{P} = N\mathbf{p}$ and $\mathbf{M} = N\mathbf{m}$ are the average polarization density and magnetization of the medium, N the density of dipoles and $\mathbf{p}$ and $\mathbf{m}$ the electric and magnetic dipole moments of the individual microscopic scatterers embedded in the composite medium. The net field that effectively polarizes a single scatterer, located at the origin of the coordinate system, is the sum of the average applied field plus the fields radiated by all the neighboring scatterers. These interaction fields, denoted $\mathbf{E}_{int}$ and $\mathbf{H}_{int}$, are proportional to the dipole moments and may be expressed via some interaction constants $\bar{\bar{C}}^e$ and $\bar{\bar{C}}^m$ as $\mathbf{E}_{int} = \bar{\bar{C}}^e \mathbf{p}/\varepsilon_0$ and $\mathbf{H}_{int} = \bar{\bar{C}}^m \mathbf{m}$. The electric and magnetic dipole moments of the scatterer located at the origin can then be written as:

$$\mathbf{p} = \bar{\bar{\alpha}}^e \varepsilon_0 (\mathbf{E} + \mathbf{E}_{int}) = \frac{\varepsilon_0 \bar{\bar{\alpha}}^e}{1 - \bar{\bar{C}}^e \bar{\bar{\alpha}}^e} \mathbf{E} \tag{4.15a}$$

$$\mathbf{m} = \bar{\bar{\alpha}}^m (\mathbf{H} + \mathbf{H}_{int}) = \frac{\bar{\bar{\alpha}}^m}{1 - \bar{\bar{C}}^m \bar{\bar{\alpha}}^m} \mathbf{H} \tag{4.15b}$$

Using Eq. (4.15) and Eq. (4.14), we find an expression for the effective permittivity and permeability of the composite medium:

$$\bar{\bar{\varepsilon}} = 1 + N \frac{\bar{\bar{\alpha}}^e}{1 - \bar{\bar{C}}^e \bar{\bar{\alpha}}^e} \tag{4.16a}$$

$$\bar{\bar{\mu}} = 1 + N \frac{\bar{\bar{\alpha}}^m}{1 - \bar{\bar{C}}^m \bar{\bar{\alpha}}^m} \tag{4.16b}$$

We understand at this point that once the polarizability of the scattering elements of a composite medium is known, the remaining step is to derive the interaction constant. This derivation has been clearly described by Silveirinha in the case of square array of rods (assuming a time dependence in $e^{i\omega t}$)

in Ref. [193]. In what follows, we use the following expression for the interaction constant:

$$C = k^2 \left(\frac{i}{4} + \frac{1}{2\pi} \ln\left(\frac{ka}{4\pi}\right) + \frac{\gamma}{2\pi} + \frac{1}{12} + \sum_{n=1}^{\infty} \frac{1}{\pi|n|} \frac{1}{e^{2\pi|n|} - 1} \right)$$

where γ is the Euler constant. This expression of the interaction constant is an approximation taken in the long-wavelength limit and under the condition that the cross-section of the rods is much smaller than the lattice constant. It also does not take into account the full interaction of dipoles out of the normal to the propagation plane (i.e. out of the z-axis), this would require further investigation. Note however that our purpose here is not to reconstruct accurately the dispersion curves of an array of dielectric rods but to show that arrays of dielectric rods can be treated as metallic MMs and that similar effects can be obtained. This expression of the interaction constant is sufficient for the sake of the demonstration.

Before moving on, it is also worth noting that the expressions of $\bar{\bar{\varepsilon}}$ and $\bar{\bar{\mu}}$ in Eqs. (4.16) neglect the existence of cross-polarized coupling between magnetic and electric dipoles. Since this coupling originates from the interaction fields only, it is intrinsically small and thus should not influence significantly our results. Examples of the derivation of cross-coupling interaction constants can be found in Refs. [207,208].

Effective dispersion curves

We are now equipped to calculate the effective parameters of square arrays of dielectric rods using the electric and magnetic polarizabilities found in Sec. 4.1. We apply the nonlocal homogenization technique described above in the approximation of wavevectors close to the Γ-point and in the long-wavelength limit on a square array of rods of permittivity $\varepsilon = 600$ and radius $R = 0.68a/3$, where a is the lattice periodicity. For the sake of comparison, this structure is similar to the one studied by Peng *et al.* [104]. In the case of light propagating along the x-direction (this is, of course, an arbitrary direction), only the ε_{zz} and μ_{yy} components are required to define the effective index of the material $n_{eff} = \sqrt{\varepsilon_{zz}\mu_{yy}}$. The calculated effective permittivity and permeability, plotted in Fig. 4.3(a), exhibit strong resonances, owing to the electric and magnetic dipole resonances of the individual rods. This shows especially that arrays of rods in E-polarized light indeed exhibit a magnetic activity. It should also be remarked that the effective permittivity matches exactly its static limit obtained from the classical mixing formula in nondispersive media [204], $\varepsilon_{zz} = f\varepsilon + (1 - f) \approx 98$, where f is the filling fraction of the rods.

The photonic band structure of the effective material can now be calculated by using the dispersion relation $k_x = n_{eff}\omega/c$ and compared with that of the corresponding array of high-permittivity rods calculated in 2D with the PWE method. The dispersion curves shown in Fig. 4.3(b) are in excellent agreement, especially at wavevectors close to the Γ-point, which was an approximation that we initially took. The noticeable differences are the degeneracy of the second band at the Γ-point, which is due to the symmetry of the magnetic dipole, and the extremely flat dispersion curve at $a/\lambda \approx 0.11$, which results from the resonance of the s_2 Mie scattering coefficient. Similarly, a study of higher-order bands shows that the dispersion curves that appear in the photonic band structure can be attributed to the resonances of the rods.

Thus, apart from symmetry degeneracies and higher-order resonances, which have not been taken into account here, the main features of the photonic band structure of the square array of rods are well reproduced. The first and second PBGs both originate from the first electric dipole resonance of the rods, corresponding to a frequency region of negative permittivity. The magnetic dipole resonance of the rods creates a resonance of the effective permeability, which takes negative values at reduced frequencies $a/\lambda \approx 0.07$ and result in the creation of a left-handed dispersion curve that intersects the original PBG.

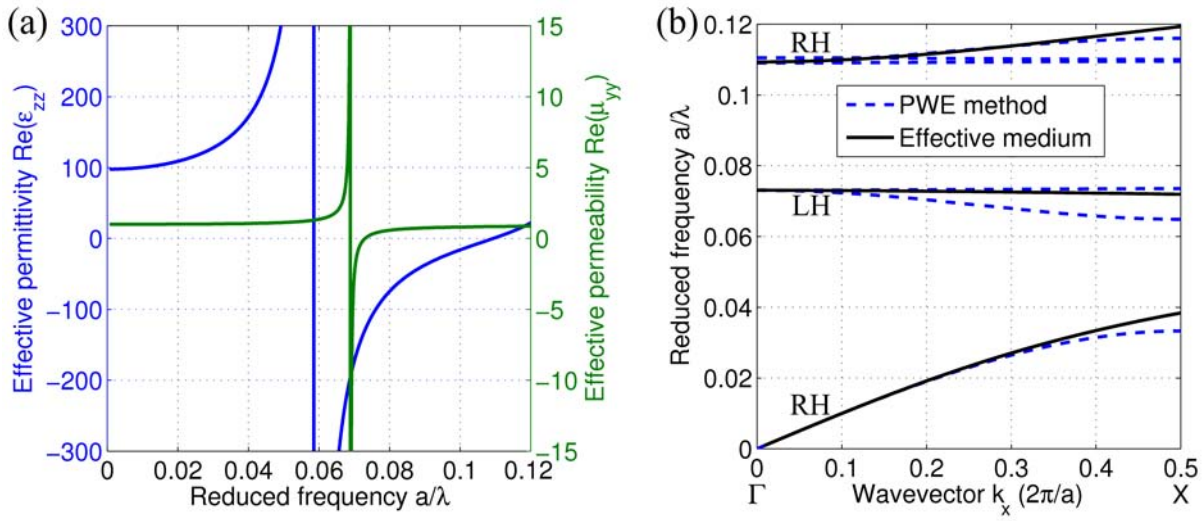

Figure 4.3: (a) Real parts of the effective permittivity ε_{zz} (blue solid line) and permeability μ_{yy} (green solid line) of a square array of rods ($R = 0.68a/3$, $\varepsilon = 600$) versus the reduced frequency a/λ. (b) Dispersion curves of the PhC along the ΓX direction of the square array of rods, calculated with the PWE method (blue dashed lines) and using the effective material parameters (black solid lines). The right-handed (RH) and left-handed (LH) nature of the curves is indicated on the photonic band structure.

When occuring in the frequency range of a right-handed dispersion curve ($\varepsilon > 0$), a resonance of the permeability ($\mu < 0$) would yield the opening of a PBG. This is actually what happens in arrays of high-permittivity rods in H-polarization [101]. Our results make it clear that *the optical properties of periodic arrays of rods result from the collective response of the resonant rods*, which rigorously demonstrates the ability of arrays of dielectric rods to control light in a similar way as metallic MMs.

4.2.2 Scaling to the optical frequencies

Due to the increasing interest in developing MMs for the optical frequencies, it is now important to investigate the scaling properties of these structures. Previous studies have limited their work to high-permittivity rods to place their resonances in the homogeneous regime ($\lambda \gg a, R$) and prevent them from exhibiting a strong spatial dispersion [104, 105, 184]. Our theory provides additional information on this subject. As shown above, the electric and magnetic dipole activities of dielectric rods are intrinsically related to their Mie scattering coefficients. The scaling properties of rod-type structures may therefore be understood from the dependence of these coefficients with the permittivity ε of the rods and the free space wavelength λ. Figure 4.4 shows the complex moduli of the electric (s_0) and magnetic (s_1) dipole coefficients of the rods with respect to their refractive index $n = \sqrt{\varepsilon}$ and to the wavelength-to-radius ratio λ/R. In the range of study, the resonance wavelengths exhibit a quasi-linear dependence with the refractive index of the rods. For relatively large refractive indices, the resonances indeed scale with the optical size of the rods (nR being their optical radius). The magnetic dipole resonance observed in rods of permittivity $\varepsilon = 600$ ($n \approx 24.5$) at reduced frequencies $a/\lambda \approx 0.07$ ($\lambda/R \approx 63$) can be shifted to $a/\lambda \approx 0.5$ ($\lambda/R \approx 8.8$) by using rods of permittivity $\varepsilon = 12$ ($n \approx 3.5$). By calculating the complex moduli of the higher-order Mie scattering coefficients, we can show that this permittivity is sufficiently high for the s_0 and s_1 coefficients to remain dominant over the higher-order coefficients up to the first resonance frequency of the s_2 coefficient at $R/\lambda \approx 0.17$. The left-handed behavior in particular is expected to hold.

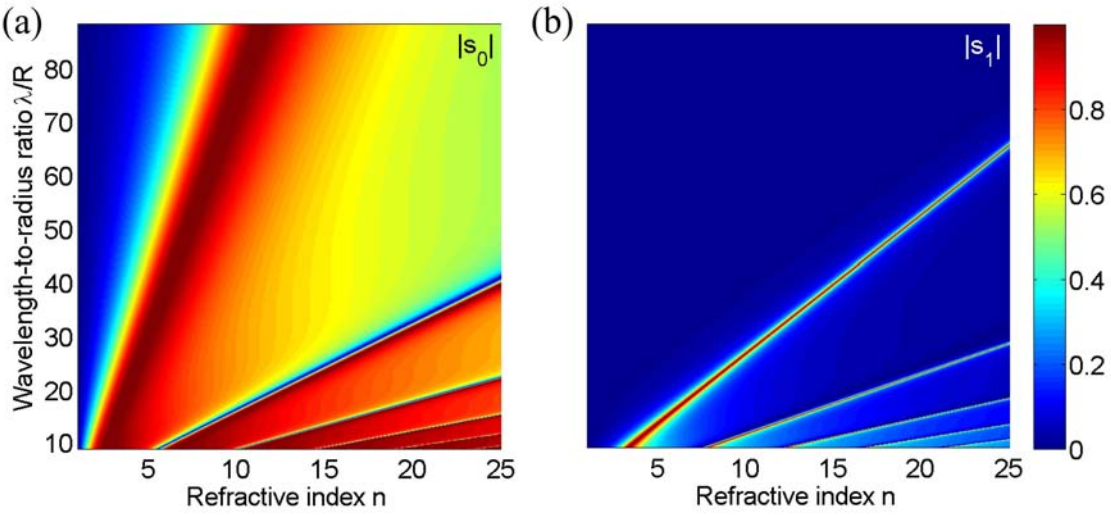

Figure 4.4: Complex moduli of the s_0 (a) and s_1 (b) Mie scattering coefficients of dielectric rods with radius R as a function of their refractive index $n = \sqrt{\varepsilon}$ and the wavelength-to-radius ratio λ/R.

Photonic band structures

This is verified by comparing the photonic band structures of the two structures with rods of permittivity $\varepsilon = 600$ and $\varepsilon = 12$, calculated in 2D with the PWE method. Results are shown in Fig. 4.5. The optical properties of the lowest bands of both structures clearly exhibit the same features. The left-handed curves (in green) lying at reduced frequencies $a/\lambda \approx 0.07$ are pushed up to $a/\lambda \approx 0.5$, as expected. Its broadening is due to the lower quality factor of the rods and a stronger interaction between them, naturally following the decrease of their refractive index [198]. This is an advantage for practical reasons since it broadens the operating bandwidth of the structure in the left-handed frequency range and increases the coupling efficiency. It is commonly believed that the second PBG comes from the s_1 Mie resonance of the rods [201]. Our analysis shows that it is actually the continuation of the PBG created by the electric dipole resonance. This "second" PBG is much smaller than before, reduced by the higher-order band, which corresponds to the permittivity of the effective medium going back to positive values. It is found at lower frequencies precisely because the resonances of the rods are much weaker, resulting in a resonance of the permittivity of a smaller amplitude and thus, in a narrower PBG (more discussion is given below). At higher frequencies, this right-handed band is Bragg diffracted and strongly perturbed by the s_2 resonance of the rods at $a/\lambda \approx 0.75$.

Iso-frequency curves

To go further with our scaling analysis, we plot the iso-frequency curves (IFCs) of the high and low permittivity structures for both the right- and left-handed dispersion curves. We concentrate on the central region of the Brillouin zones, where periodicity effects are avoided. The IFCs of the two structures shown in Fig. 4.6 are very similar to each other. The right-handed bands, which delimit the negative permittivity PBG, have a very isotropic response. They only rely on the electric dipole activity of the rods and do not seem significantly influenced by the structure of the lattice. On the contrary, the left-handed band, which depends on both the electric and magnetic dipole activities of the rods, exhibits a strong spatial dispersion even at wavevectors close to the Γ-point. This observation notably supports previous studies, affirming that large wavelength-to-period ratios do not necessarily result in an isotropic

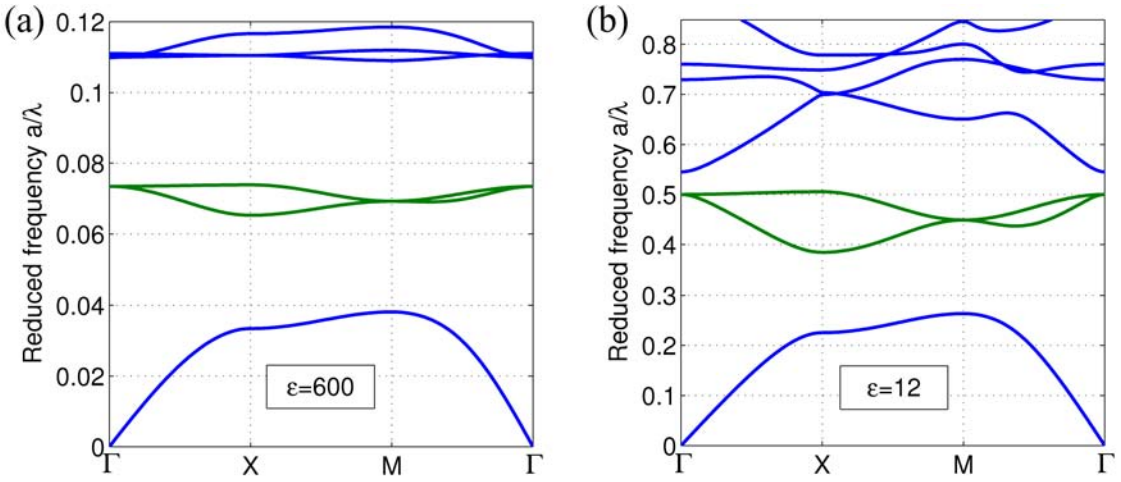

Figure 4.5: Photonic band structures of a square lattice of rods with radius $R = 0.68a/3$ and permittivity $\varepsilon = 600$ (a) and $\varepsilon = 12$ (b). The left-handed curve, resulting from the magnetic dipole resonance of the rods within the negative permittivity PBG, is highlighted is green solid lines.

MM [209–211]. In the electrodynamics of continuous media, it is known that the first-order spatial dispersion is inferred by the magnetic dipole activity of the medium [11]. In fact, spatial dispersion naturally arises as soon as higher-order terms in the multipole expansion of the electric field in powers of a/λ are considered (the magnetic dipole is quadratic in the wavevector k). The symmetry of the structure plays a central role in the spatial dispersion of the MM in the left-handed frequency range precisely because nonlocal effects are very sensitive to structural changes. Being in the long-wavelength limit, and thus, using high refractive index objects, is *absolutely not* a sufficient condition to ensure the isotropic response of a MM.

Going back to our initial hypothesis, we have shown that arrays of high-permittivity rods are indeed MMs in the strict sense of the term, exhibiting resonances of both the effective permittivity and permeability, and further that these effects are not a matter of large wavelength-to-period ratio but simply of interacting resonances. Therefore, we suggest that collections of dielectric rods may be defined and used as MMs as long as the effects of microscopic resonances predominate over periodicity effects. These results constitute *an original point of view on the optical properties of rod-type PhCs*. The different steps described above may be carried out for the dielectric rods in H-polarized fields but may also be applied to metallic rods, thereby opening many perspectives for future works.

True left-handed behavior at near-infrared wavelengths

To illustrate the capability of the all-dielectric MM to exhibit a true left-handed effect at the optical frequencies, we perform a 2D fullwave calculation of an E-polarized field at the reduced frequency $a/\lambda = 0.45$ incident on the structure at an angle of 20°, with the 2D FDTD method. The steady-state amplitude of the electric field is shown in Fig. 4.7, together with the corresponding IFC. The phase of the field propagating in the MM is found to be in an opposite direction compared to that of the field in free space, which indicates, as expected, a left-handed behavior. It is quite remarkable to see the field propagate as in a homogeneous medium. The magnetic dipole resonances of the rods are also clearly visible, which supports the idea that the left-handed effect is due to a collective response of coupled dipoles. This effect can be tuned to the telecommunication wavelengths ($\lambda \approx 1.55$ μm) by using rods of refractive index $n \approx 3.5$ (e.g. silicon), radius $R \approx 160$ nm and a lattice of periodicity $a \approx 700$

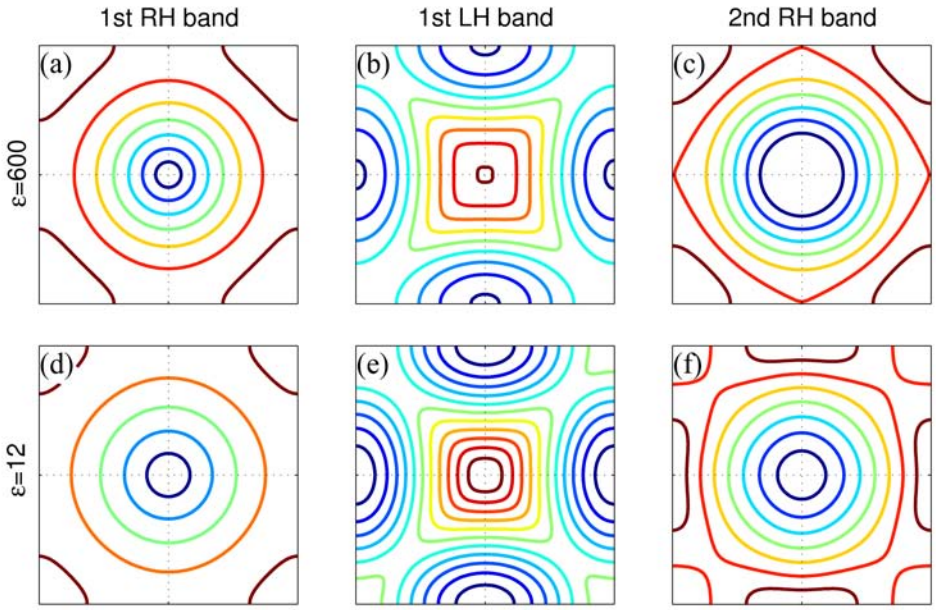

Figure 4.6: IFCs of a square lattice of rods with radius $R = 0.68a/3$ and permittivity $\varepsilon = 600$ (a-c) and $\varepsilon = 12$ (d-f), on the first Brillouin zone of the reciprocal lattice (wavevectors from $-0.5\,(2\pi/a)$ to $0.5\,(2\pi/a)$, not displayed for better readibility). The reduced frequencies a/λ, given in ascending order following the rainbow colors from violet to red, range from (a) 0.005 to 0.035 in steps of 0.005, (b) 0.065 to 0.073 in steps of 0.001, (c) 0.111 to 0.117 in steps of 0.001, (d) 0.05 to 0.25 in steps of 0.05, (e) 0.39 to 0.49 in steps of 0.01, and (f) 0.56 to 0.68 in steps of 0.01.

nm. Since the experimental techniques to fabricate and characterize silicon rod-type PhCs have already been developed [212, 213], we believe that silicon could be a constituent of the early all-dielectric MMs operating in the optical range. From a general point-of-view, the resonances of dielectric rods offer a control over the electric and magnetic response of rod-type structures, but it is worth noting that they cannot be tuned independently. In order to use rod-type MMs in applications such as electromagnetic cloaks, one may think of changing the shape of the cylinders in different regions of the structure in a way to generate different resonances.

In view of future experiments on all-dielectric MMs, it is finally important to discuss the effect of disorder on their optical properties. It is often said that MMs are insensitive to structural disorder, owing to the large wavelength-to-period ratio usually employed and the fact that the optical properties of these structures rely on the resonances of their individual elements and not to their periodicity. Peng *et al.* have made the prism experiment with a disordered rod-type structure and indeed observed a left-handed behavior [104]. Recent studies have however shown that the left-handed properties of metallic MMs could be significantly reduced and eventually suppressed with disorder [214, 215]. Clearly, it would be interesting to know if such effects also occur in all-dielectric rod-type MMs. The propagation of light is disordered structures is, by itself, a complex problem, yielding a vast range of optical phenomena [216] such as strong or weak localization of light, and should therefore be handled with care. Based on our understanding of the principles of light propagation in periodic structures, we can still make a number of hypotheses to explain certain experiments and predict various phenomena qualitatively.

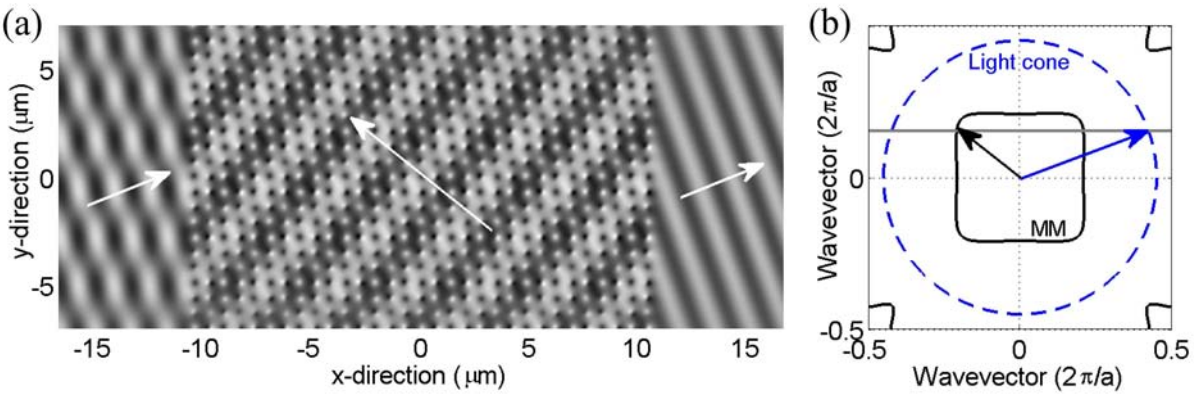

Figure 4.7: (a) Steady-state amplitude of the electric field of an E-polarized field at a reduced frequency $a/\lambda = 0.45$ incident at an angle of 20° on the low-permittivity MM, scaled to a wavelength $\lambda = 1.55$ μm. The white arrows indicate the phase velocity directions of the incident planewave and of the propagating mode in the MM. (b) IFCs of the light cone (blue dashed line) and of the rod-type MM (black solid line) in the first Brillouin zone of the square lattice. The blue and black arrows define the wavevectors of the incident planewave and of the propagating mode in the MM, respectively. The gray solid line represents the conservation of the tangential component of the wavevector at the coupling interface (along the y-direction in this case).

4.2.3 From periodicity to randomness

Disordered arrangements of rods have been studied many years ago in the context of PhCs especially to know how sensitive their PBGs are to disorder [217, 218]. These studies have been motivated on an experimental point of view by the fact that fabrication processes always involve some imperfections. Very rapidly, it has been shown that PBGs in arrangements of dielectric rods were not significantly sensitive to structural disorder because they rely on the Mie resonances of the rods and not on Bragg scattering effects. On the other hand, changing the refractive index of the rods or their size modifies their resonance wavelengths and thus ruins the initial optical properties of the structure. In the context of MMs, this observation has been made by Felbacq and Bouchitté [219] on high-permittivity rods in the H-polarization and by Zharov *et al.* [215] on 3D arrays of split-ring resonators. To approach the problem on the macroscopic scale, let us bring out two main factors that may come into play when structural disorder is introduced: the density of rods and their position.

Disorder in rod-type structures

The effect of the rod density on the macroscopic properties of rod-type structures can be captured directly from the definition of the permittivity and permeability of the effective medium in Eqs. (4.16), via the dipole density N and the interaction constant C (a higher density increases the interaction between the rods). Decreasing (and inversely increasing) the density of rods results in a weaker collective response and resonances of the permittivity and permeability of a smaller amplitude. As a consequence, the edges of the negative permittivity PBG (i.e. the lower edge of the first PBG and the upper edge of the second PBG) are slightly pushed down to lower frequencies and the bandwidth of the left-handed dispersion curve becomes narrower.

Disordered structures are made by regions of different densities, where the coupling between the rods and thus the local behavior of light varies in space. Locally changing the density of a structure can be advantageous for various purposes. For example, arbitrary-shaped waveguides have been designed in

disordered PhCs by creating linear defects of lower density compared to the surrounding structure [220]. Most of the applications now try to minimize disorder. The nearest-neighbor distance is defined with a certain dispersion, which partly depicts the amount of disorder in the structure. The acceptable limit depends on the desired effect. When the disorder is too important, PBGs can be entirely closed, filled by "defect" modes that result from different coupling strengths in different parts of the structure. This effect is expected to be reduced in quasi-periodic structures because their density dispersion is small (see e.g. Ref. [201], where it is suggested that PBGs are sustained as long as a certain filling ratio is exceeded). The effect of disorder on the dispersion curves may be interpreted in a similar way. In their experiment, Peng *et al.* [104] have supposed a uniform distribution of the distance between neighboring rods from about $0.6a$ to $1.2a$, where a is the lattice parameter of the initial periodic structure. All of these densities are sufficiently large for the resonance of the permeability to hold so that light is actually free to propagate through all parts of the MM. We will see below that this simplified picture of disordered structures is actually not as simple as it appears here.

Remaining on the macroscopic level of description, the position of the rods is now another factor that needs to be considered. As we have seen above, the spatial dispersion in periodic structures is inherent to the magnetic dipole activity of the rods. The electric dipole is directed along the normal to the propagation plane and thus, exhibits no preferential direction in this plane. The right-handed dispersion curves, which only rely on the electric dipole activity of the rods, are consequently quite insensitive to positional disorder. This effect is also observed in arrangements of metallic rods where it has been shown that the cut-off frequency is not related to the periodicity of the structure but to the average distance between the rods (i.e. to their density) [221]. The magnetic dipole of a rod, on the other hand, lies in the propagation plane of the structure and thus is locally more sensitive to the position of the neighboring rods. Disorder is however known to make disappear preferential directions, so that the absolute lack of symmetry would actually make the spatial response of the structure more isotropic on average.

Altogether, we expect the left-handed behavior observed in all-dielectric rod-type structures to be sustained up to a relatively high amount of disorder, with the general remark though that heterogeneity should be avoided as much as possible. In this regard, quasi-periodic structures are interesting, for they preserve a relatively low dispersion of the nearest-neighbor distance and lack of rotational and translational symmetry. In fact, negative refraction has been observed experimentally in quasi-periodic structures [222]. More recent studies have also noted the importance of short-range interactions associated with local order and symmetry [223]. Our theoretical analysis above may provide some insight onto these effects. The question of how light behaves on the *microscopic* scale is indeed much more subtle. Owing to the directionality of the magnetic dipoles and the existence of a negative permittivity PBG, disordered structures can possibly yield quite atypical optical effects. It is therefore worth looking at the microscopic behavior of light in disordered rod-type structures into more details.

2D microscopic optical necklace states

To investigate this point, we consider a set of 135 high-permittivity ($\varepsilon = 600$), non-overlapping rods randomly disposed in space. Light is emitted at a wavelength close to the magnetic dipole resonance of the rods ($\lambda/R \approx 63$) from a point source placed above the disordered structure. The norm of the electric field, calculated with the 2D FE method is shown on Fig. 4.8. Light is found to extend over the entire structure in the form of a complex network of coupled resonances. The nodes of the electric field let us distinguish clusters of aligned magnetic dipoles connecting different regions of the structure. Thus, in spite of the disorder, light can easily be transported from one end of the structure to the other. Because of the negative permittivity PBG of the effective medium, the only way light can propagate

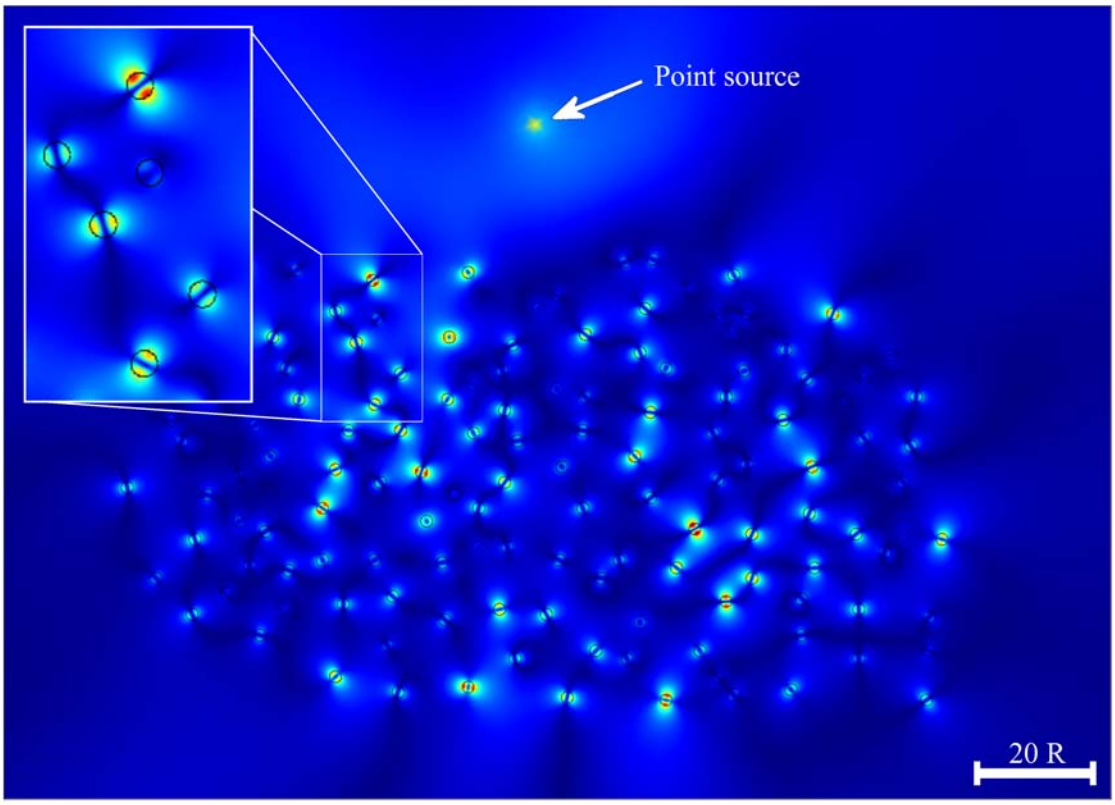

Figure 4.8: Norm of the electric field emitted by a point source placed above a disordered all-dielectric rod-type structure. The clusters of aligned magnetic dipoles, such as that shown on the magnified view in the inset, may be assimilated to 2D microscopic necklace states.

is by using the inner magnetic dipole resonances of the rods. This observation emphasizes the role of these resonances in the electrodynamics of rod-type structures in the left-handed frequency range. These "chains" of resonances also bring to light a theoretically predicted but still unobserved (in 2D) optical effect.

In 1987, Pendry described some counter-intuitive transport properties of electrons in strongly disordered systems where the conduction is no longer dominated by single localized states but by hybrid, delocalized states, which he called necklace states, because they were formed by chains of energy-degenerate resonances [224]. A few years ago, Bertolotti *et al.* showed that similar effects exist for photons by reporting the observation of optical necklace states in 1D disordered structures [225]. To our knowledge, however, there has been no evidence of optical necklace states in 2D and 3D structures up to now. We believe that the modes shown above in 2D disordered rod-type structures can be assimilated to 2D *microscopic* optical necklace states. The high-quality factor rods resonate at the same frequency and hybridize to create extended modes, making it possible for the light to propagate. This effect also occurs at nearby frequencies since the random disposition of the rods results in different coupling strengths and consequently in necklace modes of different frequencies.

This finding actually provides a great opportunity to study 2D optical necklace states experimentally and perhaps make progress on the understanding of the electrodynamics of disordered photonic structures. Moreover, it may be worth investigating the role of optical necklace states in random lasers [226], as it has been shown that extended modes can provide high-efficiency and spectrally narrow lasing modes [227, 228]. Random lasing has recently been demonstrated experimentally in disordered 3D opals

that exploit the Mie resonances of the spheres to transport light [229]. This original result, together with our recent theory on rod-type structures, shows that the idea of using collections of resonant objects to transport light extends far beyond the exciting field of MMs.

Summary

In this chapter, we have provided some novel theoretical insight onto the propagation of light in collections of dielectric rods. We have given a rigorous proof that dielectric rods in E-polarized fields in the long-wavelength limit could be conceptually replaced by radiating electric and magnetic dipoles. The optical properties of square arrays of such rods have been shown to rely intrinsically of these resonances and be described on the macroscopic scale by dispersive permittivity and permeability. In this way, we have demonstrated the fact that collections of rods could be considered exactly as metallic MMs. Interestingly, they have been found to exhibit a true left-handed behavior, resulting for simultaneously negative permittivity and negative permeability. By changing the refractive index of the rods, we have shown that it is possible to scale these effects to the optical frequencies. We have also noted that spatial dispersion is inherent to the magnetic dipole activity of the rods and thus, cannot be reduced by placing the resonances of the rods in the long-wavelength limit. The effect of disorder has been qualitatively analyzed. On the macroscopic scale, the optical properties of rod-type structures are expected to hold as long as the density of rods has a low dispersion. On the microscopic scale, we have seen that light in the magnetic response frequency range is transported by the formation of chains of resonances, which have been identified as 2D microscopic necklace states, opening some perspectives for future studies.

Conclusion

This thesis has been concerned with the study of the optical properties of photonic crystals and metamaterials to provide reliable solutions for an advanced control over light, while aiming at realistic designs from a technological point of view. Nanostructured materials offer a broad panel of different ways to manipulate electromagnetic fields. The work presented here considers several of them.

One particularly interesting aspect of photonic crystals is their ability to confine light to structural defects. In Chapter 2, we have focused on the design of cavities and waveguides in opal-based photonic crystals, motivated by the fact that they can be reproduced on large scales, at low cost and with a high quality. Various ways to reach this objective have been envisaged. First, we have shown that monolayers of spheres with a superlattice of defects could exhibit a photonic band gap below the light line and have proposed the designs of a L3-like cavity and of a W1-like waveguide. These effects require a refractive index higher than 1.9, which may be obtained with titania spheres, or higher-refractive index materials, e.g. silicon, after a double inversion process. In the case of a complete PBG, as in silicon inverse opals, the whole difficulty lies in the design of defects with suitable modes. This can be addressed by using 2D-3D heterostructures, which provide more tunability on the optical properties of the structure. By optimizing the parameters of the 2D layer, we could design a waveguide in an inverse opal-based heterostructure with a single-mode waveguiding bandwidth of 128 nm centered on 1.55 μm, which is an improvement of better than 70 % compared to previous studies. In a last part, we have put forward the idea that the confinement of light in purely 3D inverse opals could be understood from the study of their 2D cross-sections, which is a clear advantage since such an approach requires much less computational efforts than full 3D calculations. By applying this concept, we have designed a single-mode resonant cavity and different single-mode waveguides, including one with a single-mode waveguiding bandwidth of 110 nm centered on 1.55 μm. Both types of defects may be fabricated by direct laser writing on a single inverse opal, which is a first in the literature. Our approach may also be extended to different directions to make full use of the three-dimensionality of the structure. On the whole, the different designs of cavities and waveguides presented in this chapter allow us to envisage the realization of sophisticated hybrid 2D and 3D opal-based architectures.

The dispersion properties of photonic crystals have concurrently attracted a great deal of attention, owing to the anomalous refraction effects they can yield. In Chapter 3, our objective has been to enhance the control over the propagation of light beams in such structures. Our study has been made on 2D photonic crystals in order to corroborate our conclusions with experiments in a near future. We have started by studying the optical properties of graded photonic crystals, which are known to allow the bending of light on the wavelength scale. Light beams are composed by a set of different wavevectors, which may propagate differently in the structure. We have shown that the extension, shape and curvature of the propagating beam are inherent to the local spatial dispersion of the successive layers and to the strength of the gradient in the structure. Straight iso-frequency curves can yield large

radii of curvature and thus, collimate light beams on large distances, while strong lattice gradients have the tendency to reduce the lateral extension of the beam. The richness of the dispersion properties of photonic crystals actually yields a countless number of possible ways to mold the flow of light. A first step in the integration of graded photonic crystals on all-optical platforms has been made by successfully comparing our modelling with an experiment demonstrating a mirage effect in the microwave range in a metallic structure. In the second part of this chapter, we have studied the coupling of light from integrated waveguides to supercollimating photonic crystals on silicon-on-insulator substrates. We have shown that rib waveguides, which sustain spatially extended and smooth single-modes, are a clear benefit in regard of the mode-profile matching to supercollimated beams. The impedance matching has been improved by truncating the PhC at its boundary. In this way, we have demonstrated transmission efficiencies as high as 96 % and reflections lower than 0.2 % at wavelengths close to 1.55 μm in finite-size supercollimating structure. The calculation has been made in full 3D to take all possible losses into account. The proposed solution combines coupling efficiency, single-mode operation and practicability. It may be applied to extended photonic crystals in general and thus, may open the route toward the development of high-level all-optical integrated technologies.

Metamaterials are another type of nanostructured material, relying on the resonances of their elements to modify the normal propagation of light in space. In Chapter 4, we have been concerned with gaining some theoretical insight onto the optical properties of all-dielectric rod-type structures, which present the interest of being lossless at optical frequencies, by contrast to metallic ones. We have first shown that individual dielectric rods in E-polarization can be assimilated to radiating electric and magnetic dipoles in the long-wavelength limit, by deriving rigorous expressions of their electric and magnetic polarizabilities in terms of their scattering matrix. By using a homogenization model, we have then shown that periodic arrays of such rods imitate a homogeneous medium with dispersive effective permittivity and permeability. We have found in this way that the two lowest photonic band gaps are due to a negative permittivity and that the dispersion curves separating them originate from a negative permeability and thus, exhibit a left-handed behavior. We have shown that these effects hold at optical frequencies and can be obtained by using, for example, silicon rods, suggesting that arrays of dielectric rods can truly manipulate electromagnetic fields like metallic metamaterials without experiencing losses. We have also noted that the spatial dispersion is not a matter of large wavelength-to-period ratio but is inherent to the magnetic dipole activity of the rods. When disorder is introduced, the optical properties of the structure (photonic band gaps and dispersion curves) are expected to be maintained, provided that the density of rods exhibits a low dispersion over the structure. On the microscopic scale, the propagation of light in the magnetic resonance frequency region is ensured by the creation of chains of resonances, which we have assimilated to microscopic necklace states. To our knowledge, this is the first observation of such hybrid modes in 2D, leaving many open questions and motivations for future studies on anomalous transport in disordered media.

In this thesis, we have presented several ways to manipulate electromagnetic fields, using photonic crystals and metamaterials. The great majority of the designs presented here may be fabricated with current techniques and find use in telecommunications, quantum information processing, medical and biological imaging, environmental sensing and solar power, to mention only a few. Yet this is only the tip of the iceberg. A multitude of other optical effects are currently under deep investigation. The different works presented in this thesis show that nanostructured dielectric materials may still be full of surprises.

Bibliography

[1] J. C. Maxwell, *A Treatise on Electricity and Magnetism, 3rd edition*, Dover Publications, 1954.

[2] A. Einstein, Annalen der Physik **322**, 132 (1905).

[3] T. H. Maiman, Nature **187**, 493 (1960).

[4] E. Yablonovitch, Physical Review Letters **58**, 2059 (1987).

[5] S. John, Physical Review Letters **58**, 2486 (1987).

[6] P. Russell, Science **299**, 358 (2003).

[7] M. Lončar, T. Yoshie, A. Scherer, P. Gogna, and Y. M. Qiu, Applied Physics Letters **81**, 2680 (2002).

[8] V. Berger, Physical Review Letters **81**, 4136 (1998).

[9] T. Baba, Nature Physics **2**, 465 (2008).

[10] B. Gralak, S. Enoch, and G. Tayeb, Journal of the Optical Society of America A **17**, 1012 (2000).

[11] L. D. Landau and E. M. Lifshitz, *Vol. 8 Electrodynamics of Continuous Media, 2nd edition*, Pergamon Pr., 1984.

[12] J. B. Pendry, A. J. Holden, D. J. Robbins, and W. J. Stewart, IEEE Transactions on Microwave Theory and Techniques **47**, 2075 (1999).

[13] V. G. Veselago, Soviet Physics Uspekhi-USSR **10**, 509 (1968).

[14] D. R. Smith, W. J. Padilla, D. C. Vier, S. C. Nemat-Nasser, and S. Schultz, Physical Review Letters **84**, 4184 (2000).

[15] J. B. Pendry, Physical Review Letters **85**, 3966 (2000).

[16] Z. Liu, H. Lee, Y. Xiong, C. Sun, and X. Zhang, Science **315**, 1686 (2007).

[17] D. Schurig et al., Science **314**, 977 (2006).

[18] K. Sakoda, *Optical Properties of Photonic Crystals, 2nd edition*, Springer, 2004.

[19] J.-M. Lourtioz et al., *Photonic Crystals: Towards Nanoscale Photonic Devices*, Springer, 2005.

[20] K. Busch et al., Physics Reports **444**, 101 (2007).

[21] P. Viktorovitch et al., Comptes Rendus Physique **8**, 253 (2007).

[22] J. D. Joannopoulos, S. G. Johnson, J. N. Winn, and R. D. Meade, *Photonic Crystals: Molding the Flow of Light, 2nd edition*, Princeton University Press, 2008.

[23] D. R. Smith, J. B. Pendry, and W. C. K. Wiltshire, Science **305**, 788 (2004).

[24] G. V. Eleftheriades and K. G. Balmain, *Negative Refraction Metamaterials: Fundamental Principles and Applications*, Wiley-IEEE Press, 2005.

[25] S. A. Ramakrishna, Reports on Progress in Physics **68**, 449521 (2005).

[26] N. Engheta and R. W. Ziolkowski, *Electromagnetic Metamaterials: Physics and Engineering Explorations*, Wiley-IEEE Press, 2006.

[27] V. M. Shalaev and A. K. Sarychev, *Electrodynamics of Metamaterials*, World Scientific Publishing Company, 2007.

[28] J. V. Sanders, Nature **204**, 1151 (1964).

[29] P. Vukusic and J. R. Sambles, Nature **424**, 852 (2003).

[30] J. P. Vigneron et al., Physical Review E - Part 1 **73**, 041905 (2006).

[31] C. Cohen-Tannoudji, B. Diu, and F. Laloë, *Quantum Mechanics*, Wiley-Interscience, 2006.

[32] J. N. Winn, Y. Fink, S. Fan, and J. D. Joannopoulos, Optics Letters **23**, 1573 (1998).

[33] R. D. Meade, K. D. Brommer, A. M. Rappe, and J. D. Joannopoulos, Applied Physics Letters **61**, 495 (1992).

[34] C. Soukoulis, *Photonic Band Gaps and Localization*, Springer, 1993.

[35] T. F. Krauss, R. M. De La Rue, and S. Brand, Nature **383**, 699 (1996).

[36] D. Labilloy et al., Physical Review Letters **79**, 4147 (1997).

[37] J. E. G. J. Wijnhoven and W. L. Vos, Science **281**, 802 (1998).

[38] A. Blanco et al., Nature **405**, 437 (2000).

[39] Y. A. Vlasov, X. Z. Bo, J. C. Sturm, and D. J. Norris, Nature **414**, 289 (2001).

[40] S. Y. Lin et al., Nature **394**, 251 (1998).

[41] S. Noda, K. Tomoda, N. Yamamoto, and A. Chutinan, Science **289**, 604 (2000).

[42] S. G. Johnson and J. D. Joannopoulos, Applied Physics Letters **77**, 3490 (2000).

[43] O. Toader, M. Berciu, and S. John, Physical Review Letters **90**, 233901 (2003).

[44] H. T. Miyazaki, H. Miyazaki, K. Ohtaka, and T. Sato, Journal of Applied Physics **87**, 7152 (2000).

[45] M. Campbell, D. N. Sharp, M. T. Harrison, R. G. Denning, and A. J. Turberfield, Nature **404**, 53 (2000).

[46] H. B. Sun, S. Matsuo, and H. Misawa, Applied Physics Letters **74**, 786 (1999).

[47] J. D. Joannopoulos, P. R. Villeneuve, and S. H. Fan, Nature **386**, 143 (1997).

[48] N. W. Ashcroft and N. D. Mermin, *Solid State Physics*, Brooks Cole, 1976.

[49] E. M. Purcell, Physical Review **69**, 681 (1946).

[50] N. Gisin, G. Ribordy, W. Tittel, and H. Zbinden, Reviews of Modern Physics **74**, 145 (2002).

[51] C. J. M. Smith et al., Applied Physics Letters **78**, 1487 (2001).

[52] G. Lecamp et al., Applied Physics Letters **90**, 091120 (2007).

[53] P. Velha et al., Optics Express **15**, 16090 (2007).

[54] M. Notomi, E. Kuramochi, and H. Taniyama, Optics Express **16**, 11095 (2008).

[55] Y. Akahane, T. Asano, B. S. Song, and S. Noda, Nature **425**, 944 (2003).

[56] B. S. Song, S. Noda, T. Asano, and Y. Akahane, Nature Materials **4**, 207 (2005).

[57] T. Yoshie et al., Nature **432**, 200 (2004).

[58] D. Englund et al., Physical Review Letters **95**, 013904 (2005).

[59] O. Painter et al., Science **284**, 1819 (1999).

[60] C. Monat et al., Electronic Letters **37**, 764 (2001).

[61] H. G. Park et al., Science **305**, 1444 (2004).

[62] S. Y. Lin, E. Chow, V. Hietala, P. R. Villeneuve, and J. D. Joannopoulos, Science **282**, 274 (1998).

[63] A. Talneau, P. Lalanne, M. Agio, and C. M. Soukoulis, Optics Letters **27**, 1522 (2002).

[64] S. J. McNab, N. Moll, and Y. A. Vlasov, Optics Express **11**, 2927 (2003).

[65] E. Chow et al., Nature **407**, 983 (2000).

[66] M. H. Qi et al., Nature **429**, 538 (2004).

[67] S. Ogawa, K. Ishizaki, T. Furukawa, and S. Noda, Electronic Letters **44**, 377 (2008).

[68] M. Imada, L. H. Lee, M. Okano, S. Kawashima, and S. Noda, Applied Physics Letters **88**, 171107 (2006).

[69] M. Deubel, M. Wegener, S. Linden, G. von Freymann G, and S. John, Optics Letters **31**, 805 (2006).

[70] R. J. Liu, Z. Y. Li, Z. F. Feng, B. Y. Cheng, and D. Z. Zhang, Journal of Applied Physics **103**, 094514 (2008).

[71] P. V. Braun, S. A. Rinne, and F. García-Santamaría, Advanced Materials **18**, 2665 (2006).

[72] J. P. Dowling and C. M. Bowden, Journal of Modern Optics **41**, 345 (1994).

[73] H. Kosaka et al., Applied Physics Letters **74**, 1212 (1999).

[74] J. Witzens, M. Lončar, and A. Scherer, IEEE Journal of Selected Topics in Quantum Electronics **8**, 1246 (2002).

[75] D. N. Chigrin, S. Enoch, C. M. Sotomayor-Torres, and G. Tayeb, Optics Express **11**, 1203 (2003).

[76] P. T. Rakich et al., Nature Materials **5**, 93 (2006).

[77] X. F. Yu and S. H. Fan, Applied Physics Letters **83**, 3251 (2003).

[78] S. Y. Kim, G. P. Nordin, J. B. Cai, and J. H. Jiang, Optics Letters **28**, 2384 (2003).

[79] D. W. Prather et al., Journal of Physics D: Applied Physics **40**, 2635 (2007).

[80] H. Kosaka et al., Physical Review B **58**, 10096 (1998).

[81] S. Enoch, G. Tayeb, and D. Maystre, Optics Communications **161**, 171 (1999).

[82] D. Felbacq, B. Guizal, and F. Zolla, Journal of Optics A: Pure and Applied Optics **2**, L30 (2000).

[83] A. I. Căbuz, E. Centeno, and D. Cassagne, Applied Physics Letters **84**, 2031 (2004).

[84] T. Ochiai and J. Sanchez-Dehesa, Physical Review B **64**, 245113 (2001).

[85] L. J. Wu, M. Mazilu, and T. F. Krauss, Journal of Lightwave Technology **21**, 561 (2003).

[86] M. Notomi, Physical Review B **62**, 10696 (2000).

[87] C. Luo, S. G. Johnson, J. D. Joannopoulos, and J. B. Pendry, Physical Review B **65**, 201104 (2002).

[88] E. Cubukcu, K. Aydin, E. Özbay, S. Foteinopoulou, and C. M. Soukoulis, Nature **423**, 604 (2003).

[89] P. V. Parimi, W. T. T. Lu, P. Vodo, and S. Sridhar, Nature **426**, 404 (2003).

[90] C. Y. Luo, S. G. Johnson, J. D. Joannopoulos, and J. B. Pendry, Physical Review B **68**, 045115 (2003).

[91] W. Kock, Proceedings of the IRE **34**, 828 (1946).

[92] J. B. Pendry, A. J. Holden, W. J. Stewart, and I. Youngs, Physical Review Letters **76**, 4773 (1996).

[93] R. A. Shelby, D. R. Smith, and S. Schultz, Science **292**, 77 (2001).

[94] J. B. Pendry, D. Schurig, and D. R. Smith, Science **312**, 1780 (2006).

[95] J. Zhou et al., Physical Review Letters **95**, 223902 (2005).

[96] V. M. Shalaev, Nature Photonics **1**, 41 (2007).

[97] C. M. Soukoulis, S. Linden, and M. Wegener, Science **315**, 47 (2007).

[98] J. Yao et al., Science **321**, 930 (2008).

[99] J. Valentine et al., Nature **455**, 376 (2008).

[100] H. van de Hulst, *Light Scattering By Small Particles*, Dover Publications, 1981.

[101] S. O'Brien and J. B. Pendry, Journal of Physics: Condensed Matter **14**, 4035 (2002).

[102] D. Felbacq and G. Bouchitté, Physical Review Letters **94**, 183902 (2005).

[103] L. Jylhä, I. Kolmakov, S. Maslovski, and S. Tretyakov, Journal of Applied Physics **99**, 043102 (2006).

[104] L. Peng et al., Physical Review Letters **98**, 157403 (2007).

[105] J. A. Schuller, R. Zia, T. Taubner, and M. L. Brongersma, Physical Review Letters **99**, 107401 (2007).

[106] K. M. Ho, C. T. Chan, and C. M. Soukoulis, Physical Review Letters **65**, 3152 (1990).

[107] S. G. Johnson and J. D. Joannopoulos, Optics Express **8**, 173 (2001).

[108] MIT photonic bands, `http://ab-initio.mit.edu/mpb/`.

[109] K. S. Yee, IEEE Transactions on Antennas and Propagation **14**, 302 (1966).

[110] A. Taflove and S. C. Hagness, *Computational Electrodynamics: the finite-difference time-domain method, 2nd edition*, Artech House, 2000.

[111] V. A. Mandelshtam and H. S. Taylor, Journal of Chemical Physics **107**, 6756 (1997).

[112] MIT electromagnetic equation propagation, `http://ab-initio.mit.edu/meep/`.

[113] J. P. Berenger, Journal of Computational Physics **114**, 185 (1994).

[114] J. Jin, *The Finite Element Method in Electromagnetics, 2nd edition*, John Wiley & Sons, 2002.

[115] COMSOL multiphysics, `http://www.comsol.com/`.

[116] J. D. Jackson, *Classical Electrodynamics, 3rd edition*, Wiley, 1999.

[117] D. Felbacq, G. Tayeb, and D. Maystre, Journal of the Optical Society of America A **11**, 2526 (1994).

[118] Y. L. Xu, Applied Optics **34**, 4573 (1995).

[119] M. Abramowitz and I. A. Stegun, *Handbook of Mathematical Functions: with Formulas, Graphs, and Mathematical Tables*, Dover Publications, 1965.

[120] G. Tayeb and D. Maystre, Journal of the Optical Society of America A **14**, 3323 (1997).

[121] E. Centeno and D. Felbacq, Journal of the Optical Society of America A **17**, 320 (2000).

[122] The PHAT project, `http://www.tyndall.ie/phat/`.

[123] C. López, Advanced Materials **15**, 1679 (2003).

[124] C. López, Journal of Optics A: Pure and Applied Optics **8**, R1 (2006).

[125] S. C. Mau and D. A. Huse, Physical Review E **59**, 4396 (1999).

[126] P. Jiang, J. F. Bertone, K. S. Hwang, and V. L. Colvin, Chemistry of Materials **11**, 2132 (1999).

[127] A. Amann, W. Khunsin, G. Kocher, C. M. Sotomayor Torres, and E. P. O'Reilly, Proceedings of SPIE **6603**, 660321 (2007).

[128] P. Jiang and M. J. McFarland, Journal of the American Chemical Society **126**, 13778 (2004).

[129] C. Kittel, *Introduction to Solid State Physics, 8th edition*, Wiley, 2004.

[130] H. S. Sözüer, J. W. Haus, and R. Inguva, Physical Review B **45**, 13962 (1992).

[131] H. Míguez et al., Advanced Materials **13**, 1634 (2001).

[132] S. John and K. Busch, Journal of Lightwave Technology **17**, 1931 (1999).

[133] A. Chutinan and S. John, Physical Review E **71**, 026605 (2005).

[134] Z. Y. Li and Z. Q. Zhang, Physical Review B **62**, 1516 (2000).

[135] J. H. Ye et al., Langmuir **22**, 7378 (2006).

[136] R. Iliew, C. Etrich, and F. Lederer, Optics Express **13**, 7076 (2005).

[137] K. Ren, Z. Y. L. X. B. Ren, S. Feng, B. Y. Cheng, and D. Z. Zhang, Physical Review B **75**, 115108 (2007).

[138] Q. F. Yan, L. K. Wang, and X. F. Zhao, Advanced Functional Materials **17**, 3695 (2007).

[139] F. Jonsson et al., Microelectronic Engineering **78-79**, 429 (2005).

[140] G. Kocher et al., 2D photonic defect layers in 3D inverted opals on Si platforms, in *Proc. International Conference on Transparent Optical Networks*, volume 2, pages 68–72, 2006.

[141] W. J. Cai and R. Piestun, Applied Physics Letters **88**, 111112 (2006).

[142] S. A. Rinne, F. García-Santamaría, and P. V. Braun, Nature Photonics **2**, 52 (2008).

[143] V. Lousse and S. Fan, Optics Express **14**, 866 (2006).

[144] D. L. C. Chan, E. Lidorikis, and J. D. Joannopoulos, Physical Review E - Part 2 **71**, 056602 (2005).

[145] S. Yano et al., Physical Review B **66**, 075119 (2002).

[146] X. C. Jiang, T. Herricks, and Y. N. Xia, Advanced Materials **15**, 1205 (2003).

[147] N. Tétreault et al., Advanced Materials **18**, 457 (2006).

[148] M. Qiu, Physical Review B **66**, 033103 (2002).

[149] D. Cassagne, C. Jouanin, and D. Bertho, Physical Review B **53**, 7134 (1996).

[150] S. G. Johnson, P. R. Villeneuve, S. H. Fan, and J. D. Joannopoulos, Physical Review B **62**, 8212 (2000).

[151] N. Ganesh et al., Nature Nanotechnology **2**, 515 (2007).

[152] R. L. Espinola, R. U. Ahmad, F. Pizzuto, M. J. Steel, and R. M. Osgood, Optics Express **8**, 517 (2001).

[153] A. Chutinan, S. John, and O. Toader, Physical Review Letters **90**, 123901 (2003).

[154] A. Chutinan and S. John, Physical Review B **72**, 161316 (2005).

[155] A. Chutinan and S. John, Photonics and Nanostructures Fundamentals and Applications **2**, 41 (2004).

[156] M. L. Povinelli, S. G. Johnson, S. Fan, and J. D. Joannopoulos, Physical Review B **64**, 075313 (2001).

[157] R. P. Feynman, R. B. Leighton, and M. Sands, *The Feynman lectures on Physics. Mainly mechanics, radiation and heat*, chapter 26, Addison-Wesley, Reading, MA, 1963.

[158] E. Centeno and D. Cassagne, Optics Letters **30**, 2278 (2005).

[159] E. Centeno, D. Cassagne, and J. P. Albert, Physical Review B **73**, 235119 (2006).

[160] H. Kurt and D. S. Citrin, Optics Express **15**, 1240 (2007).

[161] P. Pottier, M. Gnan, and R. M. De La Rue, Optics Express **15**, 6569 (2007).

[162] T. Baba, D. Mori, K. Inoshita, and Y. Kuroki, IEEE Journal of Selected Topics in Quantum Electronics **10**, 484 (2004).

[163] E. Akmansoy, E. Centeno, K. Vynck, D. Cassagne, and J.-M. Lourtioz, Applied Physics Letters **92**, 133501 (2008).

[164] U. Leonhardt and T. G. Philbin, Transformation optics and the geometry of light, arXiv:0805.4778v2.

[165] S. G. Johnson et al., Physical Review E **66**, 066608 (2002).

[166] V. Zabelin et al., Optics Letters **32**, 530 (2007).

[167] B. Lombardet, L. A. Dunbar, R. Ferrini, and R. Houdré, Journal of the Optical Society of America B **22**, 1179 (2005).

[168] E. Cassan, D. Bernier, G. Maire, D. Marris-Morini, and L. Vivien, Journal of the Optical Society of America B **24**, 1211 (2007).

[169] J. Witzens and A. Scherer, Journal of the Optical Society of America A **20**, 935 (2003).

[170] D. W. Prather et al., Optics Letters **29**, 50 (2004).

[171] B. Miao, C. Chen, S. Shi, and D. W. Prather, IEEE Photonics Technology Letters **17**, 61 (2005).

[172] M. Augustin et al., Applied Physics B: Lasers and Optics **81**, 313 (2005).

[173] T. Baba and D. Ohsaki, Japanese Journal of Applied Physics **40**, 59205924 (2001).

[174] J. Witzens, M. Hochberg, T. Baehr-Jones, and A. Scherer, Physical Review E **69**, 046609 (2004).

[175] B. Momeni and A. Adibi, Applied Physics Letters **87**, 171104 (2005).

[176] P. Lalanne and A. Talneau, Optics Express **10**, 354 (2002).

[177] S. Lardenois et al., Optics Letters **28**, 1150 (2003).

[178] Y. A. Vlasov and S. J. McNab, Optics Letters **31**, 50 (2006).

[179] R. A. Soref, J. Schmidtchen, and K. Petermann, IEEE Journal of Quantum Electronics **27**, 1971 (1991).

[180] P. Yeh, *Optical waves in layered media, 2nd ed.*, John Wiley & Sons, 2005.

[181] Z. Lu and D. W. Prather, Optics Express **15**, 8340 (2007).

[182] W. Śmigaj and B. Gralak, Physical Review B **77**, 235445 (2008).

[183] B. Momeni, A. A. Eftekhar, and A. Adibi, Optics Letters **32**, 778 (2007).

[184] K. C. Huang, M. L. Povinelli, and J. D. Joannopoulos, Applied Physics Letters **85**, 543 (2004).

[185] V. Yannopapas and A. Moroz, Journal of Physics: Condensed Matter **17**, 3717 (2005).

[186] M. S. Wheeler, J. S. Aitchison, and M. Mojahedi, Physical Review B **72**, 193103 (2005).

[187] A. Ahmadi and H. Mosallaei, Physical Review B **77**, 045104 (2008).

[188] C. M. Soukoulis, T. Koschny, J. F. Zhou, M. Kafesaki, and E. N. Economou, Physica Status Solidi B - Basic Solid State Physics **244**, 1181 (2007).

[189] D. Kajfez and P. Guillon, *Dielectric Resonators*, Artech House, 1986.

[190] W. Cai, U. K. Chettiar, A. V. Kildishev, and V. M. Shalaev, Optics Express **16**, 5444 (2008).

[191] D. P. Gaillot, C. Croenne, and D. Lippens, Optics Express **16**, 3986 (2008).

[192] R. C. McPhedran, C. G. Poulton, N. A. Nicorovici, and A. B. Movchan, Proceedings of the Royal Society of London Series A: Mathematical Physical and Engineering Sciences **452**, 2231 (1996).

[193] M. G. Silveirinha, Physical Review E **73**, 046612 (2006).

[194] G. B. Arfken and H. J. Weber, *Mathematical Methods for Physicists, 5th edition*, Academic Press, 2000.

[195] W. J. Padilla, D. N. Basov, and D. R. Smith, Materials Today **9**, 28 (2006).

[196] A. Sihvola, Metamaterials **1**, 2 (2007).

[197] C. M. Soukoulis, J. Zhou, T. Koschny, M. Kafesaki, and E. N. Economou, Journal of Physics: Condensed Matter **20**, 304217 (2008).

[198] E. Lidorikis, M. M. Sigalas, E. N. Economou, and C. M. Soukoulis, Physical Review Letters **81**, 1405 (1998).

[199] A. Moroz and A. Tip, Journal of Physics: Condensed Matter **11**, 2503 (1999).

[200] Y. N. Barabanenkov and M. Y. Barabanenkov, Journal of the Optical Society of America A **23**, 581 (2006).

[201] C. Rockstuhl, U. Peschel, and F. Lederer, Optics Letters **31**, 1741 (2006).

[202] D. R. Smith, D. C. Vier, T. Koschny, and C. M. Soukoulis, Physical Review E - Part 2 **71**, 036617 (2005).

[203] D. R. Smith and J. B. Pendry, Journal of the Optical Society of America B **23**, 391 (2006).

[204] A. Sihvola, *Electromagnetic Mixing Formulae and Applications*, INSPEC, Inc., 2000.

[205] P. A. Belov and C. R. Simovski, Physical Review E - Part 2 **72**, 026615 (2005).

[206] C. R. Simovski and S. A. Tretyakov, Physical Review B **75**, 195111 (2007).

[207] R. E. Collin, *Field Theory of Guided Waves, 2nd edition*, Wiley-IEEE Press, 1990.

[208] C. R. Simovski and S. L. He, Physics Letters A **311**, 254 (2003).

[209] P. A. Belov et al., Physical Review B **67**, 113103 (2003).

[210] A. I. Căbuz, D. Felbacq, and D. Cassagne, Physical Review Letters **98**, 037403 (2007).

[211] A. I. Căbuz, D. Felbacq, and D. Cassagne, Physical Review A **77**, 013807 (2008).

[212] Y. Xu, H. B. Sun, J. Y. Ye, S. Matsuo, and H. Misawa, Journal of the Optical Society of America B **18**, 1084 (2001).

[213] M. Tokushima, H. Yamada, and Y. Arakawa, Applied Physics Letters **84**, 4298 (2004).

[214] K. Aydin, K. Guven, N. Katsarakis, C. M. Soukoulis, and E. Özbay, Optics Express **12**, 5896 (2004).

[215] A. A. Zharov, I. V. Shadrivov, and Y. S. Kivshar, Journal of Applied Physics **97**, 113906 (2005).

[216] P. Sheng, *Introduction to Wave Scattering, Localization And Mesoscopic Phenomena, 2nd edition*, 2006.

[217] M. M. Sigalas, C. M. Soukoulis, C. T. Chan, and D. Turner, Physical Review B **53**, 8340 (1996).

[218] A. A. Asatryan et al., Physical Review E - Part B **62**, 5711 (2000).

[219] D. Felbacq and G. Bouchitté, New Journal of Physics **7**, 159 (2005).

[220] H. Miyazaki, M. Hase, H. T. Miyazaki, Y. Kurokawa, and N. Shinya, Physical Review B **67**, 235109 (2003).

[221] G. Guida, Optics Communications **156**, 294 (1998).

[222] Z. F. Feng et al., Physical Review Letters **94**, 247402 (2005).

[223] E. D. Gennaro et al., Physical Review B **77**, 193104 (2008).

[224] J. B. Pendry, Journal of Physics C: Solid State Physics **20**, 733 (1987).

[225] J. Bertolotti, S. Gottardo, D. S. Wiersma, M. Ghulinyan, and L. Pavesi, Physical Review Letters **94**, 113903 (2005).

[226] D. S. Wiersma, Nature Physics **4**, 359 (2008).

[227] S. Mujumdar, M. Ricci, R. Torre, and D. S. Wiersma, Physical Review Letters **93**, 053903 (2004).

[228] C. Vanneste, P. Sebbah, and H. Cao, Physical Review Letters **98**, 143902 (2007).

[229] S. Gottardo et al., Nature Photonics **2**, 429 (2008).